

การศึกษาต่อคาร์บอนนาโนผนังเดี่ยวเชื่อมด้วยไฮ-กระสุน โดยฟังก์ชันนอล

ความหนาแน่น



วิทยานิพนธ์นี้เป็นส่วนหนึ่งของการศึกษาตามหลักสูตรปริญญาวิทยาศาสตรดุษฎีบัณฑิต

สาขาวิชาฟิสิกส์

มหาวิทยาลัยเทคโนโลยีสุรนารี

ปีการศึกษา 2559

**DENSITY-FUNCTIONAL STUDY OF HYDRAZINE
DOPED SINGLE-WALLED CARBON NANOTUBES**

Wutthisak Prachamon



A Thesis Submitted in Partial Fulfillment of the Requirements for the

Degree of Doctor of Philosophy in Physics

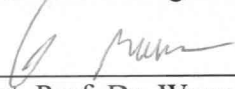
Suranaree University of Technology

Academic Year 2016

**DENSITY-FUNCTIONAL STUDY OF HYDRAZINE DOPED
SINGLE-WALLED CARBON NANOTUBES**

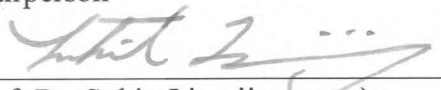
Suranaree University of Technology has approved this thesis submitted in partial fulfillment of the requirements for the Degree of Doctor of Philosophy.

Thesis Examining Committee



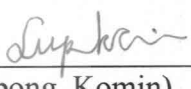
(Asst. Prof. Dr. Worawat Meevasana)

Chairperson



(Prof. Dr. Sukit Limpijumnong)

Member (Thesis Advisor)



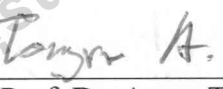
(Dr. Sittipong Komin)

Member



(Asst. Prof. Dr. Michael F. Smith)

Member



(Assoc. Prof. Dr. Anan Tongraar)

Member



(Prof. Dr. Santi Maensiri)

Acting Vice Rector for Academic Affairs
and Internationalisation



(Prof. Dr. Santi Maensiri)

Dean of Institute of Science

วุฒิสกดิ์ ประชามอญ : การศึกษาต่อคาร์บอนนาโนทิวส์เดี่ยวเชื่อมด้วยไฮ-ดระซีน โดย ฟังก์ชันนอลความหนาแน่น (DENSITY-FUNCTIONAL STUDY OF HYDRAZINE DOPED SINGLE-WALLED CARBON NANOTUBES) อาจารย์ที่ปรึกษา : ศาสตราจารย์ ดร.ชูกิจ ลิมปิจำนงค์, 94 หน้า.

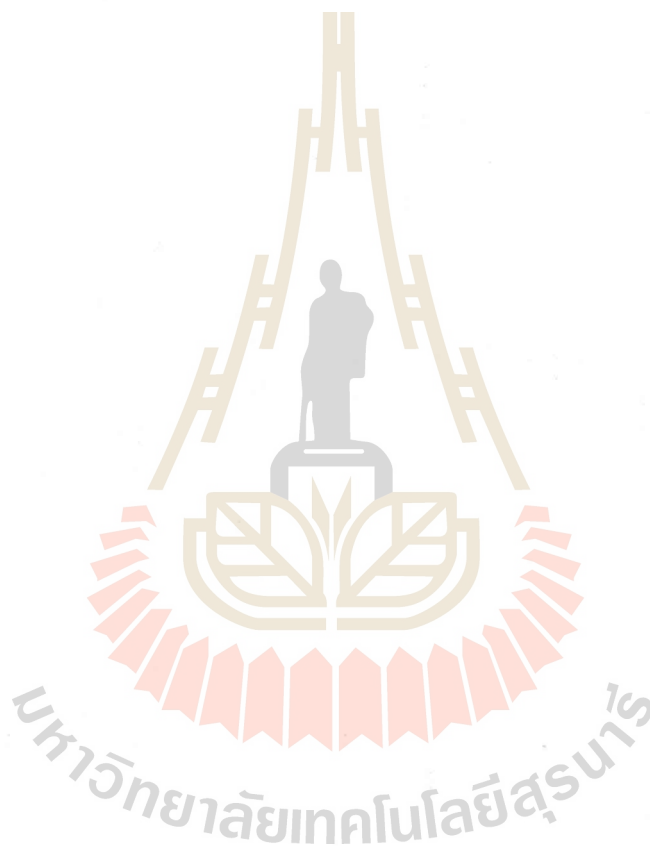
วิทยานิพนธ์นี้ ได้รายงานการศึกษาเชิงทฤษฎีของต่อคาร์บอนนาโนทิวส์เดี่ยวเชื่อมด้วยไฮ-ดระซีน โดยใช้การคำนวณแบบเฟสฟังก์ชันฟิลบนพื้นฐานของ ทฤษฎีฟังก์ชันนอลความหนาแน่น ฟังก์ชันนอลความหนาแน่นได้เพิ่มความถูกต้องด้วยอันตรกิริยาแบบแวนเดอร์วาลส์ เพื่อใช้หาค่าเหมาะที่สุดของการซ้กันแบบมีขอบเขตของโครงข่ายพันธะไฮโดรเจน ผลลัพธ์จากการคำนวณแถบพลังงาน แถบพลังงานจากการเชื่อมแบ่งออกเป็นสามกลุ่ม กลุ่มแรก สถานะเชื่อมต่ำกว่าค่าสูงสุดแถบวาเลนซ์ (ISBMVS) กลุ่มที่สอง สถานะเชื่อมปกติ (ต่ำกว่า) ค่าสูงสุดแถบวาเลนซ์ (ISCMVS) กลุ่มที่สาม สถานะผู้ให้ในแถบพลังงาน (DS)

การลดลงเชิงตำแหน่งของความหนาแน่นอิเล็กตรอน (RDG) และการวิเคราะห์ประจุแบบ Bader ถูกนำมาใช้แสดงให้เห็นว่า โมเลกุลไฮ-ดระซีนที่เป็นเงื่อนไขของการเกิดสถานะผู้ให้ในแถบพลังงานประกอบด้วย โครงข่ายพันธะไฮโดรเจน และการจัดเรียงตัวอย่างมีรูปแบบ การจัดเรียงตัวของไฮ-ดระซีนโมเลกุลนี้ H อะตอมของทั้งสองด้านต้องชี้ไปยัง N อะตอมของโมเลกุลอื่น เงื่อนไขของการส่งผ่านของอิเล็กตรอน พิจารณาจาก PDOS ของแต่ละโมเลกุล

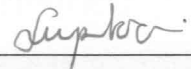
วิธี GIPAW ถูกใช้ในการศึกษานิวเคลียร์แมกเนติกเรโซแนนซ์ (NMR) ค่า ^{13}C เคมีคัลซิฟท์ (δ) ถูกนำมาใช้ตรวจสอบอันตรกิริยาระหว่างโมเลกุลกับต่อคาร์บอนนาโนทิวส์เดี่ยว การส่งผ่านของอิเล็กตรอน ขึ้นกับรูปแบบของอันตรกิริยาแบบไม่ใช่โควาเลนต์ของต่อคาร์บอนนาโนทิวส์เดี่ยวกับไฮ-ดระซีนโมเลกุล ในกรณีที่เกิดสถานะผู้ให้ในแถบพลังงาน ค่า ^{13}C NMR δ เลื่อนไปทางความถี่ต่ำลง (4 ppm) เมื่อเทียบกับต่อคาร์บอนนาโนทิวส์เดี่ยวบริสุทธิ์ สำหรับกรณีอันตรกิริยาแบบแวนเดอร์วาลส์ ค่า ^{13}C NMR δ จะมีการเลื่อนไปทางความถี่สูงขึ้นเมื่อเทียบกับต่อคาร์บอนนาโนทิวส์เดี่ยวบริสุทธิ์ ในกรณีที่เกิดสถานะผู้ให้ในแถบพลังงาน ค่า ^1H NMR δ ใช้บอกถึงการจัดเรียงตัวของไฮ-ดระซีนโมเลกุล และค่า ^1H NMR δ เลื่อนไปทางความถี่สูงขึ้นมากที่สุด (10 ppm เทียบกับ TMS)

แถบการดูดกลืนแสง ศึกษาด้วย TDDFT สถานะผู้ให้ในแถบพลังงานที่เกิดจากการดูดซับทางกายภาพของต่อคาร์บอนนาโนทิวส์เดี่ยวเชื่อมด้วยไฮ-ดระซีนเป็นสาเหตุที่ทำให้เกิดแยกออกของแถบพลังงานที่เท่ากัน จากการแยกออกของแถบพลังงานทำให้เกิดการเปลี่ยน optical transition ของ

E_{11} จาก dark excitons ไปเป็น bright excitons จากการ transition ของ HOMO-0(+) \rightarrow LUMO+3(+) และ HOMO-0(-) \rightarrow LUMO+3(-).



สาขาวิชาฟิสิกส์
ปีการศึกษา 2559

ลายมือชื่อนักศึกษา 
ลายมือชื่ออาจารย์ที่ปรึกษา 
ลายมือชื่ออาจารย์ที่ปรึกษาร่วม 

WUTTHISAK PRACHAMON : DENSITY-FUNCTIONAL STUDY OF
HYDRAZINE DOPED SINGLE-WALLED CARBON NANOTUBES.

THESIS ADVISOR : PROF. SUKIT LIMPIJUMNONG, Ph.D. 94 PP.

DFT/CARBON NANOTUBES/TDDFT

In this thesis, reported the theoretical study of hydrazine doped single-walled carbon nanotube (SWCNT), the calculation was carried out by using first-principle calculation based on the density functional theory (DFT) corrected by the van der Waals (vdW) interaction. The DFT was used to carry out the periodic boundary condition (PBC) geometry optimization which hydrazine formed the hydrogen bond network (HBN). The electronic band structures are classified according to three group, first, the impurity state below the maximum valence state (ISBMVS), second, the impurity state close to the maximum valence state (ISCMVS) and, third, the DS.

The reduced density gradient (RDG) approach and the Bader charge analysis were used to reveal the hydrazine molecule which cause DS to occur. We found that the case of DS occurrence, it depends on both HBN and configuration of a hydrazine molecule; the molecule a H atom of both side of itself point to a N atom of another molecule (a N atom of itself could pointed by a H atom of another molecule). The condition for electron charge transfer was considered based on projected density of state (PDOS) of each molecule.

The nuclear magnetic resonance (NMR) chemical shifts (δ) for noncovalent interaction of hydrazine doped SWCNT was studied computationally using gauge-including projector-augmented plane-wave (GIPAW) DFT. The ^{13}C NMR δ for the

case of DS occurrence was described. To confirm the configuration which obtained DS we found ^{13}C NMR δ shifts to a lower frequency (4 ppm) for N-H $\cdots\pi$ interaction when compare to pristine SWCNT, and shifts to a higher frequency for the case of vdW interaction. The local structure signature of ^1H NMR δ of a hydrazine molecule which cause DS to occur was used to identify electronic band structure. For ^1H NMR δ of hydrazine molecules, when HBN occurrence the ^1H NMR δ shifts to a higher frequency when compare to isolated hydrazine (Gauche), and more shifts to a higher frequency (10 ppm compare to TMS) for the molecule that satisfied the condition DS to occur.

The absorption spectra will be calculated by using time-dependent density functional theory (TDDFT). The DS in physisorption of hydrazine doped SWCNT is a cause for change the optical transition of E_{11} and photon absorption energy. When hydrazine caused the degenerate band of SWCNTs to split into nondegenerate bands ((-),(+)), the optical transitions also changed. In the case of DS occurrence the dark excitons changed to bright excitons are the optical transitions from HOMO-0(+) \rightarrow LUMO+3(+) and HOMO-0(-) \rightarrow LUMO+3(-).

School of Physics

Academic Year 2016

Student's Signature Wutthisak Prachanon

Advisor's Signature [Signature]

Co-advisor's Signature [Signature]

ACKNOWLEDGEMENTS

I would like to express my gratitude to the following people for their assistance and support which have enabled me to complete my thesis.

My thesis advisor Prof. Dr. Sukit Limpijumnong and thesis co-advisor Dr. Sittipong Komin.

I would like to thank Asst. Prof. Dr. Worawat Meevasana, Asst. Prof. Dr. Michael F. Smith and Assoc. Prof. Dr. Anan Tongraar for sitting at the thesis committee

I would like to thank the School of Physics Institute of Science Suranaree University of Technology, and the members of the condensed matter theory SUT group.

I would like to thank Ubon Ratchathani University, Department of Physics Ubon Ratchathani University and Dr. Chittakorn Polyon head of department, and Mr. Phongnared Boontueng member of Laboratory of Computational Spectroscopy and Material Modelling Department of Physics Ubon Ratchathani University.

Wutthisak Prachamon

CONTENTS

	Page
ABSTRACT IN THAI.....	I
ABSTRACT IN ENGLISH.....	III
ACKNOWLEDGEMENTS.....	V
CONTENTS.....	VI
LIST OF TABLES.....	IX
LIST OF FIGURES.....	XIII
LIST OF ABBREVIATIONS.....	XVIII
CHAPTER	
I INTRODUCTION.....	1
1.1 Introduction.....	1
1.2 Research objectives.....	4
1.3 Scope and limitations.....	4
II COMPUTATIONAL METHODS.....	6
2.1 Research Methods.....	6
2.2 Density functional theory.....	7
2.2.1 The Hohenberg and Kohn theorem.....	8
2.2.2 Kohn and Sham equation.....	8
2.2.3 The local density approximation (LDA).....	9
2.2.4 The generalized gradient approximation (GGA).....	9

CONTENTS (Continued)

	Page
2.2.5 Van der Waals (vdW) interaction.....	10
2.2.6 Gauge including projector augmented wave method.....	10
2.2.7 Time dependent density functional perturbation theory.....	13
III LITERATURE REVIEWS.....	17
3.1 Single-walled carbon nanotubes (SWCNTs).....	17
3.2 Hydrazine.....	18
3.3 Hydrazine doped SWCNTs.....	19
IV RESULTS.....	21
4.1 Configurations.....	21
4.1.1 Configurations and electronic band structures.....	21
4.1.2 Electron charge transfer.....	28
4.1.3 Configuration and Interaction Energy.....	33
4.2 NMR chemical shifts (δ).....	36
4.2.1 ^{13}C NMR chemical shifts (δ).....	36
4.2.2 ^1H NMR chemical shifts (δ).....	38
4.3 Ultraviolet-visibility (UV-Vis) spectroscopic.....	42
4.3.1 Photon absorption energy of IS and DS.....	43
4.3.2 Optical transition of IS and DS.....	44
4.3.3 Native defect in SWCNTs.....	59
4.3.4 Electronic structures of native defect in SWCNTs.....	61

CONTENTS (Continued)

	Page
4.3.5 Optical transitions of native defect in SWCNTs.....	65
4.3.6 Photon absorption spectra of native defect in SWCNTs.....	73
V CONCLUSIONS.....	78
5.1 Configurations.....	78
5.2 NMR chemical shifts (δ).....	79
5.3 Ultraviolet-visibility (UV-Vis) spectroscopic.....	79
REFERENCES	81
CURRICULUM VITAE.....	94

LIST OF TABLES

Table		Page
4.1	Calculated electronic band structure state (EBSS) and band gap, of pristine SWCNT and hydrazine doped SWCNTs. Abbreviations: VBM = valence band maximum, CBM = conduction band minimum, DS = donor state	29
4.2	Calculated binding energy and interaction energy in eV for intermolecular interaction of hydrazine doped SWCNTs	35
4.3	Calculated Bader charge analysis of hydrazine and SWCNT in e ⁻¹ unit.....	36
4.4	Calculated the σ (ppm) of C atoms that are closest to the H atom of the N-H... π interaction of each interaction	38
4.5	<i>E₁₁</i> Photon absorption energy (PAE) in eV of pristine and doped SWCNTs. Abbreviations: P = pristine, SW = Stone-Wales, DV = diatom vacancies, SV = single vacancy, IS = impurity state, DS = donor state, ISBMVS = impurity state below the maximum valence state, ISCMVS = impurity state close to the maximum valence state, Shift = (PAE-doped) - (PAE-pristine)	55

LIST OF TABLES (Continued)

Table		Page
4.6	<p>E_{22} Photon absorption energy (PAE) in eV of pristine and doped SWCNTs. Abbreviations: P = pristine, SW = Stone-Wales, DV = diatom vacancies, SV = single vacancy, IS = impurity state, DS = donor state, ISBMVS = impurity state below the maximum valence state, ISCMVS = impurity state close to the maximum valence state, Shift = (PAE-doped) - (PAE-pristine)</p>	56
4.7	<p>Electric dipole allowed (di-al) and forbidden (di-fo) optical transitions of pristine and doped (8,0) SWCNTs. Abbreviations: P = pristine, DS = donor state, ISBMVS = impurity state below the maximum valence state, ISCMVS = impurity state close to the maximum valence state</p>	57
4.8	<p>Calculated Eigen energies in eV at the Γ-point of the pristine (8,0) SWCNT and doped (8,0) SWCNTs, model, P-hyd-1, P-hyd-2 and P-hyd-3. To aid identification of the energy levels, the labels are shown. The Fermi energy (E_f) of each system is also shown. Label abbreviations: L = lowest unoccupied molecular orbital, H = highest occupied molecular orbital</p>	58

LIST OF TABLES (Continued)

Table		Page
4.9	<p>Calculated Eigen energies in eV at the Γ-point of the pristine (8,0) SWCNT and defected (8,0) SWCNTs, namely, single vacancy (SV), diatom vacancy (DV), and Stone-Wales (SW). To aid identification of the energy levels, the labels are shown in column 2 and 6 for pristine SWCNT and defected SWCNTs, respectively. The Fermi energy (E_f) of each system is also shown. Label abbreviations: L = lowest unoccupied molecular orbital, H = highest occupied molecular orbital, vi = virtual state, oc = occupied state</p>	72
4.10	<p>Calculated formation energies and band gaps of the pristine (8,0) SWCNT and defected (8,0) SWCNTs, namely, single vacancy (SV), diatom vacancy (DV), and Stone-Wales (SW). The band gaps are calculated from the lowest unoccupied state minus the highest occupied state in Table 4.9</p>	74
4.11	<p>Electric dipole allowed (di-al) and forbidden (di-fo) optical transitions of pristine and defected (8,0) SWCNTs. Abbreviations: P = pristine, SW = Stone-Wales, DV = diatom vacancies, SV = single vacancy</p>	75

LIST OF TABLES (Continued)

Table		Page
4.12	<p>E_{11} Photon absorption energy (PAE) in eV of pristine and defected SWCNTs. Abbreviations: P = pristine, SW = Stone-Wales, DV = diatom vacancies, SV = single vacancy, IS = impurity state,</p> <p>Shift = (PAE-defect) - (PAE-pristine)</p>	76
4.13	<p>E_{22} Photon absorption energy (PAE) in eV of pristine and defected SWCNTs. Abbreviations: P = pristine, SW = Stone-Wales, DV = diatom vacancies, SV = single vacancy, IS = impurity state,</p> <p>Shift = (PAE-defect) - (PAE-pristine)</p>	77

LIST OF FIGURES

Figure		Page
2.1	Schematic diagram of the calculation procedures	7
3.1	The 2D graphene sheet is shown along with the vectors which specify the chiral nanotubes	18
4.1	Pristine (8,0) SWCNT (a), (b) HOMO, (c) LUMO and (d) electronic band structure	24
4.2	Doped SWCNT model P-hyd-1, (a) no common HB (N-H...N) interactions, (b) N-H... π interactions, (c) orbital shapes of electronic band structure state (d)	25
4.3	Doped SWCNT model P-hyd-2, (a) common HB (N-H...N) interactions, (b) N-H... π interactions, (c) orbital shapes of electronic band structure state (d)	26
4.4	Doped SWCNT model P-hyd-3, (a) common HB (N-H...N) interactions, (b) N-H... π interactions, (c) orbital shapes of electronic band structure state (d)	27
4.5	Supplement data (a) P-hyd-3 model remained only <i>res3</i> , (b) P-hyd-3-CS model H point to N of <i>res3</i> , (c) and (d) are electronic band of (a) and (b) respectively	28

LIST OF FIGURES (Continued)

Figure		Page
4.6	Noncovalent Interaction (NCI) plot (b) of pristine (8,0) SWCNT (a), and (d) of gauche N ₂ H ₄ (c)	30
4.7	Noncovalent Interaction (NCI) plot (b) of N-H... π (a) interaction, and (d) of N-H...N (c) interaction	31
4.8	The intermolecular interaction, vdW interaction (a) of model P-hyd-1, the N-H...N (HB) and N-H... π interaction, (b) and (c) of model P-hyd-2 and P-hyd-3	32
4.9	DOS (PDOS) of hydrazine molecules with doped SWCNTs (arb. units)	33
4.10	¹³ C NMR δ of hydrazine doped SWCNTs of each interaction and electronic band structure, frequency (arb. units)	39
4.11	Selected ¹³ C NMR δ (a) and selected C atom (b) of vdW interaction of hydrazine doped SWCNT, frequency (arb. units), P-hyd-1	40
4.12	Selected ¹³ C NMR δ (a) and selected C atoms (b) of HB interaction of hydrazine doped SWCNT, frequency (arb. units), P-hyd-2	40
4.13	Selected ¹³ C NMR δ (a) and selected C atoms (b) of HB interaction of hydrazine doped SWCNT, frequency (arb. units), P-hyd-3	41
4.14	¹ H NMR δ of hydrazine doped SWCNTs, frequency (arb. units)	42

LIST OF FIGURES (Continued)

Figure		Page
4.15	Calculated photon absorption energy of (a) pristine (8,0) SWCNT, (b)-(d) doped SWCNT. The corresponding optical transition states, band structures, and density of states are shown on the right (e)-(h). The z axis is defined along the tube direction	46
4.16	Relevant molecular orbitals for E_{11} (A_{11} , B_{11}) optical transition of the pristine (8,0) SWCNT; (c), (e) the dipole-allowed transition and (d), (f) the dipole forbidden	47
4.17	Relevant molecular orbitals for E_{22} (A_{22} , B_{22}) optical transition of the pristine (8,0) SWCNT; (c), (e) the dipole-allowed transition and (d), (f) the dipole forbidden	49
4.18	Relevant molecular orbitals for E_{11} (A_{11}) optical transition of the doped (8,0) SWCNT P-hyd-1 model; (c) and (d) the dipole-allowed transition	51
4.19	Relevant molecular orbitals for E_{11} (B_{11}) optical transition of the doped (8,0) SWCNT P-hyd-1 model; (c) and (d) the dipole-allowed transition	52
4.20	Relevant molecular orbitals for E_{11} (A_{11}) optical transition of the doped (8,0) SWCNT P-hyd-3 model; (c) and (d) the dipole-allowed transition	53

LIST OF FIGURES (Continued)

Figure		Page
4.21	Relevant molecular orbitals for E_{11} (B_{11}) optical transition of the doped (8,0) SWCNT P-hyd-3 model; (c) and (d) the dipole-allowed transition	54
4.22	Schematic illustration of the structure of (a) pristine (8,0) SWCNT, (b) Single vacancy (SV) defect, (c) Diatom-vacancy (DV) defect and (d) Stone-Wales (SW) defect	63
4.23	Calculated photon absorption energy of (a) pristine (8,0) SWCNT, (b)-(d) defected SWCNT. The corresponding optical transition states, band structures, and density of states are shown on the right (e)-(h). The z axis is defined along the tube direction	64
4.24	Relevant molecular orbitals for E_{11} (A_{11}) optical transition of the pristine (8,0) SWCNT; (c) the dipole-allowed transition and (d) the dipole forbidden	67
4.25	Relevant molecular orbitals for E_{11} (B_{11}) optical transition of the pristine (8,0) SWCNT; (c) the dipole-allowed transition and (d) the dipole forbidden	68
4.26	Relevant molecular orbitals for E_{11} and E_{22} optical transitions of the single vacancy defect, SV, in (8,0) SWCNT; (c) the dipole-allowed E_{11} transition and (d) the dipole-allowed E_{22} transition	69

LIST OF FIGURES (Continued)

Figure		Page
4.27	Relevant molecular orbitals for E_{11} and E_{22} optical transitions of the diatom vacancy defect, DV, in (8,0) SWCNT; (c) the dipole-allowed E_{11} transition and (d) the dipole-allowed E_{22} transition	70
4.28	Relevant molecular orbitals for E_{11} and E_{22} optical transitions of the Stone-Wales defect, SW, in (8,0) SWCNT; (c) the dipole-allowed E_{11} transition and (d) the dipole-allowed E_{22} transition.....	71

LIST OF ABBREVIATIONS

TCF	Thin Conducting Film
PV	Photovoltaic
TCO	Transparent Conducting Oxide
ITO	Indium Tin Oxide
CNT	Carbon Nanotube
FOLED	Flexible Organic Light Emitting Device
SWCNT	Single-Walled Carbon Nanotube
DS	Donor State
DFT	Density Functional Theory
LDA	Local Density Approximation
GGA	Generalized Gradient Approximation
vdW	Van der Waals
DFT-D	Dispersion-corrected DFT
PBC	Periodic Boundary Condition
PAW	Projector Augmented-Wave
NMR	Nuclear Magnetic Resonance
GIPAW	Gauge-Including Projector Augmented-Wave
XPS	X-ray Photoelectron Spectroscopy
UV-Vis	Ultraviolet-Visibility
TDDFT	Time Dependent Density Functional Theory

LIST OF ABBREVIATIONS (Continued)

NCI	Noncovalent Interaction
SC	Steric Clashes
HB	Hydrogen Bond
PBE	Perdew-Burke-Ernzerhof
RDG	Reduced Density Gradient
DOS	Density Of State
IS	Impurity State
ISBMVS	Impurity State Below the Maximum Valence State
ISCMVS	Impurity State Close to the Maximum Valence State
PDOS	Projected Density Of State
HBN	Hydrogen Bond Network
HOMO	Highest Occupied Molecular Orbital
LUMO	Lowest Unoccupied Molecular Orbital
PAE	Photon Absorption Energy

CHAPTER I

INTRODUCTION

1.1 Introduction

Thin conducting film (TCF) electrodes are important parts of photovoltaic (PV) devices and other optoelectronic devices; utilizing as p-type (hole-collecting electrode) and n-type (electron-collecting electrode) semiconductors. Currently, transparent conducting oxides (TCO) play a major role in such devices. Typical TCO materials are In_2O_3 , SnO_2 or ZnO , which are normally doped into n-type by dopants. Today, the most commercialized n-type TCO material is indium tin oxide (ITO) with tin of about 10 wt%. Early report of a p-type TCO semiconductor was on NiO in 1997 (Kodama *et al.*, 1997). Concurrently, the discovery of p-type conductivity in CuAlO_2 (Kawazoe *et al.*, 1997) led to the studies of many Cu(I) based delafossites that are simultaneously transparent and (p-type) conducting, such as CuScO_2 , CuYO_2 , CuInO_2 , CuGaO_2 and CuCrO_2 . Beside oxides for TCF materials, carbon nanotubes (CNTs) have been studied. CNTs have covalent bonding which does not suffer from electromigration a common problem that leads to the failure in thin metal conductors. In addition, CNTs are thermally stable and highly resistant to chemical damage. Therefore, CNTs that are flexible and transparent organic material is a potential candidate to replace conventional ITO in the next generation optoelectronic devices. Because CNTs films are flexible,

they can be used in flexible organic light emitting devices (FOLEDs). (Mistry *et al.*, 2011; Sohn and Han, 2011).

Single-walled carbon nanotubes (SWCNTs) can be used in nanotube electronics devices (McEuen *et al.*, 2002; Komarov and Mironov, 2004), energy storage devices (Rashidi *et al.*, 2010), memory devices (Cui *et al.*, 2002), chemical sensors (Kong *et al.*, 2000), biotechnology (Bekyarova *et al.*, 2005), and coatings and films (Kaempgen *et al.*, 2005; Han and Zettl, 2003). The n-type and p-type semiconductors are the foundation of diodes, and the diode is mandatory in electronic devices. Because the transparent oxide such as ZnO (n-type) and CuAlO₂ (p-type) are not flexible (Ohta and Hosono, 2004), they have limited use in flexible electronic devices (Zhang *et al.*, 2006; Unalan *et al.*, 2008; Mirri *et al.*, 2012). For such purpose, CNTs that are transparent and highly conductive are produced (Wu *et al.*, 2004; De Volder *et al.*, 2013). The potential applications of CNTs are photovoltaic devices (Gabor *et al.*, 2009; Barkelid and Zwiller, 2013), diodes (Mueller *et al.*, 2010; Jena *et al.*, 2008) and thermoelectric materials (Freeman *et al.*, 2012; Nonoguchi *et al.*, 2013), and other optoelectronic devices (Rana *et al.*, 2014; Xia *et al.*, 2010; Champlain, 2011). Chemical doping with Boron (B) dopant (Williams *et al.*, 2007) results in the hybridization of C and B (Bai and Zhou, 2007) atoms which leads to the sp^3 preference. It is a challenge to maintain sp^2 hybridization (physisorption) B-doped CNTs for the flexible properties. The physisorption doping process of poly(ethylene imine) (PEI) (Shim *et al.*, 2001; Kong and Dai, 2001) is unstable in air and transforms the material from n-type semiconductors to intrinsic semiconductors (Tomohiro *et al.*, 2014). The theoretical study of hydrazine (N₂H₄) and water (H₂O) doped SWCNT shows n-type behavior (Yu *et al.*, 2011). The experimental results of SWCNT doped by the amine group (R-NH₂;

hydrazine, methylamine, ethylenediamine and polyethylenimine), also showed that hydrazine is an effective n-type dopant for SWCNT on the basis of its conductivity and optical transparency. However, it is unstable in air (Mistry *et al.*, 2011). To characterize the role of water molecules, synchrotron transient photoelectron spectroscopy was used to study C-N bonds (Wang *et al.*, 2013). The absorption and luminescence of SWCNT depends on the chiral index of SWCNT (Weisman and Bachilo, 2003; Avouris *et al.*, 2008). When an intrinsic semiconductor is transformed to an n-type or a p-type semiconductor, its absorption changes which could affect its optoelectronic properties (Mu *et al.*, 2013; Liu *et al.*, 2012).

Experimentally, the amine group were used to dope CNTs by various doping processes. The adsorption of organic molecules on SWCNT under ambient conditions was done by exposing the sample to the vapor of the molecules. This leads to n-type SWCNT (Kong and Dai, 2001). SWCNT submerged in a 20 wt% solution of PEI in methanol also turned into an n-type semiconductor (Shim *et al.*, 2001). The SWCNT soaked in hydrazine in a helium glove box also shown n-type property (Mistry *et al.*, 2011).

A monolayer of water molecules and hydrazine molecules covering the surface of SWCNT is necessary for the donor states (DS) to form (Chakrapani *et al.*, 2007). Water is somehow necessary for the charge to transfer from hydrazine to SWCNT (Desai *et al.*, 2010). To understand DS of hydrazine-doped SWCNT by computation, hydrazine molecules were added one-by-one onto the SWCNT surface (Yu *et al.*, 2011). However, in that particular case, there was no DS formed. DS only formed after water was added to hydrazine and SWCNT; indicating that water is necessary for the DS to form in hydrazine-doped SWCNT.

In this study we found that SWCNT doped purely with hydrazine could also have DS without the aid of water; providing that the hydrazine is properly binding with SWCNT in a specific manner. The configuration of hydrazine which causes the occurrence of DS is investigated. Understanding how DS occurs will help designing n-type SWCNT that is stable in air.

1.2 Research objectives

A problem of flexible transparent conducting film based on SWCNT is that they are unstable in air. An understanding of the charge transfer mechanism of intermolecular interactions may be useful in modifying and solving this problem. The purpose of this thesis is to investigate hydrazine doped SWCNT to understand the mechanisms that leads to the conduction. Following properties will be studied: the electronic band structures, the ^{13}C nuclear magnetic resonance (NMR) chemical shifts and the Ultraviolet-visibility (UV-Vis) spectroscopic parameters. The later two properties, i.e., ^{13}C NMR chemical shifts and UV-Vis spectroscopic parameters can be used for comparison with experiments to confirm the theoretical models.

1.3 Scope and limitations

The computations will be carried out by using first-principle calculations based on the density functional theory (DFT) (Hohenberg and Kohn, 1964; Kohn and Sham, 1965) by the plane wave method (Callaway, 1955) that was implemented in the Quantum ESPRESSO package (Paolo *et al.*, 2009). The form of exchange correlation

energy in Kohn-Sham is treated according to the Perdew-Burke-Ernzerhof (PBE) approach (Perdew *et al.*, 1996). The van der Waals (vdW) interaction is described by the post Hartree-Fock (post-HF) method (Barone *et al.*, 2009). The NMR chemical shifts will be calculated by using the gauge-including projector augmented-wave (GIPAW) approach (Mauri *et al.*, 1996; Pickard and Mauri, 2001). The absorption spectra will be calculated by using time-dependent density functional theory (TDDFT) by the Liouville-Lanczos approach (Malcioğlu *et al.*, 2011).

The mechanisms and spectroscopic spectra of hydrazine doped SWCNTs will be investigated. The calculated ^{13}C NMR chemical shifts can be used to compare with actual experimental measurements to confirm the geometry of the atomic models and the associated electronic band structure states. The intermolecular interaction will be described by using reduced density gradient (RDG) of the electron densities to describe noncovalent interactions (NCI) between hydrazine and SWCNTs. The optical transition of hydrazine doped SWCNTs will be described by using TDDFT.

The limitations of this study are the size of the system that can be studied and the accuracy of the computations. Both factors are due to the current computational limits and available computational tools. Regarding the size, current computational resources can deal with the system size of the order of 100 atoms. Regarding the accuracy, currently first principles calculations are calculating only the ground states and many-body interactions are simplified using DFT and exchange-correlation interactions terms. The dynamical properties are limited to the accuracy of the quantum Monte Carlo theory which we use the CASINO package implemented in the Quantum ESPRESSO suite (<https://vallico.net/casinoqmc/>).

CHAPTER II

COMPUTATIONAL METHODS

2.1 Research Methods

The calculations were carried out by using the Quantum ESPRESSO suite with the Rappe Rabe Kaxiras Joannopoulos method. The calculations are based on density functional theory with pseudopotentials plane-wave approach. To allow computations of large systems the ultra-soft version of pseudopotentials is employed with the Perdew-Burke-Ernzerhof exchange-correlation function. The Bader charge analysis was calculated by using the Projector Augmented-Wave (PAW) method with PBE exchange-correlation function. The plane-wave energy cutoff for the plane-wave basis sets was set to 30 Ry for electronic band structure calculations, structural optimization and TDDFT calculations, 45 Ry for NMR calculations (GIPAW) and 55 Ry for Bader charge analysis.

In this study, we calculated the geometry and the electronic configurations at the ground state to explain the properties of the systems. Firstly, we calculated the cell optimization of SWCNTs. Then we calculated the ionic optimization and, finally, we calculated the electronic optimization. The optimized electronic configuration can be used to calculate the bands, density of state (DOS), ^{13}C NMR chemical shifts and absorption spectra. For the hydrazine doped SWCNT we repeat similar steps with the starting SWCNT structure from the converged pure SWCNT. The procedures described

above are shown in Figure 2.1, with tags according to terminologies in the Quantum ESPRESSO package, i.e., *vc-relax* is a variable cell relaxation that is used for cell optimization, *relax* is used for ionic optimization, and *scf* is a self-consistent field used for electronic optimization.

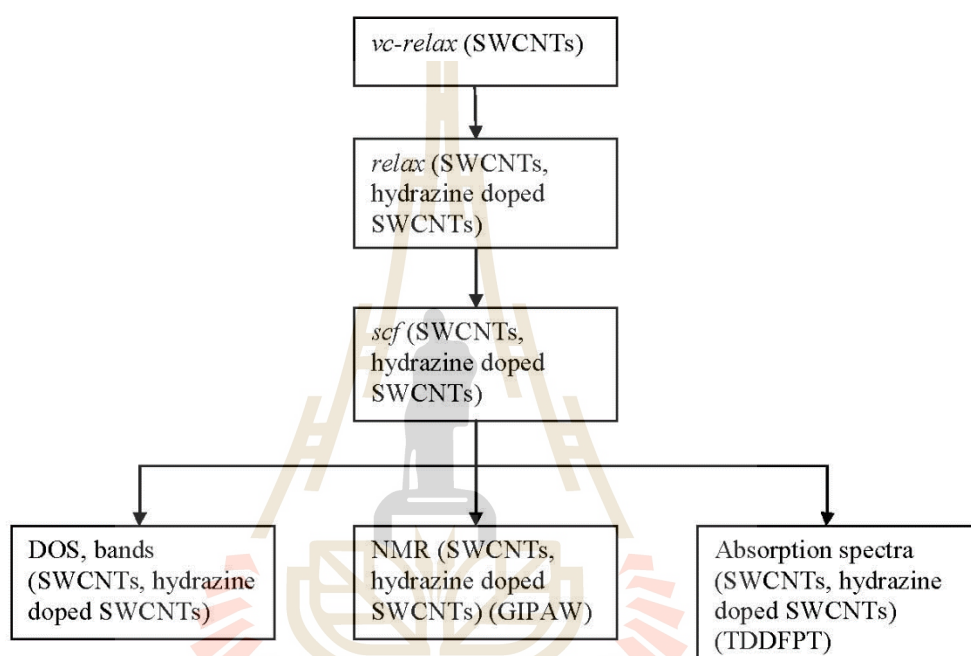


Figure 2.1 Schematic diagram of the calculation procedures.

2.2 Density functional theory

Density functional theory (DFT) is a ground-state theory in which the emphasis is on the charge density as the relevant physical property.

2.2.1 The Hohenberg and Kohn theorem

The ground-state energy and all electron properties of the many electron wave-functions in the presence of an external potential can be determined from the electron density, $n(\vec{r})$. When the coulomb-interacting particles move in an external potential $V_{ext}(\vec{r})$, the ground-state energy can be obtained by minimizing the energy functional. The ground-state of many electron wave-functions can be written as (Hohenberg and Kohn, 1964),

$$E_v[n(\vec{r})] \equiv \int V_{ext}(\vec{r})n(\vec{r})d\vec{r} + F[n(\vec{r})], \quad (2.1)$$

where $V_{ext}(\vec{r})$ is an external potential generated by the nuclei acting on the electrons. $F[n(\vec{r})]$ is an universal functional of electron density, independent of the external potential $V_{ext}(\vec{r})$. The functional $F[n(\vec{r})]$ includes all kinetic and electron-electron interaction terms.

2.2.2 Kohn and Sham equation

Kohn and Sham (Kohn and Sham, 1965) proposed that the Hohenberg and Kohn expression can be written as,

$$E[n(\vec{r})] = \int V_{ext}(\vec{r})n(\vec{r})d\vec{r} + \frac{e^2}{2} \iint \frac{n(\vec{r})n(\vec{r}')}{|\vec{r}-\vec{r}'|} d\vec{r}d\vec{r}' + T_s[n(\vec{r})] + E_{xc}[n(\vec{r})], \quad (2.2)$$

where $\frac{e^2}{2} \iint \frac{n(\vec{r})n(\vec{r}')}{|\vec{r}-\vec{r}'|} d\vec{r}d\vec{r}'$, is the electron-electron Coulomb energy, which is called Hartree energy. $T_s[n(\vec{r})]$ is the kinetic energy of a non-interacting system with the same density. $E_{xc}[n(\vec{r})]$ is the exchange-correlation energy. Thus the Kohn-Sham (KS)-effective potential can be written as,

$$V_{eff}(\vec{r}) = V_{ext}(\vec{r}) + e^2 \int \frac{n(\vec{r}')}{|\vec{r}-\vec{r}'|} d^3r' + \frac{\delta E_{xc}[n(\vec{r})]}{\delta n}. \quad (2.3)$$

The one-particle Schrödinger equation or Kohn-Sham equation can be written as,

$$\left[-\frac{\hbar^2}{2m} \nabla^2 + V_{eff}(\vec{r})\right] \psi_i(\vec{r}) = \epsilon_i \psi_i(\vec{r}). \quad (2.4)$$

The electron density of the system is given by,

$$n(\vec{r}) = \sum_{i=1}^N |\psi_i(\vec{r})|^2, \quad (2.5)$$

where N is the number of electrons.

2.2.3 The local density approximation (LDA)

To solve the one-particle Schrödinger equation, $E_{xc}[n(\vec{r})]$ must be approximated. The most basic approximation of $E_{xc}[n(\vec{r})]$ is the local density approximation (LDA), which is derived from a homogeneous electro gas model. The local density approximation for the exchange correlation energy can be written as (Kohn, 1999),

$$E_{xc}^{LDA}[n(\vec{r})] = \int n(\vec{r}) \epsilon_{xc}[n(\vec{r})] d^3r, \quad (2.6)$$

where $\epsilon_{xc}[n(\vec{r})]$ is the exchange correlation energy per particle of homogeneous electron gas with the density $n(\vec{r})$.

2.2.4 The generalized gradient approximation (GGA)

The generalized gradient approximation (GGA) is introduced to treat the variations of electron density in space. The exchange-correlation energy E_{xc} is a function of the local electron density, $n(\vec{r})$ and their gradients $|\nabla n(\vec{r})|$ (Kohn, 1999),

$$E_{xc}^{GGA}[n(\vec{r})] = \int f[n(\vec{r}), \nabla n(\vec{r})] n(\vec{r}) d^3r. \quad (2.7)$$

2.2.5 Van der Waals (vdW) interaction

The DFT with the LDA and semilocal GGA is not only successful in numerous applications for individual molecules and dense solids, it has also been developed, for instance, in order to include nonlocal effects, such as the vdW force (Rydberg *et al.*, 2000). The vdW force between two atoms or two molecules arises from interaction induced dipole moments, because of the electron densities. However, vdW forces are non-classical and non-local interactions that need a proper treatment for electronic dynamic correlation. This can be achieved by the so-called post Hartree-Fock (post-HF) method (Barone *et al.*, 2009). For the dispersion-corrected DFT (DFT-D) approach, the energy can be written as,

$$E_{DFT-D} = E_{DFT} + E_{disp}, \quad (2.8)$$

$$E_{disp} = -\frac{1}{2} \sum_{ij} C_{6ij} [\sum_{\vec{R}} |\vec{r}_{ij} + \vec{R}|]^{-6} f_{damp}(|\vec{r}_{ij} + \vec{R}|), \quad (2.9)$$

$$f_{damp}(|\vec{r}_{ij} + \vec{R}|) = S_6 \cdot \left\{ 1 + \exp \left[-d \cdot \left(\frac{|\vec{r}_{ij} + \vec{R}|}{r_0} - 1 \right) \right] \right\}^{-1}, \quad (2.10)$$

where $\vec{r}_{ij} = (\vec{r}_i - \vec{r}_j)$ is the atom-atom distance vector, $\vec{R} (= l\vec{a} + m\vec{b} + n\vec{c})$ are lattice vectors, S_6 is a functional-dependent scaling parameter, d is a parameter that tunes the steepness of the damping function and C_{6ij} is the coefficient computed for each pair of atoms, r_0 is vdW radii of the atom pairs ($r_0 = r_{0i} + r_{0j}$).

2.2.6 Gauge including projector augmented wave method (GIPAW)

The nuclear magnetic moment ($\vec{\mu}_i$) is related to the nuclear spin \vec{I}_i of the nucleus by

$$\vec{\mu}_i = \gamma \vec{I}_i \quad (2.11)$$

where γ is the gyromagnetic ratio, a constant of a given type of nucleus. The applied magnetic field is generated \vec{B}_{ext} and is taken to be along z of the laboratory frame of reference, i.e. $\vec{B} = (0,0,B_{ext})$ in the $\omega = \gamma B$ equation. The frequency with the $\vec{\mu}_i$ precesses about this field is defined as ω_0 , the *Larmor frequency*: (Duer, 2005)

$$\omega_0 = -\gamma B_{ext}. \quad (2.12)$$

The hamiltonian \hat{H} for a nuclear spin in a static field is

$$\hat{H} = -\hat{\mu} \cdot \vec{B}_{ext} \quad (2.13)$$

where $\hat{\mu}$ is the nuclear magnetic moment operator and \vec{B}_{ext} is the magnetic field applied in the NMR experiment. This hamiltonian is often referred to as the *Zeeman hamiltonian*. The $\hat{\mu}$ can be written in term of the nuclear spin operator \hat{I} :

$$\hat{\mu} = \gamma \hbar \hat{I}. \quad (2.14)$$

The applied field is taken to be along z , so combining Equation (2.13) and (2.14), we have

$$\hat{H} = -\gamma \hbar \vec{I}_z B_{ext}. \quad (2.15)$$

If we consider \vec{B} as the field at the nucleus due to the presence of an externally applied field \vec{B}_{ext} we can express *Zeeman hamiltonian* (Equation (2.15)) as (Bonhomme *et al.*, 2012):

$$\hat{H} = -\gamma_i \hbar \vec{I}_{i,z} (1 - \vec{\sigma}_i) B_{ext}. \quad (2.16)$$

The shielding tensor can equivalently be written as a second derivative of the electronic energy of the system:

$$\vec{\sigma}_i = \frac{\partial^2 E}{\partial \vec{\mu}_i \partial \vec{B}_{ext}}. \quad (2.17)$$

The change in resonant frequency, a normalized chemical shift is reported: (ν_{ref} is the resonance frequency of reference)

$$\delta = \frac{\nu_{sample} - \nu_{ref}}{\nu_{ref}}. \quad (2.18)$$

The magnetic shielding and chemical shift are related by:

$$\delta = \frac{\sigma_{ref} - \sigma_{sample}}{1 - \sigma_{ref}}. \quad (2.19)$$

For all but very heavy elements, $|\sigma_{ref}| \ll 1$ and so:

$$\delta \approx \sigma_{ref} - \sigma_{sample}. \quad (2.20)$$

The *ab initio* computation of NMR chemical shifts in condensed matter systems is calculated by using periodic boundary conditions (PBC) through an extension of Blöchl's projector augmented-wave (PAW) approach which is called the gauge-including projector augmented-wave (GIPAW) approach and it was introduced by Mauri *et al.* (Mauri *et al.*, 1996; Pickard and Mauri, 2001). The GIPAW is implemented in the Quantum ESPRESSO package (Paolo *et al.*, 2009) with a uniform external field \vec{B}_{ext} applied to a sample which induces an electronics current density, $\vec{J}_{in}(\vec{r})$. The current produces an induced magnetic field, $\vec{B}_{in}(\vec{r})$. If \vec{B}_{ext} is small enough a condition is realized in the NMR experiment, so

$$\vec{B}_{in}(\vec{r}) = -\vec{\sigma}(\vec{r})\vec{B}_{ext}, \quad (2.21)$$

where $\vec{\sigma}(\vec{r})$ is the magnetic shielding tensor. With NMR spectroscopy, it is possible to measure the symmetric part of $\vec{\sigma}(\vec{r})$ or more often its trace,

$$\sigma(\vec{r}) = \frac{1}{3} \text{Tr}[\vec{\sigma}(\vec{r})] \quad (2.22)$$

at the position of the nonzero spin nuclei. For a periodic system,

$$\vec{\sigma}(\vec{r}) = \sum_{\vec{G}} \vec{\sigma}(\vec{G}) e^{i\vec{G} \cdot \vec{r}} \quad (2.23)$$

is a bulk property. The induced field $\vec{B}_{in}(\vec{r})$ tensor is calculated from the induced current using the Biot-Savart Law (Ren *et al.*, 2013):

$$\vec{B}_{in}(\vec{r}) = \frac{1}{c} \int d\vec{r}' \vec{j}_{in}(\vec{r}') \times \frac{\vec{r}' - \vec{r}}{|\vec{r}' - \vec{r}|^3} \quad (2.24)$$

where c is the speed of light. For non-periodic conditions, $\vec{B}_{in}(\vec{G} = 0) = 4\pi\alpha\chi_v\vec{B}_{ext}$, $\sigma(0) = -4\pi\alpha\chi_v$, where α is the diagonal tensor that depends on the macroscopic shape, χ_v is the magnetic volume susceptibility tensor. For CNT with a cylindrical shape, $\alpha_{xx} = \alpha_{yy} = 1/2$ and $\alpha_{zz} = 2/3$, where the tube axis is along the z direction (Marques *et al.*, 2006). The chemical shift changes ($\Delta\delta_{induce}$) induced by a magnetic field is calculated by using the negative value of the isotropic shielding constants of σ_{iso} in the same positions as for molecules in an empty nanotube. σ_{iso} is calculated from the diagonalized symmetric part of the magnetic shielding tensor $\vec{\sigma}(\vec{r})$:

$$\Delta\delta_{induce} = -\sigma_{iso}(\vec{r}) = -\frac{1}{3} \text{Tr}[\vec{\sigma}(\vec{r})]. \quad (2.25)$$

2.2.7 Time dependent density functional perturbation theory (TDDFPT)

The perturbation induces a transition from the initial N -electron ground state $|N\rangle$ to the final state $|N - 1, m; \vec{k}\rangle$. The final state is represented by a system with the

photoelectron with momentum \vec{k} and the sample in the excited state m with $N-1$ electrons. The energy conservation, it is required that the photon energy ω is equal to the kinetic energy of the photoelectron $E_{\vec{k}}$ minus the electron removal energy, $E_m = E(N) - E(N-1, m)$; $\omega = E_{\vec{k}} - E_m$. The photoemission matrix elements set to a constant $\bar{\xi}$, so the total photocurrent written as;

$$J_{\vec{k}}(\omega) = |\bar{\xi}|^2 \sum_i^{occ} \delta(E_{\vec{k}} - \omega - E_i) \quad (2.26)$$

for series of delta peaks in correspondence to the energies E_i of the one-particle Hamiltonian. The photoemission spectrum is hence described by the density of occupied (occ) state:

$$DOS(E_{\vec{k}} - \omega) = \sum_i^{occ} \delta(E_{\vec{k}} - \omega - E_i), \quad (2.27)$$

evaluated at the energy $E_{\vec{k}} - \omega$ (Marques *et al.*, 2012).

Time-dependent density functional theory (TDDFT) is a powerful method for the numerical simulation of optical spectra in a variety of molecular systems, which uses the Liouville-Lanczos method. This is a method that allows for the full-spectrum of a system to be calculated over a broad frequency range (Malcioğlu *et al.*, 2011). In the dipole approximation, the response of the molecular system to the electromagnetic radiation ($V'_{ext}(\vec{r}, \omega) = -\vec{E}(\omega) \cdot \vec{r}$) is described by the dynamical polarizability tensor, $\alpha_{ij}(\omega)$, whose elements are defined as the dipole moment linearly induced along the i -th Cartesian direction by perturbing electric fields of unit strength, polarized along the j -th axis, and oscillating at the frequency ω . The absorption coefficient is essentially the product of frequency times the imaginary part of the diagonal element (or trace) of

the polarizability. The polarizability of a system of interacting electrons can be expressed as:

$$\alpha_{ij}(\omega) = Tr(\hat{X}_i \hat{\rho}'_j(\omega)), \quad (2.28)$$

where carets indicate quantum mechanical operators, \hat{X}_i is the i -th component of the dipole (or position) operator, $\hat{\rho}'_j(\omega) = \hat{\rho}_j(\omega) - \hat{\rho}^0$ is the response density matrix $\hat{\rho}_j(\omega)$ being the one electron density matrix of the system perturbed by an external homogeneous electric field of unit strength polarized along the j -th Cartesian axis and oscillation at frequency ω , and $\hat{\rho}^0$ is its unperturbed counterpart. The relationship between dipole moment (μ_i), polarizability (α_{ij}) and electric field (E_j) can be written as,

$$\begin{pmatrix} \mu_x \\ \mu_y \\ \mu_z \end{pmatrix} = \begin{pmatrix} \alpha_{xx} & \alpha_{xy} & \alpha_{xz} \\ \alpha_{yx} & \alpha_{yy} & \alpha_{yz} \\ \alpha_{zx} & \alpha_{zy} & \alpha_{zz} \end{pmatrix} \begin{pmatrix} E_x \\ E_y \\ E_z \end{pmatrix}, \quad (2.29)$$

for the balance of force, $-m_e \omega_0^2 x = eE$, and the dipole moment is,

$$\mu_{ind} = \frac{e^2}{m_e \omega_0^2} E = \alpha E. \quad (2.30)$$

Each electron has an intrinsic harmonic oscillator frequency (Hartree units: $\hbar = 1$; $e = 1$; $m_e = 1$). The polarizability for all electrons is,

$$\bar{\alpha}(\omega) = \frac{1}{3} Tr \alpha(\omega) = \sum_j \frac{f_j}{(E_j - E_0)^2 - \omega^2}. \quad (2.31)$$

The quantity f_j is the oscillator strength which is a classical formalism, f_{ij} is proportional to the intensity of a transition $i \rightarrow j$. Thus, $\sum_j f_{ij} = 1$, the spectroscopic oscillator strengths defined as,

$$f_{0j} = \frac{2}{3}(E_j - E_0)(|\langle \Psi_0 | \hat{x} | \Psi_j \rangle|^2 + |\langle \Psi_0 | \hat{y} | \Psi_j \rangle|^2 + |\langle \Psi_0 | \hat{z} | \Psi_j \rangle|^2). \quad (2.32)$$



CHAPTER III

LITERATURE REVIEWS

3.1 Single-walled carbon nanotubes (SWCNTs)

It is convenient to specify a general carbon nanotube with a tubule diameter d_t and the chiral angle θ , which are shown in Figure 3.1. The chiral vector \vec{C}_h is defined in terms of the integers (n,m) and the basis vectors \vec{a}_1 and \vec{a}_2 of the honeycomb lattice. A unit cell of carbon nanotube is shown in Figure 3.1 with the rectangle bounded by the vector \vec{C}_h and \vec{T} , where \vec{T} is the 1D translation vector of the nanotube. The vector \vec{T} is normal to \vec{C}_h and extends from the origin to the first lattice point B in the honeycomb lattice. The carbon nanotube behaves like the rolled-up cylinders of a graphene sheet of sp^2 bonded carbon atom (Dresselhaus *et al.*, 1995). When $n = m$ called armchair (n,n) , when $m = 0$ called zigzag $(n,0)$ and when $n \neq m$ called chiral (n,m) . They are metallic nanotubes when $\text{mod}(n-m,3) = 0$, and semiconducting nanotubes when $\text{mod}(n-m,3) = 1$ or 2 (Liu *et al.*, 2012), and the definition can be written as,

$$\vec{C}_h = n\vec{a}_1 + m\vec{a}_2, \vec{T} = t_1\vec{a}_1 + t_2\vec{a}_2, t_1 = \frac{2m+n}{d_R}, t_2 = -\frac{2n+m}{d_R}, \quad (3.1)$$

d : the highest common of (n,m)

d_R : the highest common of $(2n+m, 2m+n)$

$d_R = d$ if $n - m$ not a multiple of $3d$

$$d_R = 3d \text{ if } n - m \text{ a multiple of } 3d$$

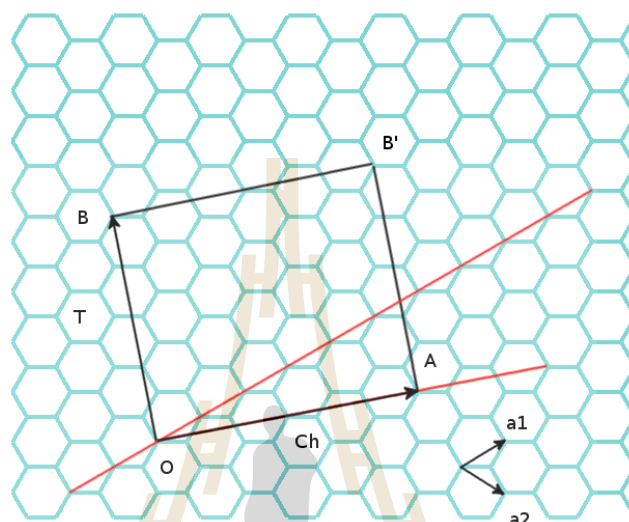


Figure 3.1 The 2D graphene sheet is shown along with the vectors which specify the chiral nanotubes.

3.2 Hydrazine

Hydrazine is a polymeric amine group ($R-NH_2$) with a molecule formula of N_2H_4 , which is a colorless, flammable liquid and a highly toxic inorganic compound. Its boiling point is $114\text{ }^\circ\text{C}$ and the dipole moment is 1.85 D (Debye, $1\text{ D} = 3.336 \times 10^{-30}$ Coulomb.meters). Hydrazine is a polar molecule with 2 lone pair electrons, the gauche

conformation is the most stable form of hydrazine in the gas phase (Daff and de Leeuw, 2011).

3.3 Hydrazine doped SWCNTs

The CNTs and TCFs are both p-type and n-type, flexible and non-flexible TCFs. Most non-flexible TCF are doped with elements, while most flexible TCF are doped with organic molecules. Dopants for the non-flexible TCFs are, for example, Ag and Ni which are used for doping SWCNTs as p-type TCF (Oh *et al.*, 2012). Dopants for flexible TCFs are, for example, nitric acid which is used for doping SWCNTs as p-type TCFs (Shin *et al.*, 2009), while dopants, such as hydrazine, methylamine, ethylenediamine and polyethylenimine are used for doping n-type TCFs. The amines group (hydrazine, methylamine, ethylenediamine and polyethylenimine) was used for doping SWCNTs to make the physisorbed hydrazine an effective dopant for SWCNTs when used in an inert environment, then used a combination of Raman spectroscopy, X-ray photoelectron spectroscopy (XPS) and nuclear magnetic resonance (NMR) to investigate the mechanisms underlying the interaction of amines with the SWCNT network: the film of SWCNT was soaked in 4 M hydrazine overnight in a helium glovebox and then the film was exposed to the air as reported by Mistry *et al.* (Mistry *et al.*, 2011).

Theoretical investigation, for a sparse matter vdW force plays an important role in numerous physical, chemical and biological systems (Rydberg *et al.*, 2000). The vdW interaction of organic molecule-metal junctions and the adsorption of thiophene on Cu(111) were studied by Sony *et al.* (Sony *et al.*, 2007), and the polyethylene and

graphite crystals were studied by Barony *et al.* (Barone *et al.*, 2009). To confirm the configuration of hydrazine doped SWCNTs, the ^{13}C NMR chemical shifts were used as reported by Mistry *et al.* (Mistry *et al.*, 2011). The relationship between diameter, electronics structure and ^{13}C NMR chemical shifts of SWCNTs were studied by Engtrakul *et al.* (Engtrakul *et al.*, 2012) and the ^{13}C NMR chemical shifts of functionalized SWCNTs were studied by Zurek *et al.* (Zurek *et al.*, 2007). The intermolecular form of hydrazine physisorbs on the surface of SWCNTs is a noncovalent interaction (NCI), which behave according to van der Waals (vdW), steric clashes (SC) and hydrogen bonds (HBs). Various kinds of NCI were investigated using the reduced density gradient (RDG) approach (Ren *et al.*, 2013; Johnson *et al.*, 2010; Contreras-García *et al.*, 2011). UV-vis is a property of optical transition in SWCNTs, for example ($\pi \rightarrow \pi^*$) was studied by Movlaroooy *et al.* and Saidi and Norman (Movlaroooy *et al.*, 2010; Saidi and Norman, 2014). The π - π interaction can be employed to open the band gap of graphene, SWCNTs, and graphene oxide as studied by Zhang and Shao (Zhang and Shao, 2014). The electron-electron interaction shifts the optical resonance energies by the same amount for both metallic and semiconducting nanotubes, and this shift increases monotonically with the nanotube diameter as was studied by Liu *et al.* (Liu *et al.*, 2012). The definition of RDG can be written as,

$$s = \frac{1}{2(3\pi^2)^{1/2}} \frac{|\nabla n(\vec{r})|}{n(\vec{r})^{4/3}} \quad (3.2)$$

CHAPTER IV

RESULTS

4.1 Configurations

In this study the intermolecular interaction is a noncovalent interaction, the configuration of intermolecular interaction is important for electronic band structure state, because it induce the electron charge transfer that can or cannot inject the electron into the SWCNT. Then we focused on relevant configuration for each electronic band structure state.

4.1.1 Configurations and electronic band structures

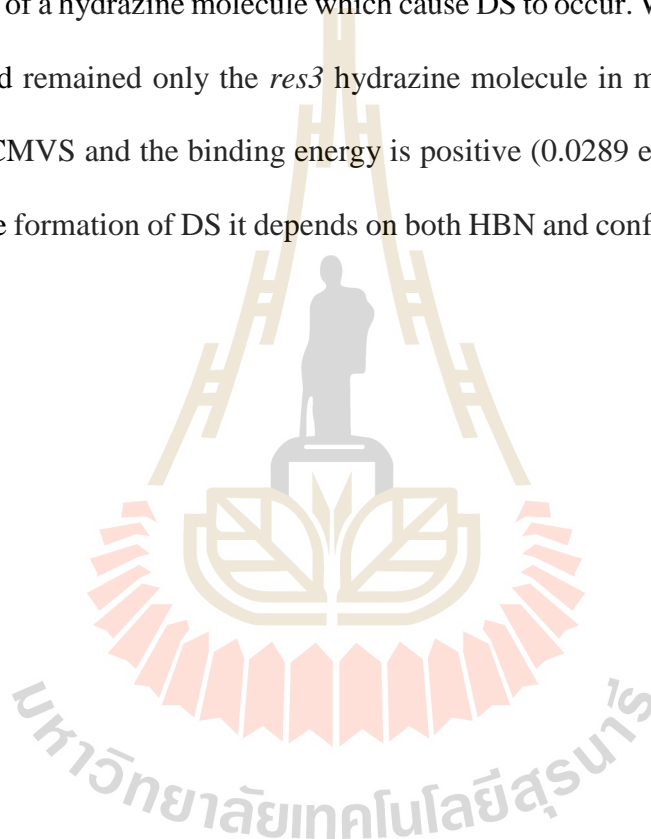
A pristine (8,0) SWCNT with 3 primitive cells (96 C atoms) is used and placed in a tetragonal cell with a and b equal to 21.0083 Å, and c/a equal to 0.6086. The diameter of the pristine SWCNT is 6.3591 Å. The electronic band gap of the pristine SWCNT is 0.596 eV (0.60 eV; Ref. (Spataru *et al.*, 2004)). The vdW (Rydberg *et al.*, 2000) was corrected by the post Hartree-Fock (post-HF) (Barone *et al.*, 2009) method. The charge transfer analysis was analyzed by using the Bader charge analysis (Bader *et al.*, 1987; Tang *et al.*, 2009; Henkelman *et al.*, 2006). The intermolecular interaction was described by using the RDG approach to investigate the NCI (Johnson *et al.*, 2010; Contreras-García *et al.*, 2011). The atomic force was less than 2×10^{-4} Ry/a.u. for pure SWCNT, and were less than 4×10^{-3} Ry/a.u. for doped SWCNTs.

The electronic band structures are classified according to three groups, first, the impurity state below the maximum valence state (ISBMVS), second, the impurity state close to (below) the maximum valence state (ISCMVS) and, third, the DS as shown in Figure 4.2d, 4.3d and 4.4d, respectively.

The electronic band structure state is shown in Table 4.1. The hydrazine doped SWCNT which is transformed from intrinsic to n-type semiconductors was investigated by using the Bader charge analysis to analyze the charge transfer. The charge transfer mechanism was explained by using the RDG of NCI and the projected density of state (PDOS) was used to consider the molecular orbital in terms of the atomic orbital. The electronic band structure of the ISBMVS is shown in Figure 4.2d. There are two impurity states (ISs) at -3.8857 and -3.8972 eV (blue solid line) and no electron is injected into the SWCNT (Table 4.3; $-0.00(27) e^{-1}$ unit). The distance between H and C atoms is 2.67 Å which is not close enough to obtain the HB. Instead, it is the vdW region as shown in Figure 4.8a. The electronic band structure of the ISCMVS is shown in Figure 4.3d, the configuration of two hydrazine molecules doped SWCNTs is shown in Figure 4.3b. The shortest distance between C and H atoms is 2.50 Å, the distances of the hydrazine hydrogen bond network (HBN) is 2.16 Å. When the HBN occurs, the distance between C and H atoms is shorter than in the case of a hydrazine molecule (2.67 Å). This is the cause for the shifting of IS to -3.2777 eV (close to maximum valence state). The blue planar between molecules represents the HB is shown in Figure 4.3a and the HB in the blue region is shown in Figure 4.8b. The electronic band structure of the DS is shown in Figure 4.4d, the configuration of 3 hydrazine molecules doped SWCNTs is shown in Figure 4.4b. The shortest distance between C and H atoms

is 2.43 Å. The distances of the hydrazine HBN are 1.99 and 2.01 Å. The DS is -2.5678 eV, and the blue planar between molecules represents the HB is shown in Figure 4.4a and the HB in the blue region is shown in Figure 4.8c.

The hydrazine molecules which cause the formation of DS. The H atoms are point to the N atoms of another molecule. Consider the DS depend only on the configuration of a hydrazine molecule which cause DS to occur. We removed hydrazine molecules and remained only the *res3* hydrazine molecule in model P-hyd-3, the DS moved to ISCMVS and the binding energy is positive (0.0289 eV; $E_{int} = -0.1641$ eV). Therefore, the formation of DS it depends on both HBN and configuration (Figure 4.5).



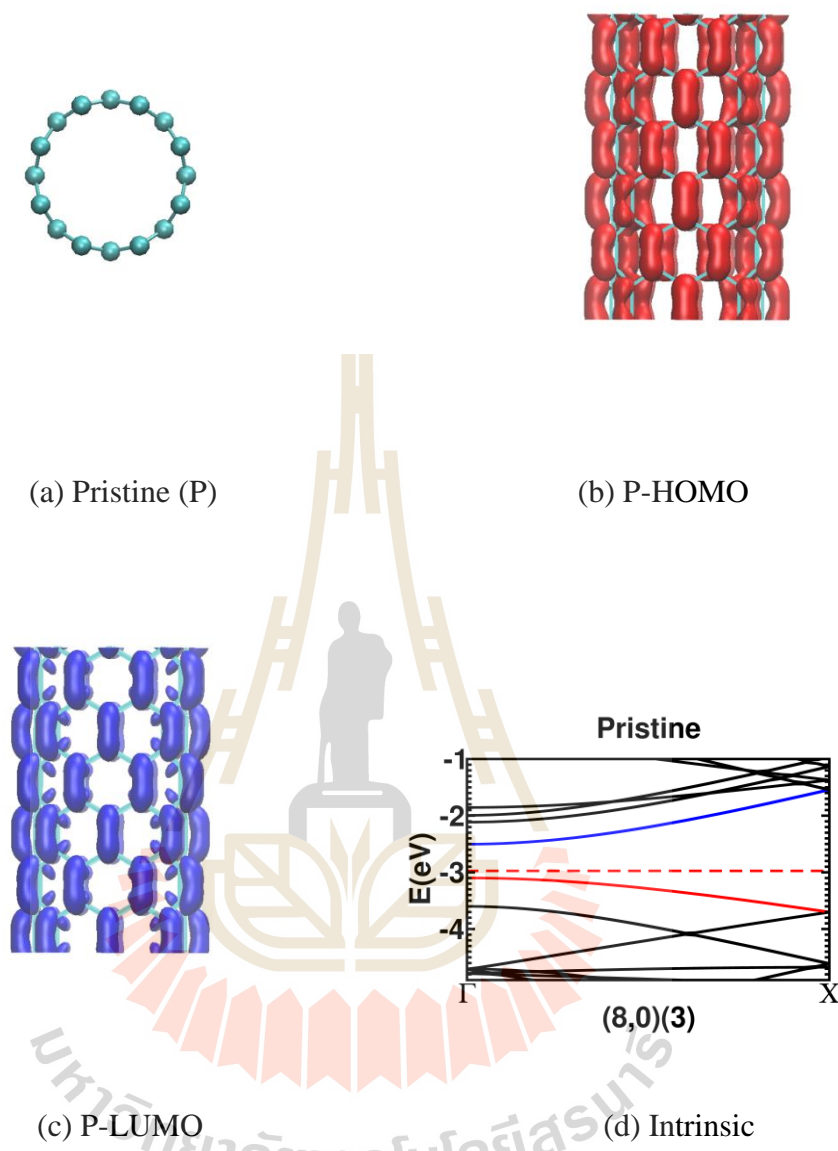


Figure 4.1 Pristine (8,0) SWCNT (a), (b) HOMO, (c) LUMO and (d) electronic band structure.

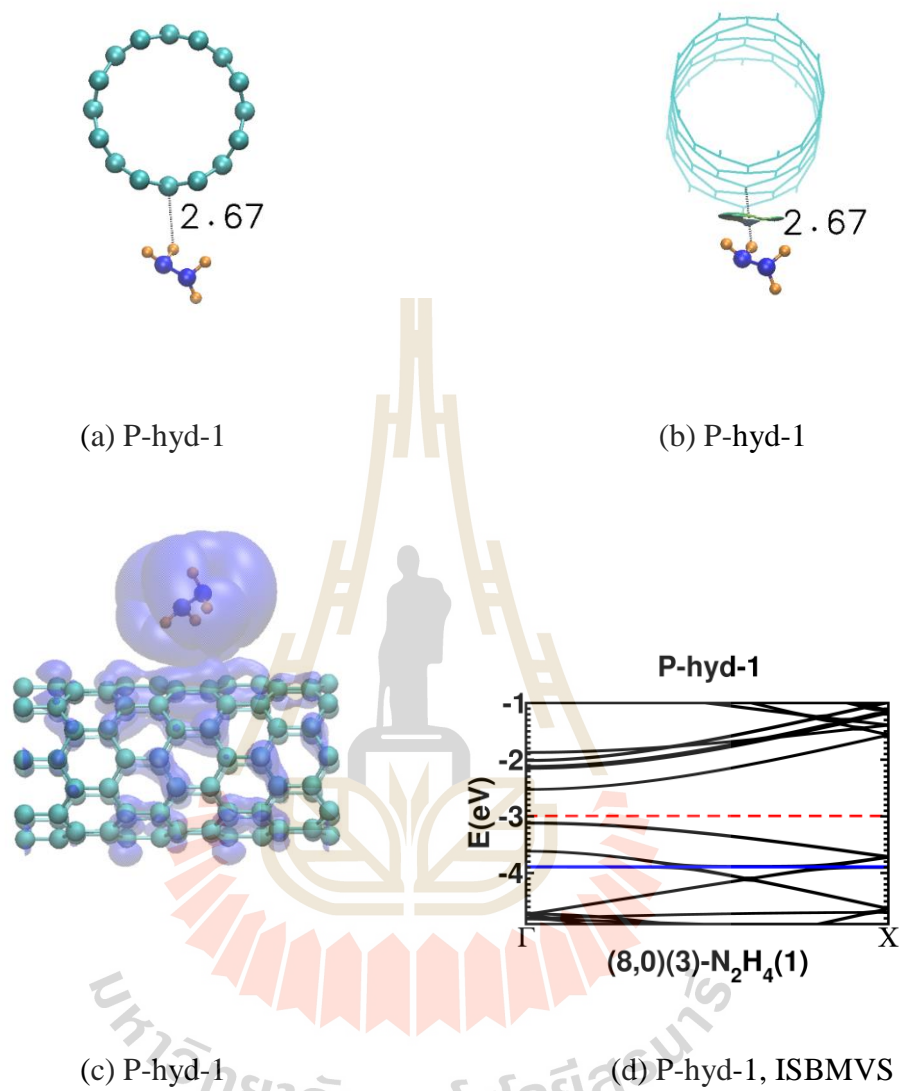


Figure 4.2 Doped SWCNT model P-hyd-1, (a) no common HB (N-H...N) interactions, (b) N-H... π interactions, (c) orbital shapes of electronic band structure state (d).

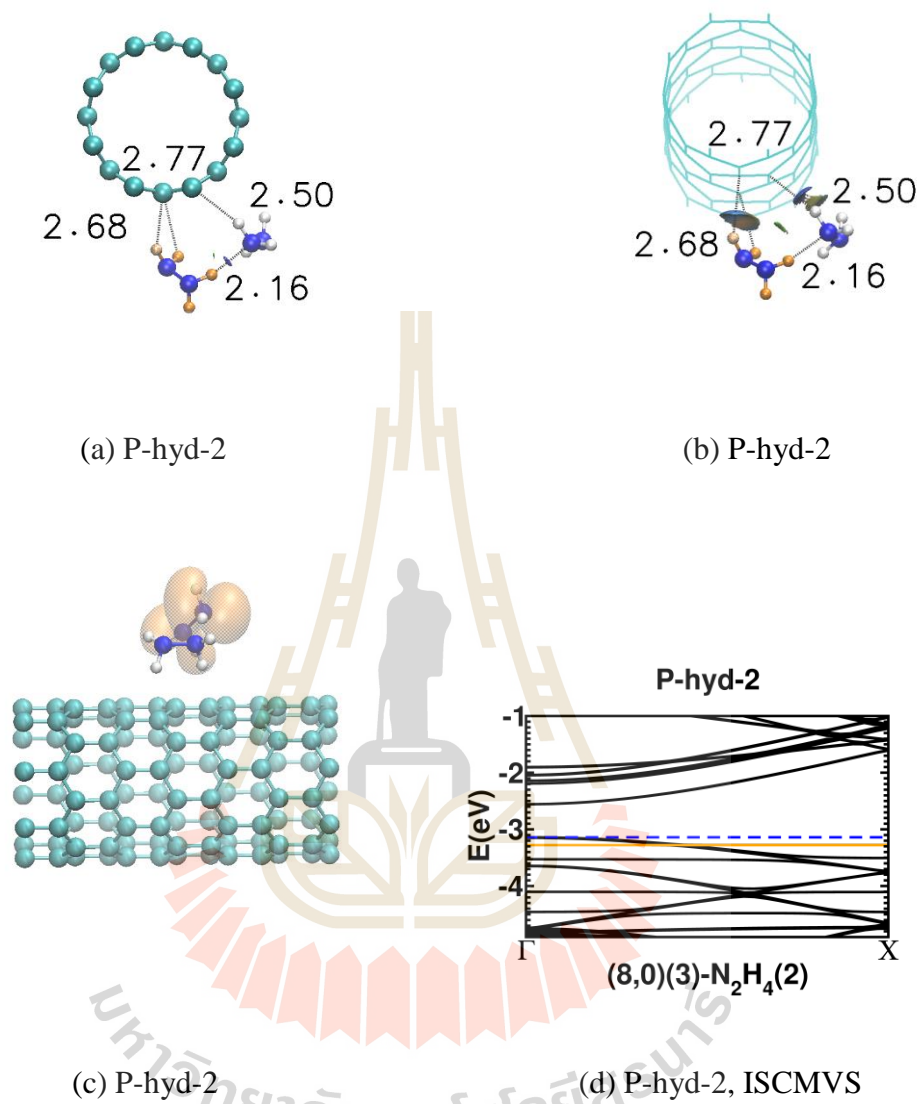


Figure 4.3 Doped SWCNT model P-hyd-2, (a) common HB (N-H...N) interactions, (b) N-H... π interactions, (c) orbital shapes of electronic band structure state (d).

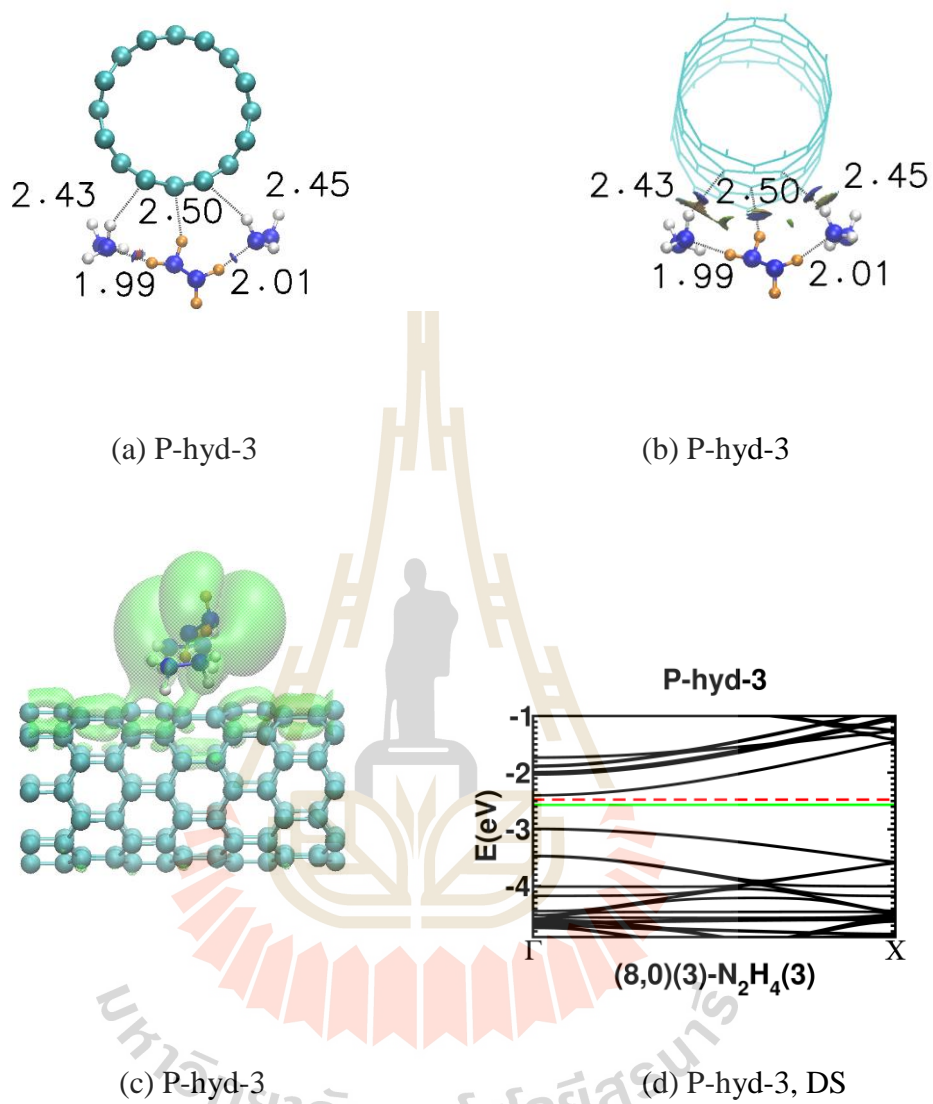


Figure 4.4 Doped SWCNT model P-hyd-3, (a) common HB (N-H...N) interactions, (b) N-H... π interactions, (c) orbital shapes of electronic band structure state (d).

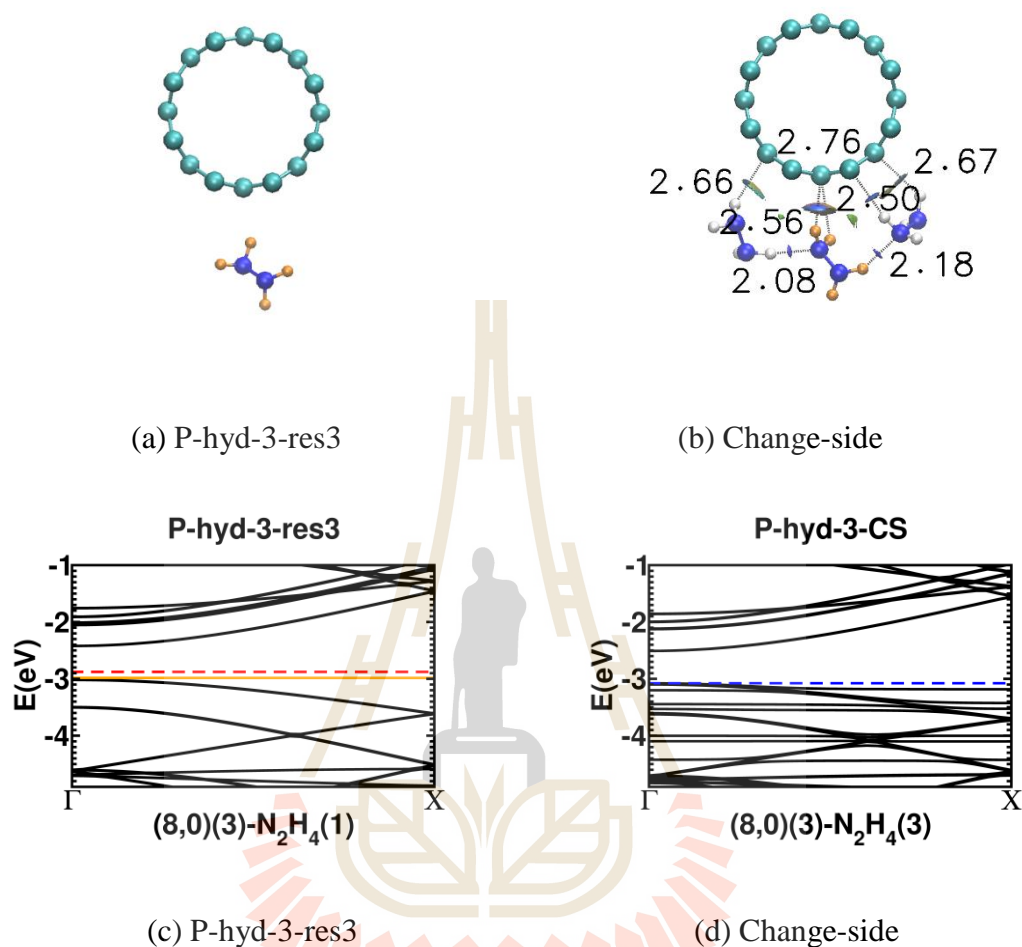


Figure 4.5 Supplement data (a) P-hyd-3 model remained only *res3*, (b) P-hyd-3-CS model H point to N of *res3*, (c) and (d) are electronic band of (a) and (b) respectively.

4.1.2 Electron charge transfer

The condition for electron charge transfers of hydrazine doped SWCNTs was analyzed by using the highest occupied molecular orbital (HOMO) and the lowest unoccupied molecular orbital (LUMO) of molecules, and the PDOS was used to analyze the molecular orbital in terms of the atomic orbital of each molecule. The

charge transfer mechanism was analyzed by using the HOMO energy of hydrazine molecules to dope the SWCNTs. With regard to the ISBMVS, the HOMO energy of molecules (green DOS) is lower than the HOMO energy of SWCNTs (blue dashed line), therefore no charge transfer (Table 4.3) is shown in Figure 4.9a (P-hyd-1). However, for ISCMVS, the HOMO energy of molecules is lower than the HOMO energy of SWCNTs, therefore no charge transfers from molecules to SWCNTs as shown in Figure 4.9b (P-hyd-2). With regard to DS, the HOMO energy of molecules is higher than the HOMO energy of SWCNTs, therefore, there is a charge transfer from the molecules (*res3*) to the SWCNTs (Leenaerts *et al.*, 2008) as shown in Figure 4.9c and 4.9d (P-hyd-3), and most of the HOMO is *p* orbital of *res3* molecule which cause the *res3* molecule to donate more electrons which shows a similar trend to the electron charge as shown in Table 4.3.

Table 4.1 Calculated electronic band structure state (EBSS) and band gap, of pristine SWCNT and hydrazine doped SWCNTs. Abbreviations: VBM = valence band maximum, CBM = conduction band minimum, DS = donor state.

Model	SWCNT (96 C atoms)	N ₂ H ₄	EBSS	Band gap (Γ, eV)
Pristine	1	0	Intrinsic ^a	0.596
P-hyd-1	1	1	ISBMVS ^a	0.587
P-hyd-2	1	2	ISCMVS ^a	0.582
P-hyd-3	1	3	DS ^b	0.422

^aBand gap = CBM - VBM

^bBand gap = DS - VBM

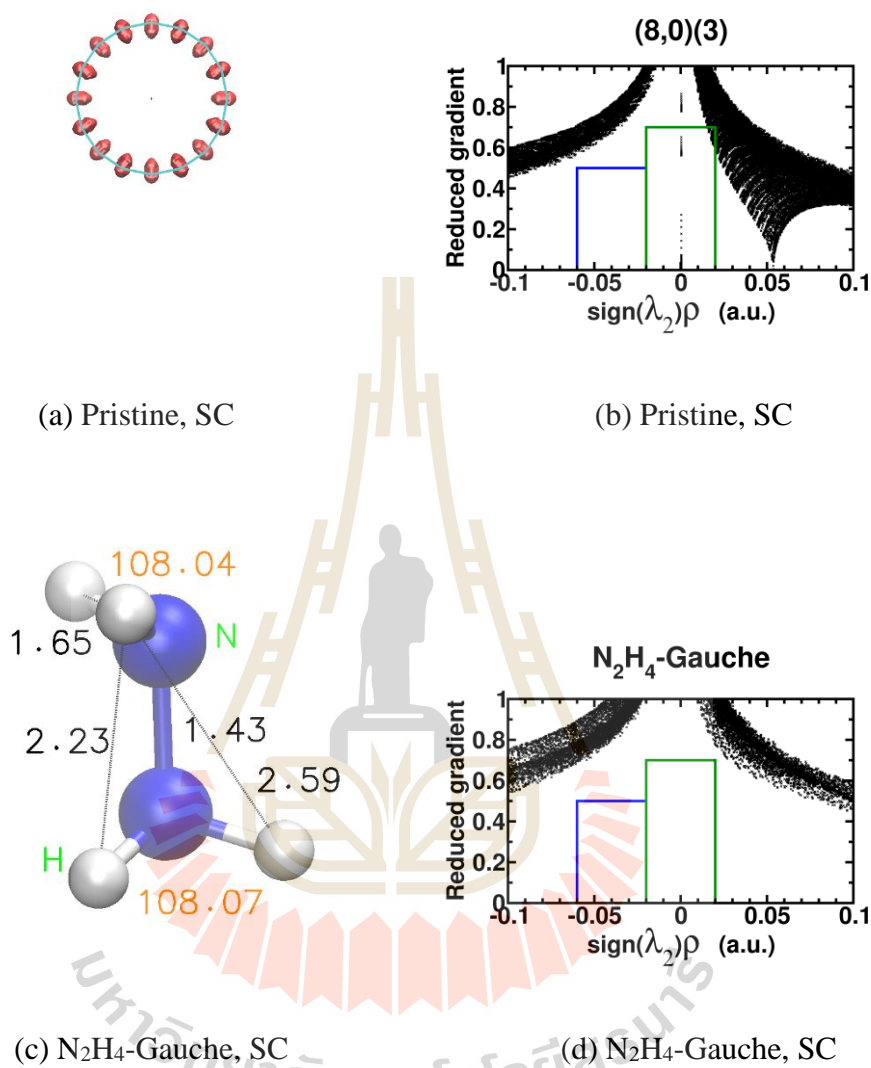


Figure 4.6 Noncovalent Interaction (NCI) plot (b) of pristine (8,0) SWCNT (a), and (d) of gauche N_2H_4 (c).

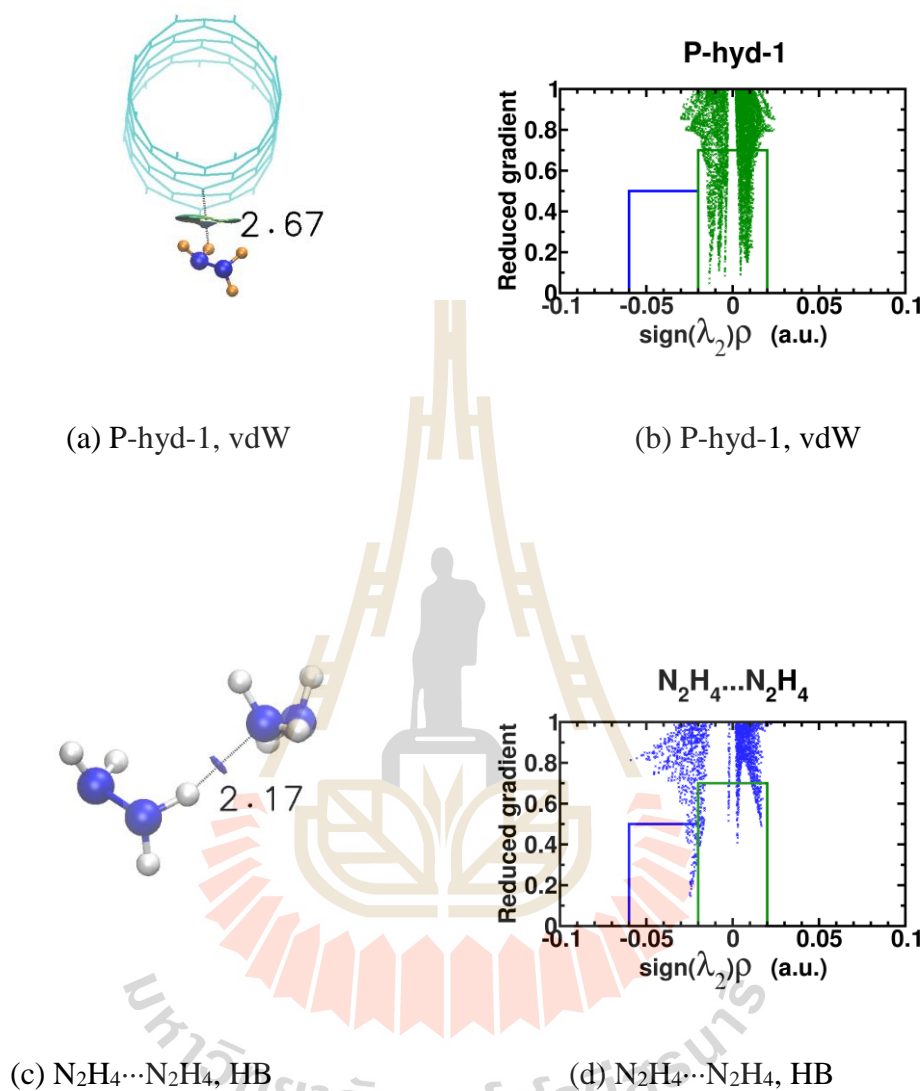


Figure 4.7 Noncovalent Interaction (NCI) plot (b) of N-H \cdots π (a) interaction, and (d) of N-H \cdots N (c) interaction.

The Figures 4.6 and 4.7, the color scale is $-2.00 < \rho < 2.00$ a.u. and isosurface is $s = 0.3$ a.u.. The blue region from -0.06 to -0.02 a.u. of $\text{sign}(\lambda_2)\rho$ is hydrogen bond

(HB) region. The green region is $-0.02 < \text{sign}(\lambda_2)\rho < 0.02$ is dispersion interaction (vdW) region, and $\text{sign}(\lambda_2)\rho > 0.02$ is steric clashes (SC) region.

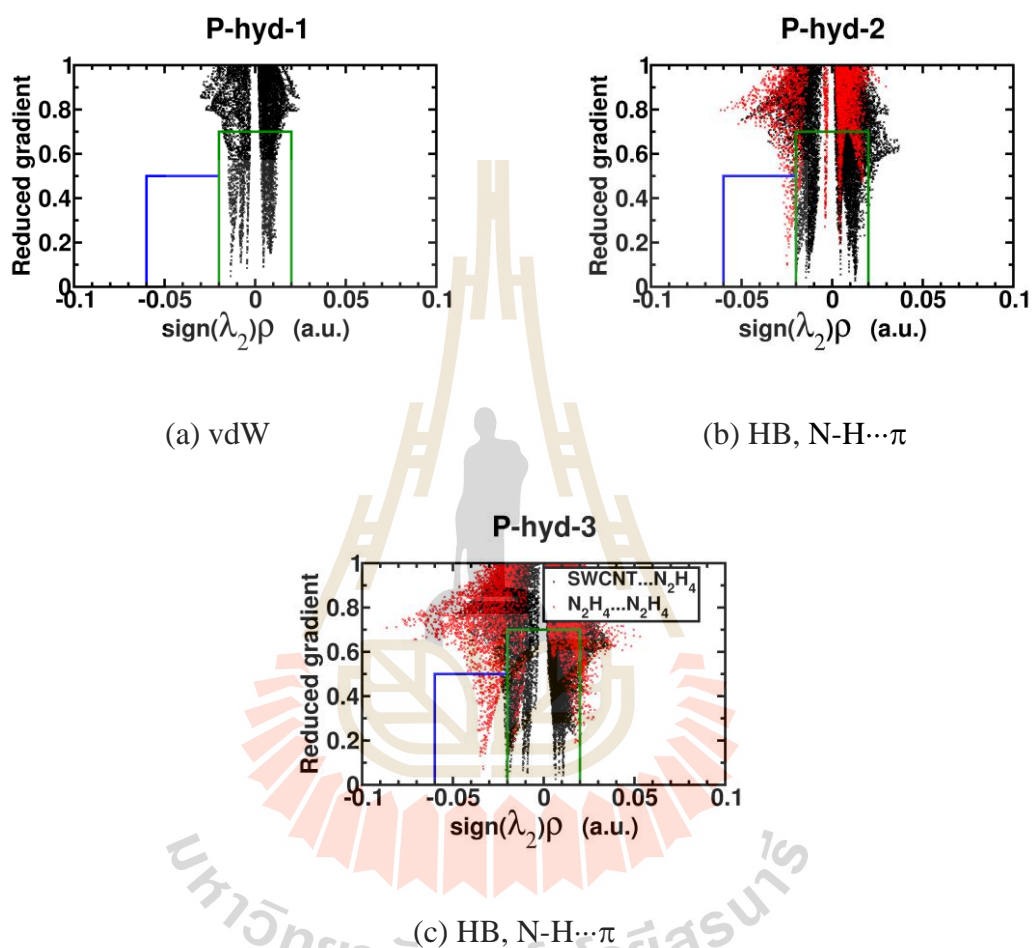


Figure 4.8 The intermolecular interaction, vdW interaction (a) of model P-hyd-1, the N-H...N (HB) (b) and N-H... π (c) interaction of model P-hyd-2 and P-hyd-3.

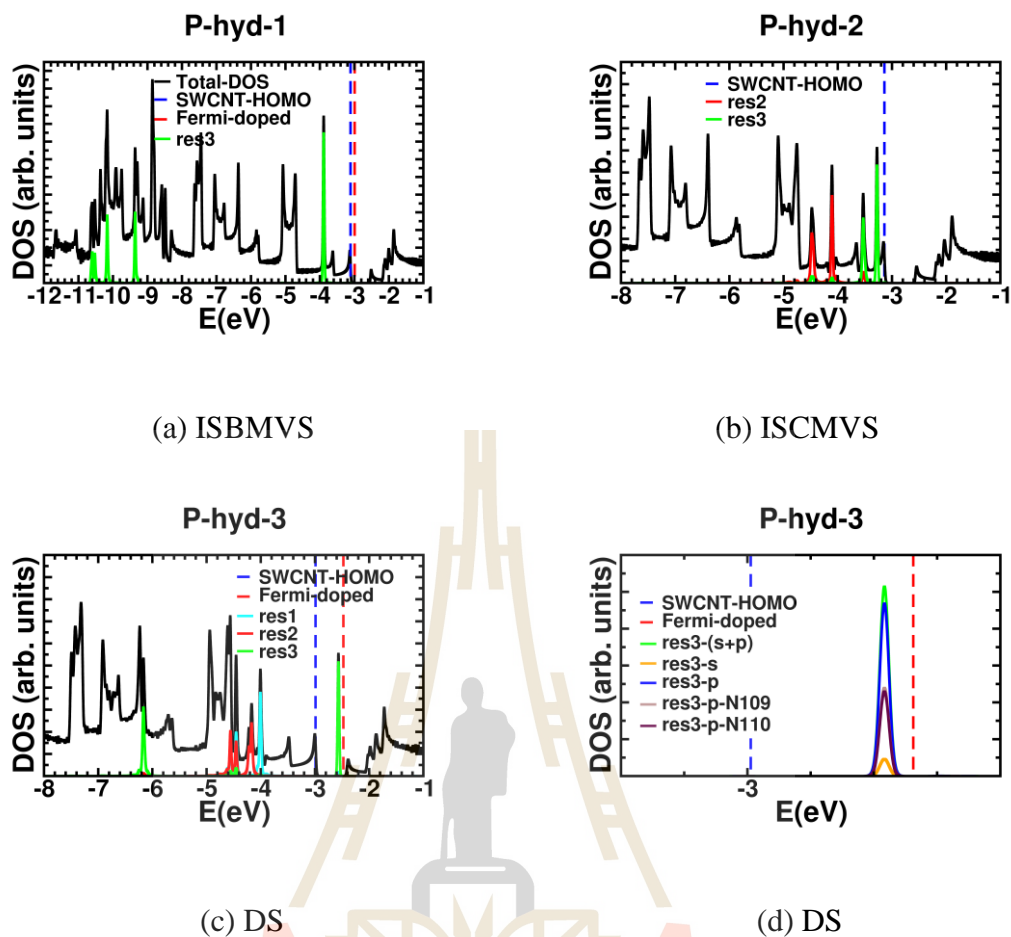


Figure 4.9 DOS (PDOS) of hydrazine molecules with doped SWCNTs (arb. units).

4.1.3 Configuration and Interaction Energy

The stability of hydrazine doped SWCNT as n-type semiconductor was considered by based on interaction energy. The gauche conformation is a most stable of a hydrazine molecule in the gas phase (Agusta *et al.*, 2010; Daff and de Leeuw, 2011; Tafreshi *et al.*, 2014). Our models most of hydrazine molecules in hydrazine doped SWCNT are gauche conformer. The interaction energy between hydrazine molecules and SWCNTs is polar $H\cdots\pi$ interaction, that comparable or even larger than common HB (Du *et al.*, 2013) shown in Table 4.2. The interaction energy between a hydrazine

molecule and SWCNT in P-hyd-1 model is vdW interaction (-0.1589 eV) it comparable to HB interaction in $N_2H_4 \cdots N_2H_4$ model (-0.1909 eV) in interaction strength, this model is a case of ISBMVS. The P-hyd-2 model, the molecules and SWCNT interactions are transforms from vdW interactions to $H \cdots \pi$ interactions, it consists of 1 $H \cdots N$, 1 $H \cdots \pi$ and 3 vdW interactions shown in Figure 4.3a and 4.3b respectively, the interactions strength ratio (ISR; $E_{ISR} = E_{H \cdots \pi}^{all} / E_{H \cdots N}^{all}$) is 1.6897, this model is a case of ISCMVS. In the case of DS, P-hyd-3 model it consists of 2 $H \cdots N$, 3 $H \cdots \pi$ and 2 vdW interactions shown in Figure 4.4a and 4.4b respectively, the ISR is 1.8693. The covering interaction of hydrazine molecules on the surface of SWCNT in model P-hyd-3 higher than P-hyd-2, in term of ISR.

For common polar HB ($N-H \cdots N$), N being attached to a H atom as an electron acceptor and N bearing lone electron pairs as an electron donor (Cheng *et al.*, 2003) shown in Figure 4.3a, the interaction is point-to-point interaction. The most stable $N-H \cdots \pi$ of R_2NH is T-shaped (Ottiger *et al.*, 2009; Ren *et al.*, 2009; Du *et al.*, 2013), the interaction could happen at any position of π -orbital (HOMO of pristine SWCNT is π -orbital parallel to SWCNT axis). Our models are $R-NH_2$, two polar H atoms could point to any position of π -orbital (Du *et al.*, 2013), and HOMO of hydrazine doped SWCNT could occur charge transfer from hydrazine molecules to SWCNT, most of charge from a hydrazine molecule which satisfied the condition of occur DS shown in Figure 4.4c and 4.9c.

Table 4.2 Calculated binding energy and interaction energy in eV for intermolecular interaction of hydrazine doped SWCNTs.

($E_{SWCNT}^{iso} = -14868.4259$; $E_{N_2H_4}^{iso} = -603.8406$; $E_{H_2O}^{iso} = -466.2458$); binding energy,

$E_{bin} = E_{SWCNT-N_2H_4} - E_{SWCNT}^{iso} - nE_{N_2H_4}^{iso}$, n is a number of hydrazine molecule;

interaction energy, $E_{int} = E_{SWCNT-N_2H_4} - E_{SWCNT}^{model} - E_{N_2H_4}^{res1} - E_{N_2H_4}^{res2} - E_{N_2H_4}^{res3}$;

$E_{ISR} = E_{H\cdots\pi}^{all}/E_{H\cdots N}^{all}$, $E_{H\cdots\pi}^{all} = E_{SWCNT-N_2H_4} - E_{SWCNT}^{model} - E_{N_2H_4}^{all}$, $E_{H\cdots N}^{all} = E_{N_2H_4}^{all} -$

$E_{N_2H_4}^{res1} - E_{N_2H_4}^{res2} - E_{N_2H_4}^{res3}$; Bond lengths in Å; P = pristine.

Model	E_{bin}	$E_{bin}/n_{N_2H_4}$	E_{int}	$E_{H\cdots\pi}^{all}$	$E_{H\cdots N}^{all}$	E_{ISR}
80-113,(P)	-	-	-	-	-	-
P-hyd-1	-0.1734	-0.1734	-0.1589	-0.1589	-	-
P-hyd-2	-0.5561	-0.2781	-0.5032	-0.3161	-0.1871	1.6897
P-hyd-3	-0.8473	-0.2824	-1.0486	-0.6832	-0.3655	1.8693
	E_{bin}	E_{bin}/n_{H-bond}	$E_{int}^{Ref.}$	E_{int}	Length	Length
^a N ₂ H ₄ ⋯N ₂ H ₄	-0.3561	-0.1781	-0.3757 ^b	-0.3664	2.1226	2.1250
H ₂ NH ₂ N⋯H ₂ O	-0.2312	-0.2313	-	-0.2469	2.1676	-
H ₂ O⋯H ₂ O	-0.2428	-0.2428	-0.2216 ^c	-0.2456	1.8742	-
N ₂ H ₄ ⋯N ₂ H ₄	-0.1838	-0.1838	Fig. 2d	-0.1909	2.1674	-

^a2 hydrogen bonds interaction of the N₂H₄⋯N₂H₄

^b(Ref. (Ju and Xiao, 2002)) DFT B3LYP/6-311G* (VI) calculation of the N₂H₄⋯N₂H₄

^c(Ref. (Xu and Goddard, 2004)) GGA PBEPBE calculation of the H₂O⋯H₂O

Table 4.3 Calculated Bader charge analysis of hydrazine and SWCNT in e^{-1} unit. Relative to hydrazine(SWCNT) = Bader(model) - Bader(N_2H_4 -isolated, pristine SWCNT); (N_2H_4 -isolated = 13.9993; P = 383.9975; $ResX(N_2H_4)$).

Model	<i>Res1</i>	<i>Res2</i>	<i>Res3</i>	Total- N_2H_4 - <i>Res3</i>	SWCNT
80-113,(P)	-	-	-	-	0.00(00)
P-hyd-1	-	-	0.00(22)	0.00(00)	-0.00(27)
P-hyd-2	-	-0.01(43)	0.02(94)	-0.01(43)	-0.00(94)
P-hyd-3	-0.03(23)	-0.03(22)	-0.19(77)	-0.06(45)	0.26(73)
P-hyd-3	<i>Res3</i>				
H	H	N	N	H	H
0.53(16)	0.58(98)	5.77(03)	5.76(74)	0.59(13)	0.55(12)

4.2 NMR chemical shifts (δ)

The calculated NMR δ was used to confirm the configuration of intermolecular interaction and that values can compare to experimental results. This study was described the intermolecular interaction of each electronic band structure state associated NMR δ values.

4.2.1 ^{13}C NMR chemical shifts (δ)

The ^{13}C NMR chemical shifts (δ) of pristine SWCNTs and hydrazine doped SWCNTs is $\delta_{SWCNT}^{TMS}(C) = \sigma_{TMS}(C) - \sigma_{SWCNT}(C)$, where TMS is tetramethylsilane ($\sigma_{TMS}(C) = 165.78$; Ref. (Pickard and Mauri, 2001) = 179.17 ppm) and σ is a shielding constant. The ^{13}C NMR δ experimental result of hydrazine doped SWCNTs found a shift to a higher frequency by 8 ppm (paramagnetic shift) and the broadening of the

main peak (Mistry *et al.*, 2011) as the SWCNTs change from an intrinsic to an n-type semiconductor.

The ^{13}C NMR δ peaks of doped SWCNTs have a width of ~ 10 ppm (117 to 127). The average shifts are slightly varied as shown in Figure 4.10. We selected δ of C atoms that are the closest to the H atom of the N-H $\cdots\pi$ interaction of each interaction (orange peak Figure 4.11a, 4.12a, 4.13a; orange C atoms Figure 4.11b, 4.12b, 4.13b). In the case of vdW interaction and ISBMVS (P-hyd-1), ^{13}C NMR δ shifts to the higher frequency as shown in Figure 4.10b and 4.11a. In the case of HB interaction and ISCMVS (P-hyd-2), ^{13}C NMR δ shifts to a lower frequency, but remained close to the position of ^{13}C NMR δ of pristine SWCNT as shown in Figure 4.10c and 4.12a. In the case of HB interaction and DS (P-hyd-3), ^{13}C NMR δ largely shifts to a lower frequency. The lowest ^{13}C NMR δ was shifted by 4 ppm when compared the pristine SWCNT as shown in Figure 4.10d and 4.13a.

Consider the ^{13}C NMR σ contribution part that shown in Table 4.4. The paramagnetic contribution (the distortion of the ground electronic state can be described by mixing excited electronic states into the original ground state), in the case of vdW interaction and ISBMVS (P-hyd-1), the σ shifts with the different ($\Delta = \sigma_P(C) - \sigma_{model}(C)$) 0.78 ppm. In the case of HB interaction and ISCMVS (P-hyd-2), the σ shifts with the Δ are -0.02, 0.62 and -0.36 ppm. In the case of HB interaction and DS (P-hyd-3), the σ shifts with the Δ are -1.51, -0.76 and 0.45 ppm. In the case of DS occurrence more mixing excited electronic states into the original ground state ($\Delta = -1.51$), Therefore, the ^{13}C NMR Δ largely shifts to a lower frequency.

4.2.2 ^1H NMR chemical shifts (δ)

The ^1H NMR δ ($\delta_{hyd}^{TMS}(H) = \sigma_{TMS}(H) - \sigma_{hyd}(H)$; $\sigma_{TMS}(H) = 29.90$; Ref. (Pickard and Mauri, 2001) = 30.76 ppm) is used to identify DS of hydrazine doped SWCNTs as shown in Figure 4.14. The DS takes place when the shift of ^1H NMR δ of hydrazine molecules is higher than 10 ppm. In the cases of ISBMVS and ISCMVS, there are no ^1H NMR δ shifts that are higher than 10 ppm. The H atom associated with each ^1H NMR δ peak is labeled in Figure 4.14b. The hydrazine molecules which cause the formation of DS give higher ^1H NMR δ . In addition, the H atoms associated with these peaks (H atom with label 111 and 114 in Figure 4.14b) are pointing toward the N atom of another molecule. This could be an important signature of the local structures that lead to the formation of DS of hydrazine doped SWCNTs.

Table 4.4 Calculated the σ (ppm) of C atoms that are closest to the H atom of the N-H $\cdots\pi$ interaction of each interaction.

Model	C#	Core	Bare	Dia	Para	P-occ-occ	P-LR-QR	Total
P	57	200.51	-44.70	2.34	-104.38	-1.97	-8.60	43.19
P-hyd-1	57	200.51	-45.94	2.34	-104.38	-1.97	-8.60	41.18
P-hyd-2	57	200.51	-45.03	2.34	-104.36	-1.99	-8.60	42.88
P	59	200.51	-44.67	2.34	-104.34	-1.98	-8.60	43.27
P-hyd-2	59	200.51	-46.22	2.34	-104.94	-1.97	-8.61	41.09
P	90	200.51	-44.70	2.34	-104.38	-1.97	-8.60	43.20
P-hyd-2	90	200.51	-44.57	2.34	-104.02	-1.98	-8.60	43.69
P	55	200.51	-44.67	2.34	-104.34	-1.98	-8.60	43.27
P-hyd-3	55	200.51	-42.66	2.35	-102.83	-1.96	-8.58	46.82
P-hyd-3	57	200.51	-43.52	2.35	-103.62	-1.96	-8.58	45.18
P-hyd-3	59	200.51	-45.26	2.34	-104.79	-1.96	-8.60	42.24

Core contribution (Core) + Bare contribution (Bare) + Diamagnetic contribution (Dia)

+ Paramagnetic contribution (Para) + Paramagnetic US occ-occ (P-occ-occ) +

Paramagnetic US L-R Q-R (P-LR-QR) = Total (Total).

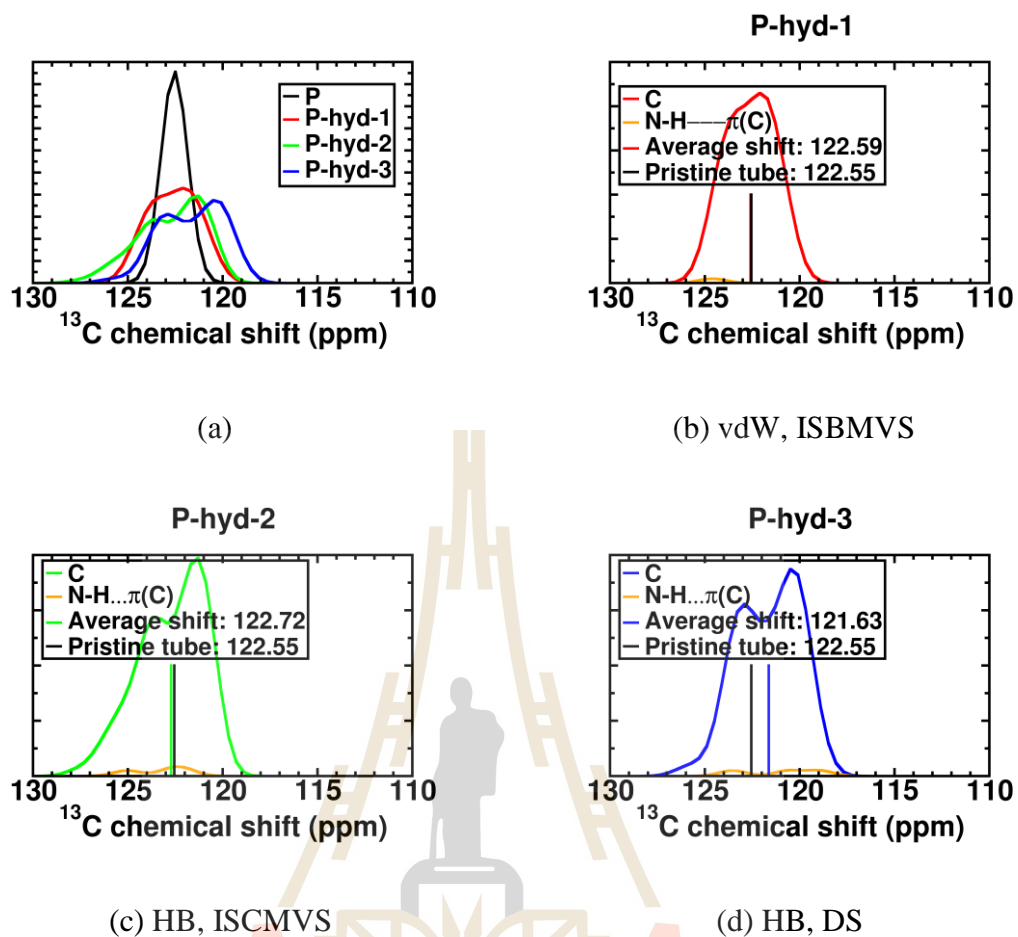


Figure 4.10 ^{13}C NMR δ of hydrazine doped SWCNTs of each interaction and electronic band structure, frequency (arb. units).

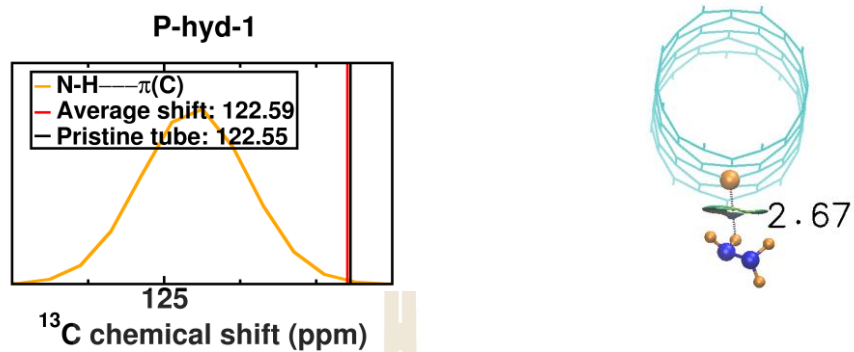


Figure 4.11 Selected ^{13}C NMR δ (a) and selected C atom (b) of vdW interaction of hydrazine doped SWCNT, frequency (arb. units), P-hyd-1.

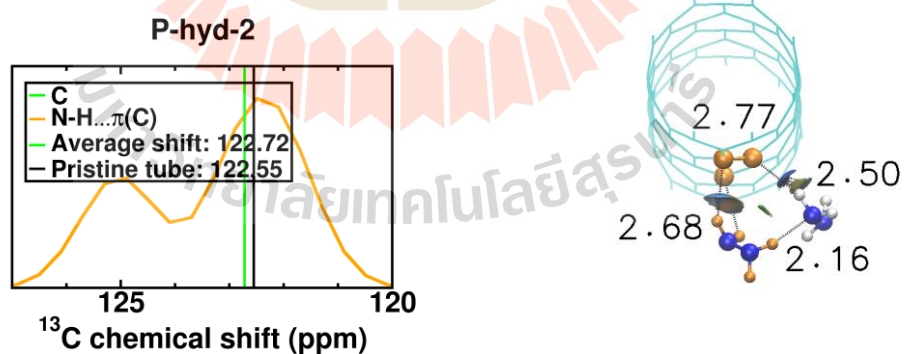


Figure 4.12 Selected ^{13}C NMR δ (a) and selected C atoms (b) of HB interaction of hydrazine doped SWCNT, frequency (arb. units), P-hyd-2.

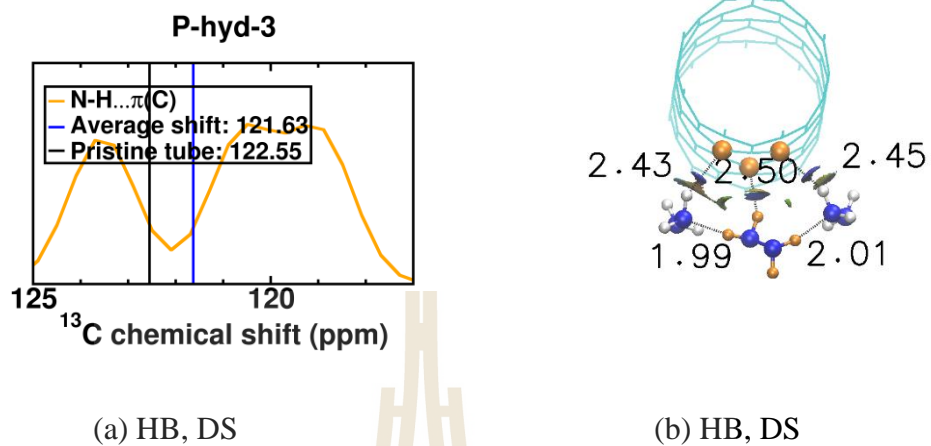


Figure 4.13 Selected ^{13}C NMR δ (a) and selected C atoms (b) of HB interaction of hydrazine doped SWCNT, frequency (arb. units), P-hyd-3.

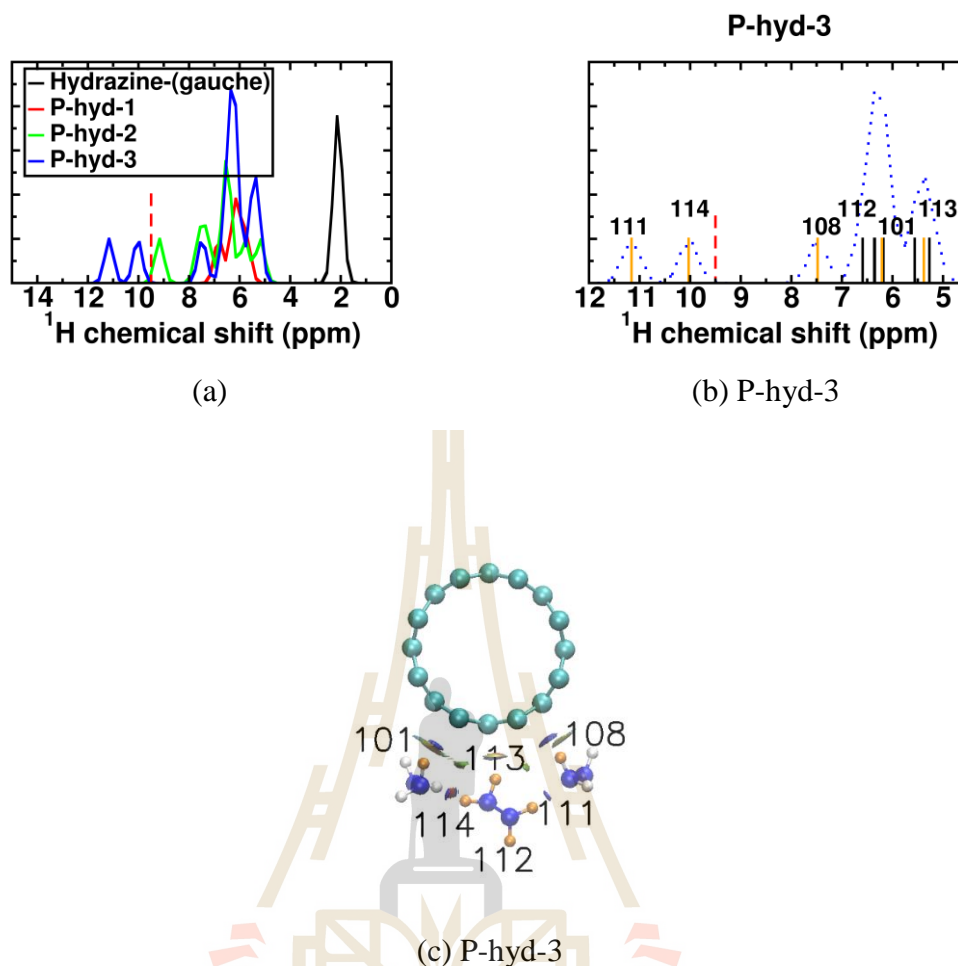


Figure 4.14 ^1H NMR δ of hydrazine doped SWCNTs, frequency (arb. units).

4.3 Ultraviolet-visibility (UV-Vis) spectroscopic

The calculated photon absorption energy (PAE) and optical transitions of each electronic band structure state will be described, the degenerate band split into nondegenerate band from the induced of hydrazine doped SWCNT, and in the case of DS occurrence the dark exciton has changed to bright exciton will be described.

4.3.1 Photon absorption energy of IS and DS

The UV-Vis experimental results of hydrazine doped SWCNTs do not seem to change their PAE as the samples change from intrinsic semiconductors to n-type semiconductors. However, there is a decrease in photon absorption intensity when compares to pristine SWCNTs (Mistry *et al.*, 2011).

The PAE was considered on the basis of band-to-band transitions (Bassani and Parravicini, 1989) and selection rules (Griffiths, 2005; Rohlfing and Louie, 2000; Hiroshi, 2012) of single-electron eigen states. The calculated optical transition (Davidson-like algorithm (Ge *et al.*, 2014)) of pristine SWCNTs shows the E_{11} exciton composed of band-to-band transitions between the HOMO (H-0) band and the LUMO+3 (L+3) band, both bands are double degenerate, there are four singlet excitons formed between them, a dipole-allowed E_{11} state and three dark states: two degenerate states and one single state, which is the same as the transition (Mu *et al.*, 2013) studied by Mu *et al.* (2013), the orbital shapes of the initial and final states related to the transitions are shown in Figure 4.16. Our calculated PAE of E_{11} is 1.278 eV (shown in Figure 4.15 and Table 4.5) which is in a good agreement with Ref. (Spataru *et al.*, 2004) (1.39 eV). For IS, ISBMVS (P-hyd-1) our calculated PAE shows a slight change to higher energy of only 0.001 eV compared to the pristine SWCNTs. This is consistent with Ref. (Saidi and Norman, 2014) (SW, DV), Ref. (Konabe and Watanabe, 2011) (IS) and Ref. (Mu *et al.*, 2013) ((8,0)+O). For ISCMVS (P-hyd-2) our calculated PAE shows a slight change to lower energy of only -0.005 eV compared to the pristine SWCNTs, which consistent with Ref. (Mu *et al.*, 2013) ((8,0)+O; chemisorption). The change of our calculated PAE associated with the split of degenerate band split into nondegenerate

band which induced from hydrazine molecules (physisorption). For DS, the PAE changes slightly, i.e., for P-hyd-3 the PAE changes to higher energy by only 0.013 eV in comparison to pristine SWCNTs, to our knowledge, there is no computational values reported for DS occurrence in (8,0) SWCNT.

The PAE of E_{22} are shows in Table 4.6, our calculated for pristine SWCNT is 1.647 eV good agreement with calculation of Ref. (Saidi and Norman, 2014) (1.51) and Ref. (Mu *et al.*, 2013) (1.79), for doped SWCNTs in the case of IS (ISBMVS, ISCMVS) the PAE slight changes to lower energy (-0.003, -0.005 eV). The case of DS occurrence the PAE a large change to lower energy with value 0.021 eV.

4.3.2 Optical transition of IS and DS

The PAE is associated with the optical transition. The optical transitions of E_{11} are shows in Table 4.7. We listed the calculated Eigen energies near the band edge are shows in Table 4.8. For the pristine SWCNT, we listed the occupied levels and unoccupied levels as H (HOMO, highest occupied molecular orbital) and L (LUMO, lowest unoccupied molecular orbital) with increasing index number as the level is moved away from the band edge. In addition, we also put the label (-) and (+) for levels with non-degeneracies in doped SWCNTs. When hydrazine caused the degenerate band of SWCNTs to split into nondegenerate bands ((-),(+)), the optical transitions also changed. For the ISCMVS (P-hyd-2), bright excitons of E_{11} (dipole-allowed) are the optical transitions from H-0(+) \rightarrow L+3(-) and H-0(-) \rightarrow L+3(+), and dark excitons (dipole-forbidden) are the optical transitions from H-0(+) \rightarrow L+3(+) and H-0(-) \rightarrow L+3(-), the bright and dark excitons in this case are same transitions as O doped (8,0) SWCNT (chemisorption) was reported by Ref. (Mu *et al.*, 2013), the bright exciton has

slightly change in PAE compared to pristine SWCNT (-5 meV). For the ISBMVS (P-hyd-1) and DS (P-hyd-3), bright excitons of E_{11} are the optical transitions from H-0(+) \rightarrow L+3(-) and H-0(-) \rightarrow L+3(+), and dark excitons changed to bright excitons are the optical transitions from H-0(+) \rightarrow L+3(+) and H-0(-) \rightarrow L+3(-), the orbital shapes of the initial and final states related to the transitions are shown in Figure 4.18, 4.19, 4.20 and 4.21, the bright excitons has slightly change to higher energy in PAE compared to pristine SWCNT (1 and 13 meV respectively). The components of dipole polarizability (α_{ij}) shown in Figure 4.15, the main component is from α_{zz} , which tube axis is along the z direction.

The optical transitions of E_{22} are shows in Table 4.6, the bright excitons of pristine SWCNT are the transitions (principle components) from H-1(A) \rightarrow L+2(B) and H-1(B) \rightarrow L+2(A), the orbital shapes of the initial and final state related to the transition are shown in Figure 4.17. The hydrazine caused the degenerate band of SWCNTs to split into nondegenerate bands, the optical transitions also changed, for all doped SWCNT the bright excitons transitions are from H-1(+) \rightarrow L+2(-) and H-1(-) \rightarrow L+2(+).

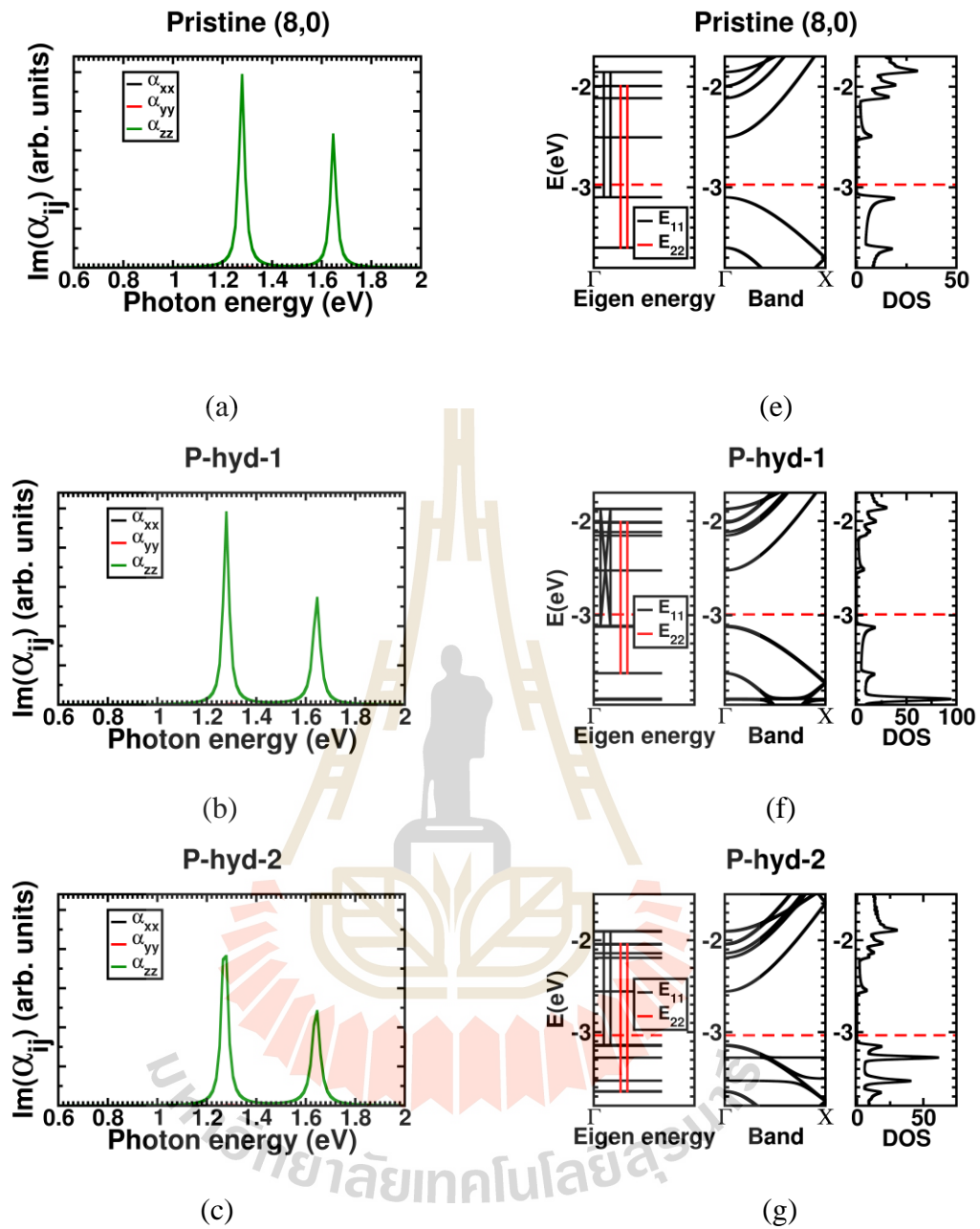


Figure 4.15 Calculated photon absorption energy of (a) pristine (8,0) SWCNT, (b)-(d) doped SWCNT. The corresponding optical transition states, band structures, and density of states are shown on the right (e)-(h). The z axis is defined along the tube direction.

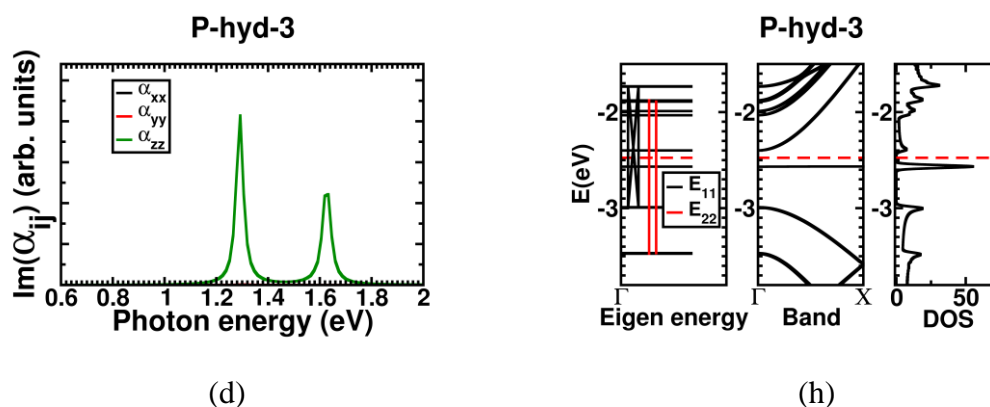


Figure 4.15 Calculated photon absorption energy of (a) pristine (8,0) SWCNT, (b)-(d) doped SWCNT. The corresponding optical transition states, band structures, and density of states are shown on the right (e)-(h). The z axis is defined along the tube direction (Continued).



(a) HOMO; (A, B; π)

(b) LUMO+3; (A, B; π, π^*)

Figure 4.16 Relevant molecular orbitals for E_{11} (A_{11} , B_{11}) optical transition of the pristine (8,0) SWCNT; (c), (e) the dipole-allowed transition and (d), (f) the dipole forbidden.

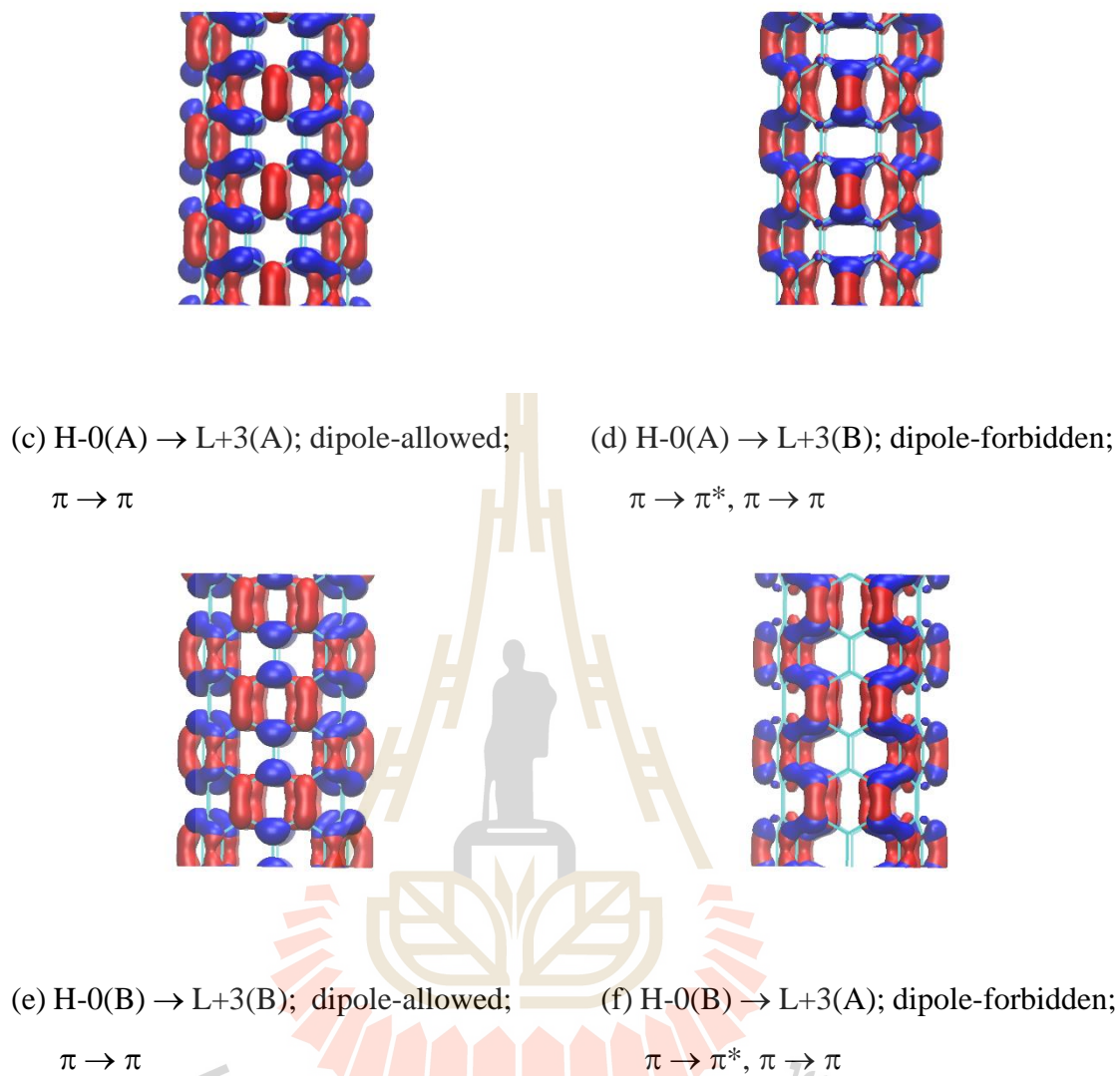


Figure 4.16 Relevant molecular orbitals for E_{11} (A_{11} , B_{11}) optical transition of the pristine (8,0) SWCNT; (c), (e) the dipole-allowed transition and (d), (f) the dipole forbidden (Continued).

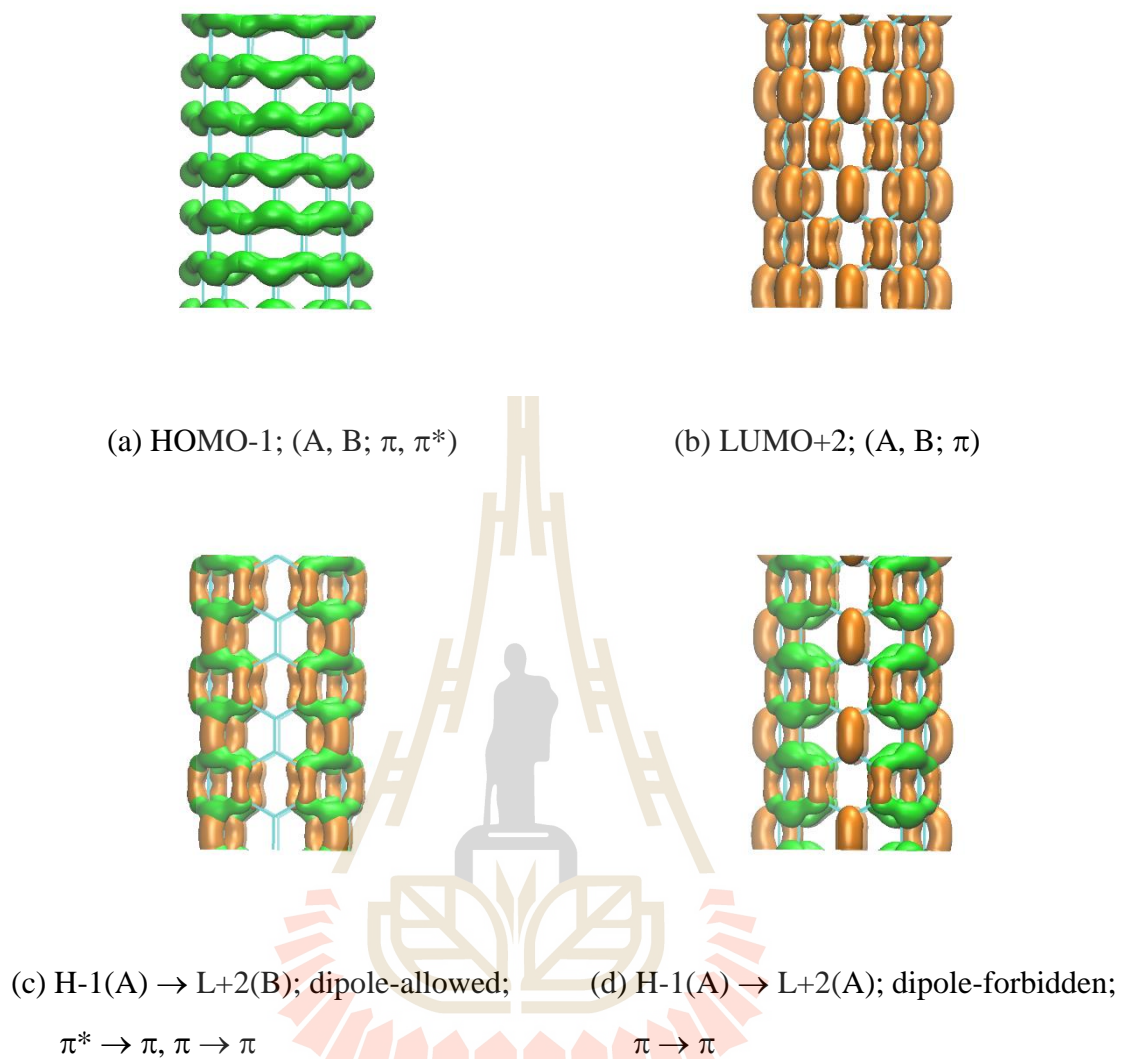


Figure 4.17 Relevant molecular orbitals for E_{22} (A_{22} , B_{22}) optical transition of the pristine (8,0) SWCNT; (c), (e) the dipole-allowed transition and (d), (f) the dipole forbidden.



(e) $H-1(B) \rightarrow L+2(A)$; dipole-allowed;

$\pi^* \rightarrow \pi, \pi \rightarrow \pi$

(f) $H-1(B) \rightarrow L+2(B)$; dipole-forbidden;

$\pi \rightarrow \pi$

Figure 4.17 Relevant molecular orbitals for E_{22} (A_{22} , B_{22}) optical transition of the pristine (8,0) SWCNT; (c), (e) the dipole-allowed transition and (d), (f) the dipole forbidden (Continued).

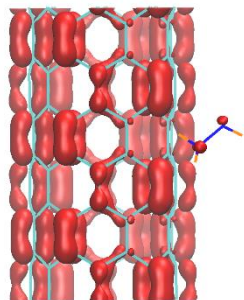
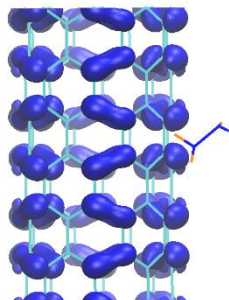
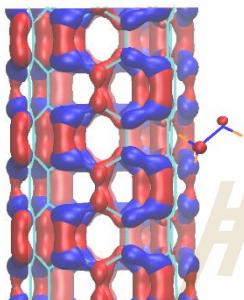
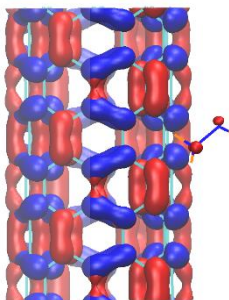
(a) HOMO-0(+); (π)(b) LUMO+3(+); (π, π^*)(c) H-0(+) \rightarrow L+3(-); dipole-allowed; $\pi \rightarrow \pi^*, \pi \rightarrow \pi$ (d) H-0(+) \rightarrow L+3(+); dipole-allowed; $\pi \rightarrow \pi$

Figure 4.18 Relevant molecular orbitals for E_{11} (A_{11}) optical transition of the doped (8,0) SWCNT P-hyd-1 model; (c) and (d) the dipole-allowed transition.

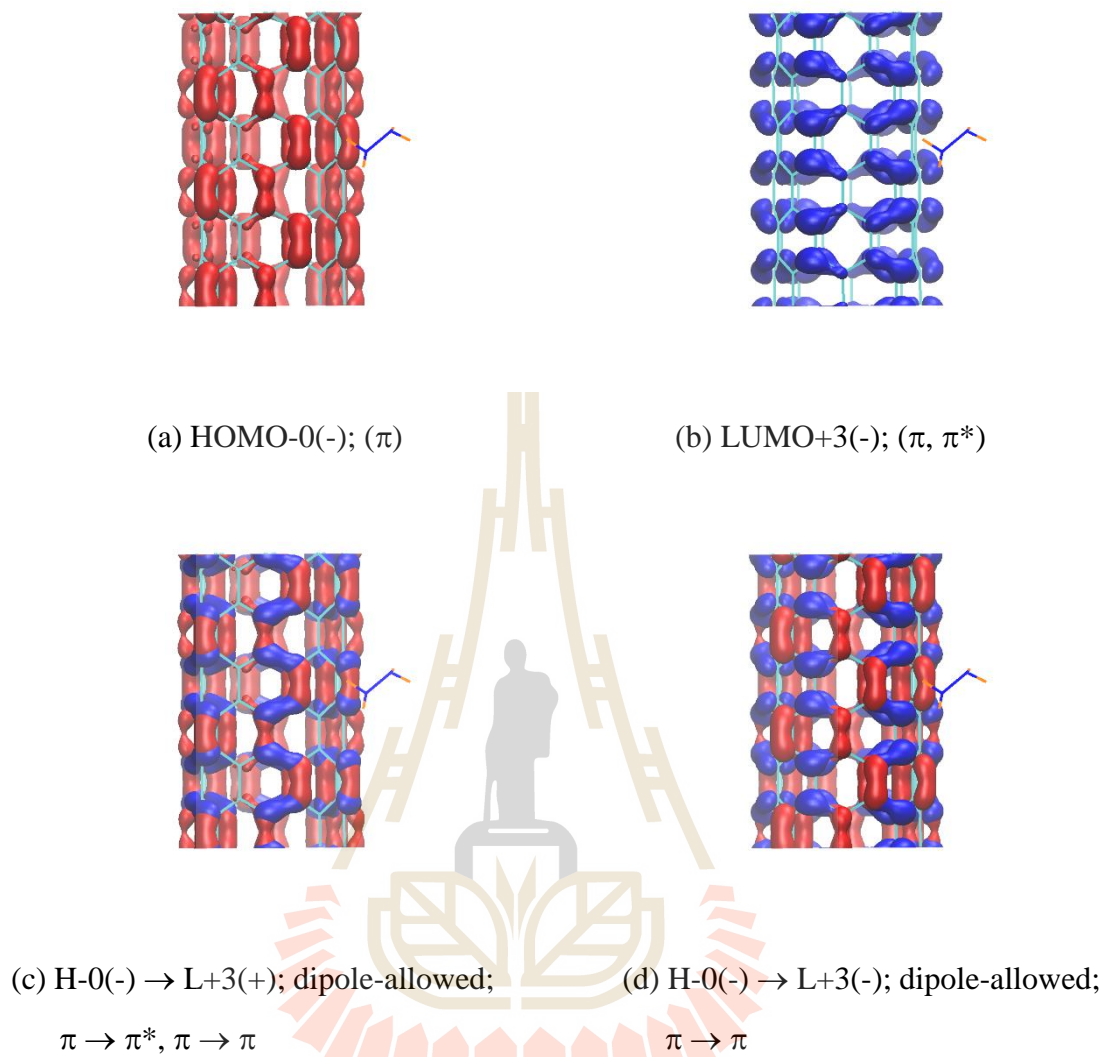


Figure 4.19 Relevant molecular orbitals for E_{11} (B_{11}) optical transition of the doped (8,0) SWCNT P-hyd-1 model; (c) and (d) the dipole-allowed transition.

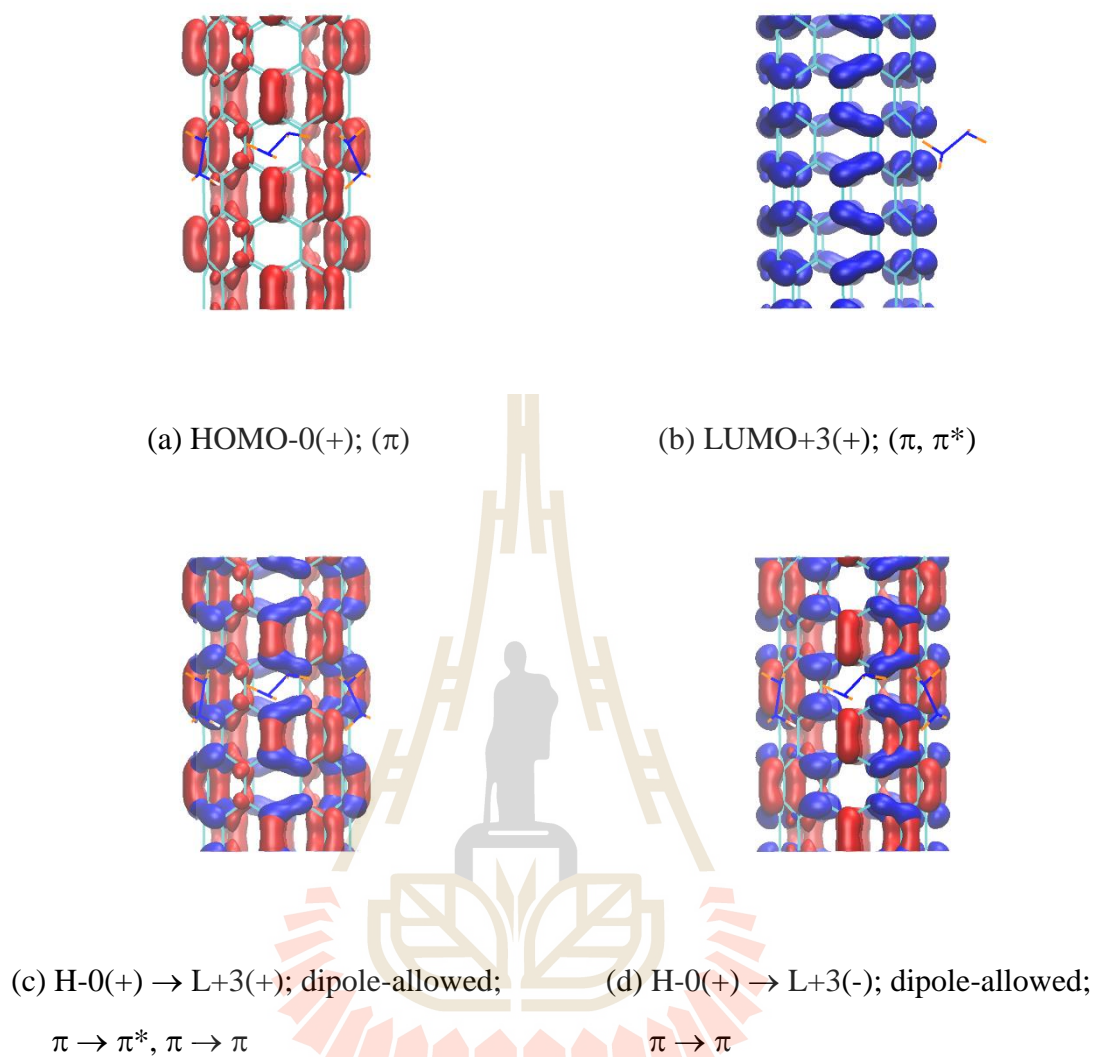


Figure 4.20 Relevant molecular orbitals for E_{11} (A_{11}) optical transition of the doped (8,0) SWCNT P-hyd-3 model; (c) and (d) the dipole-allowed transition.

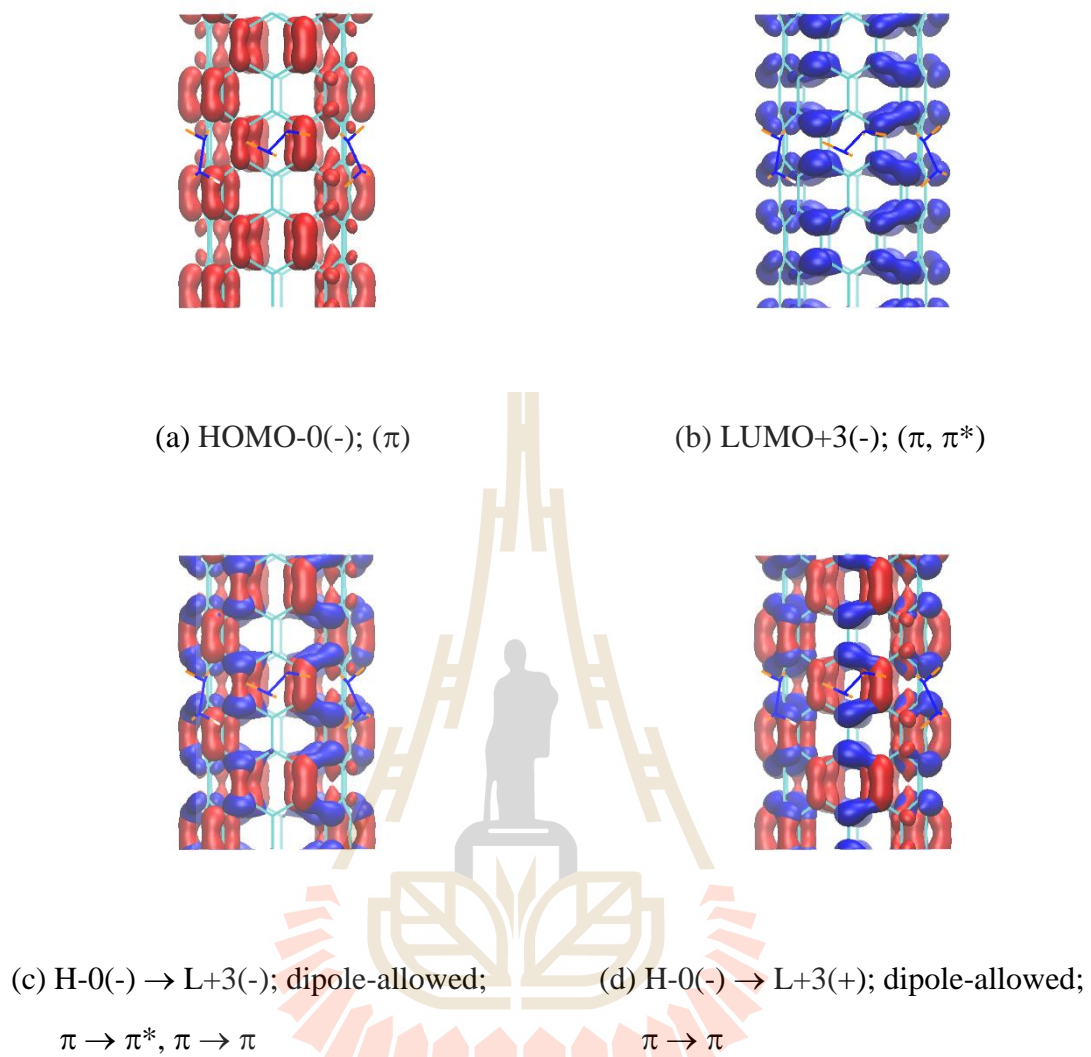


Figure 4.21 Relevant molecular orbitals for E_{11} (B_{11}) optical transition of the doped (8,0) SWCNT P-hyd-3 model; (c) and (d) the dipole-allowed transition.

Table 4.5 E_{11} Photon absorption energy (PAE) in eV of pristine and doped SWCNTs.

Abbreviations: P = pristine, SW = Stone-Wales, DV = diatom vacancies, SV = single vacancy, IS = impurity state, DS = donor state, ISBMVS = impurity state below the maximum valence state, ISCMVS = impurity state close to the maximum valence state, Shift = (PAE-doped) - (PAE-pristine).

Source	System	Model (E_{11})			Initial state	Final state
		PAE pristine	PAE doped	Shift		
Exp. ^a	P (8,0)	1.598	-	-	-	-
LDA ^b	P (8,0)	1.39	-	-	-	-
PBE ^c	SW (7,0)	0.89	0.88	-0.01	-	-
	DV 97,0)	0.89	0.81	-0.08	-	-
TB-BSE ^d	IS (20,0)	0.637	0.623	-0.014	-	-
GW+BSE ^e	P (8,0)	1.53	-	-	H-0	L+3
	O (8,0)	1.53	1.45	-0.08	H-0(+)	L+3(-)
	O (8,0)	1.53	1.62	0.09	H-0(-)	L+3(+)
	2H (8,0)	1.53	1.27	-0.26	State ₁	State ₂
	SV (8,0)	1.53	0.97	-0.56	-	-
	SW (8,0)	1.53	1.35	-0.18	-	-
Present						
P (8,0)	Intrinsic	1.278	-	-	H-0(A)	L+3(A)
P (8,0)	Intrinsic	1.278	-	-	H-0(B)	L+3(B)
P-hyd-1	ISBMVS	1.278	1.279	0.001	H-0(+)	L+3(+);L+3(-)
P-hyd-1	ISBMVS	1.278	1.279	0.001	H-0(-)	L+3(+);L+3(-)
P-hyd-2	ISCMVS	1.278	1.273	-0.005	H-0(+)	L+3(-)
P-hyd-2	ISCMVS	1.278	1.273	-0.005	H-0(-)	L+3(+)
P-hyd-3	DS	1.278	1.291	0.013	H-0(+)	L+3(+);L+3(-)
P-hyd-3	DS	1.278	1.291	0.013	H-0(-)	L+3(+);L+3(-)

^a Ref. (Weisman and Bachilo, 2003); Experimental measurement of the pristine (8,0)

SWCNT; ^b Ref. (Spataru *et al.*, 2004); LDA calculations of the pristine (8,0) SWCNT

^c Ref. (Saidi and Norman, 2014); PBE calculations of 3 units supercell of the (7,0)

SWCNT; ^d Ref. (Konabe and Watanabe, 2011); Tight-binding+BSE calculations of the

(20,0) SWCNT; ^e Ref. (Mu *et al.*, 2013); GW+BSE, PBE calculations of the pristine

(8,0) SWCNT

Table 4.6 E_{22} Photon absorption energy (PAE) in eV of pristine and doped SWCNTs. Abbreviations: P = pristine, SW = Stone-Wales, DV = diatom vacancies, SV = single vacancy, IS = impurity state, DS = donor state, ISBMVS = impurity state below the maximum valence state, ISCMVS = impurity state close to the maximum valence state, Shift = (PAE-doped) - (PAE-pristine).

		Model (E_{22})			Initial	Final
Source	System	PEA pristine	PAE doped	Shift	state	state
Exp. ^a	P (8,0)	1.878	-	-	-	-
LDA ^b	P (8,0)	1.51	-	-	-	-
PBE ^c	SW (7,0)	2.19	2.40	0.21	-	-
	DV (7,0)	2.19	2.29	0.10	-	-
GW+BSE ^e	P (8,0)	1.79	-	-	H-1	L+2
Present						
P (8,0)	Intrinsic	1.647	-	-	H-1(A)	L+2(B)
P (8,0)	Intrinsic	1.647	-	-	H-1(B)	L+2(A)
P-hyd-1	ISBMVS	1.647	1.644	-0.003	H-1(+)	L+2(-)
P-hyd-1	ISBMVS	1.647	1.644	-0.003	H-1(-)	L+2(+)
P-hyd-2	ISCMVS	1.647	1.642	-0.005	H-1(+)	L+2(-)
P-hyd-2	ISCMVS	1.647	1.642	-0.005	H-1(-)	L+2(+)
P-hyd-3	DS	1.647	1.626	-0.021	H-1(+)	L+2(-)
P-hyd-3	DS	1.647	1.626	-0.021	H-1(-)	L+2(+)

^a Ref. (Weisman and Bachilo, 2003); Experimental measurement of the pristine (8,0)

SWCNT

^b Ref. (Spataru *et al.*, 2004); LDA calculations of the pristine (8,0) SWCNT

^c Ref. (Saidi and Norman, 2014); PBE calculations of 3 units supercell of (7,0)

SWCNT

^e Ref. (Mu *et al.*, 2013); GW+BSE, PBE calculations of the pristine (8,0) SWCNT

Table 4.7 Electric dipole allowed (di-al) and forbidden (di-fo) optical transitions of pristine and doped (8,0) SWCNTs. Abbreviations: P = pristine, DS = donor state, ISBMVS = impurity state below the maximum valence state, ISCMVS = impurity state close to the maximum valence state.

Model	System	E_{11} , di-al	E_{11} , di-fo
P (8,0)	Intrinsic	H-0(A) \rightarrow L+3(A)	H-0(A) \rightarrow L+3(B)
P (8,0)	Intrinsic	H-0(B) \rightarrow L+3(B)	H-0(B) \rightarrow L+3(A)
P-hyd-1	ISBMVS	H-0(+) \rightarrow L+3(+)	-
P-hyd-1	ISBMVS	H-0(+) \rightarrow L+3(-)	-
P-hyd-1	ISBMVS	H-0(-) \rightarrow L+3(+)	-
P-hyd-1	ISBMVS	H-0(-) \rightarrow L+3(-)	-
P-hyd-2	ISCMVS	H-0(+) \rightarrow L+3(-)	H-0(+) \rightarrow L+3(+)
P-hyd-2	ISCMVS	H-0(-) \rightarrow L+3(+)	H-0(-) \rightarrow L+3(-)
P-hyd-3	DS	H-0(+) \rightarrow L+3(+)	-
P-hyd-3	DS	H-0(+) \rightarrow L+3(-)	-
P-hyd-3	DS	H-0(-) \rightarrow L+3(+)	-
P-hyd-3	DS	H-0(-) \rightarrow L+3(-)	-

Table 4.8 Calculated Eigen energies in eV at the Γ -point of the pristine (8,0) SWCNT and doped (8,0) SWCNTs, model, P-hyd-1, P-hyd-2 and P-hyd-3. To aid identification of the energy levels, the labels are shown. The Fermi energy (E_f) of each system is also shown. Label abbreviations: L = lowest unoccupied molecular orbital, H = highest occupied molecular orbital.

Energy (eV)							
P	Label	P-hyd-1	Label	P-hyd-2	Label	P-hyd-3	Label
-1.8549	L+3(A)	-1.8694	L+3(+)	-1.8999	L+3(+)	-1.7321	L+3(+)
-1.8549	L+3(B)	-1.8749	L+3(-)	-1.9063	L+3(-)	-1.7354	L+3(-)
-1.9938	L+2(A)	-2.0102	L+2(+)	-2.0402	L+2(+)	-1.8781	L+2(+)
-1.9941	L+2(B)	-2.0181	L+2(-)	-2.0466	L+2(-)	-1.8914	L+2(-)
-2.1142	L+1(A)	-2.1171	L+1(+)	-2.1416	L+1(+)	-1.9897	L+1(+)
-2.1142	L+1(B)	-2.1545	L+1(-)	-2.1912	L+1(-)	-2.0328	L+1(-)
-2.5034	L+0	-2.5252	L+0	-2.5571	L+0	-2.3996	L+0
-2.9736	E_f	-2.9922	E_f	-	E_f	-2.4755	E_f
-3.0989	H-0(A)	-3.1122	H-0(+)	-3.1395	H-0(+)	-2.5678	DS-0
-3.0989	H-0(B)	-3.1234	H-0(-)	-3.1491	H-0(-)	-2.9897	H-0(+)
-3.5996	H-1(A)	-3.6146	H-1(+)	-3.2777	IS-0	-2.9944	H-0(-)
-3.6005	H-1(B)	-3.6157	H-1(-)	-3.5279	IS-1	-3.4675	H-1(+)
-4.7058	H-2(A)	-3.8857	IS-0	-3.6431	H-1(+)	-3.4739	H-1(-)
-4.7058	H-2(B)	-3.8972	IS-1	-3.6483	H-1(-)	-4.0102	IS-1
-4.7142	-	-4.7195	H-2(+)	-4.1028	IS-2	-4.1746	IS-2
-4.7142	-	-4.7226	H-2(-)	-4.4571	IS-3	-4.4412	IS-3
-4.7142	-	-4.7306	-	-4.7460	H-2(+)	-4.5144	IS-4
-4.7142	-	-4.7321	-	-4.7542	H-2(-)	-4.5766	H-2(+)

4.3.3 Native defect in SWCNTs

The adsorption at defect sites produces a large electronic response that affects and sometimes even dominates the SWCNT capacitance and conductance sensitivity (Robinson *et al.*, 2006). SWCNT defects can be classified into four main groups: (1) *topological* (introduction of ring sizes other than hexagons), (2) *rehybridization* (ability of C atom to hybridize between sp^2 and sp^3), (3) *incomplete bonding defects* (vacancies, dislocation) and (4) *doping* with other element than C (Charlier, 2002). The defect formation energy E_{for} is defined as $E_{for} = E_{def} - E_P + n\mu_c$, where E_{def} is the total energy of SWCNT with a defect, E_P is the total energy of a pristine SWCNT, n (+) is number of C atom being removed from the defect, μ_c is chemical potential (total energy of pristine SWCNT divide by number of C atoms of pristine) (Padilha *et al.*, 2011)). The three lowest formation energy defects are Stone-Wales (SW, *topological*), diatom-vacancy (DV) and single-vacancy (SV) (Kabir and Van Vliet, 2016; Zhou *et al.*, 2014).

For the zigzag $(n,0)$ semiconducting SWCNT, $(7,0)$ SWCNT is the smallest diameter SWCNT. The $(5,0)$ is metallic because of curvature effect induced hybridization between σ - π bands. There are two series of zigzag semiconducting SWCNT which $mod(m-n,3)$ equal to 1 or 2. The $(8,0)$ SWCNT is the smallest diameter semiconduction SWCNT with $mod(m-n,3)$ equal to 2. The UV-vis depends on chiral index (n,m) and $mod(m-n,3)$ value (Weisman and Bachilo, 2003; Saidi and Norman, 2014). The signature of defect and UV-vis of $(7,0)$ SWCNT was previously studied by Saidi and Norman (Saidi and Norman, 2014).

In this study we studied the pristine SWCNT and native defects in SWCNT by first principles calculations. We focused our attentions on the semiconducting $(8,0)$

SWCNT which has $\text{mod}(m-n,3)$ equal to 2. The photon absorption energy and optical transitions associated with native defects are studied. The pristine SWCNT and defected semiconducting SWCNT are classified by using photon absorption energy and optical transitions. To obtain converged spectra, 2500 Lanczos iterations for pristine SWCNT and 5000 for defect SWCNTs were used.

In this work, in addition to the pristine (8,0) SWCNT, three native defects in the (8,0) SWCNT are studied. To study defects, a supercell approach with a supercell containing 3 primitive cells, resulting in a 96 C atoms cell, is used. To avoid spurious interactions between SWCNTs in the repetitive cells, a large a and b parameter of 21 Å is used. This leaves sufficient empty space between the neighboring SWCNTs as the diameter of the pristine SWCNT is only 6.36 Å. The defects in the (8,0) SWCNT included in this work, as schematically illustrated in Figure 4.22, are:

- (1) A single vacancy defect (SV) where a C atom is removed from the supercell. After an ionic optimization, the neighboring C atoms relax to form a five-member ring and a nine-member ring with a dangling bond (Nongnual and Limtrakul, 2011), shown in Figure 4.22(b).
- (2) A diatom vacancy defect (DV) where two adjacent C atoms with the C-C bond parallel with the SWCNT axis are removed from the supercell. After an ionic optimization, the neighboring C atoms relax to form two five-member rings and an eight-member ring in the (5-8-5) structure as shown in Figure 4.22(c).
- (3) A Stone-Wales defect (SW) where one ($\pi/2$) C-C bond, which the axis parallel to SWCNT axis ($\theta = 0$), is twisted by 90° such that the four adjacent

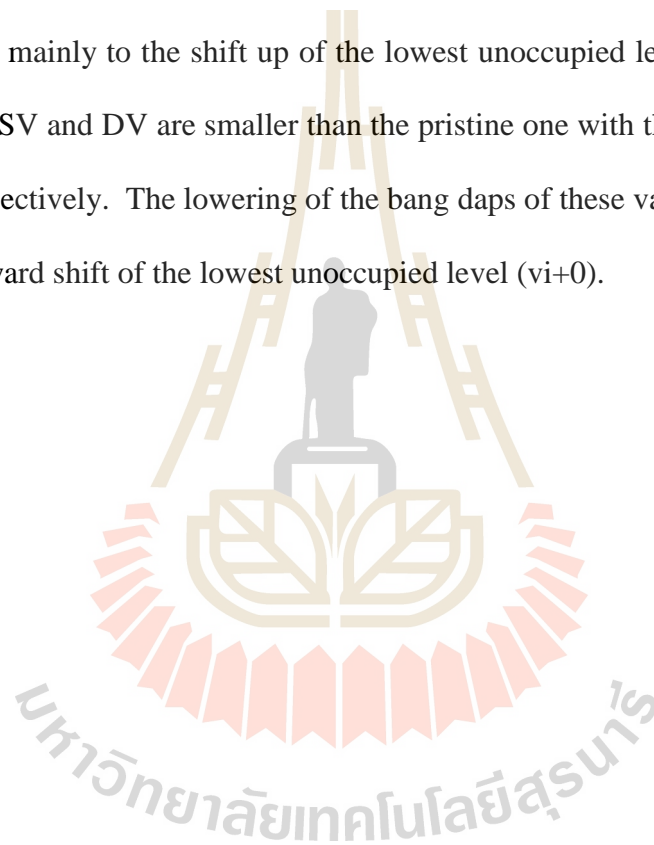
six-member rings turn into two five-member rings and two seven-member rings. This SW defect is reported to be the lowest energy defect (Kabir and Van Vliet, 2016). After an ionic optimization, the resulting pentagon-heptagon pair (5-7-7-5) structure is shown in Figure 4.22(d).

For all of models, we calculated the geometry and the electronic configurations at the ground state to explain the properties of the systems. First, we calculated the cell optimization of each model system including the pristine SWCNT as well as the three defected SWCNTs. All atoms in the supercell are allowed to relax until the atomic forces on each atom become less than 2.3×10^{-4} Ry/a.u. The optimized electronic configuration can be used to calculate the band structures, density of states (DOS) and finally optical absorption spectra.

3.3.4 Electronic structures of native defect in SWCNTs

The calculated electronic levels of the pristine (8,0) SWCNT as well as those from the three defects (SV, DV, and SW) studied are shown in Table 4.9. We listed the calculated Eigen energies near the band edge. For the pristine SWCNT, we listed the occupied levels and unoccupied levels as H (HOMO, highest occupied molecular orbital) and L (LUMO, lowest unoccupied molecular orbital) with increasing index number as the level is moved away from the band edge. In addition, we also put the label (A) and (B) for levels with degeneracies. For the defected SWCNT, we listed the occupied levels and unoccupied levels as oc (occupied) and vi (virtual) with increasing index number as the level is moved away from the band edges. E_f indicates the Fermi level of the system.

Table 4.10 tabulates the calculated formation energies and electronic band gaps of the pristine (8,0) SWCNT and defected SWCNTs. The formation energies of defects are 2.38, 3.19 and 5.10 eV for SW, DV, and SV, respectively. The band gap of the pristine (8,0) SWCNT is 0.60 eV which is in great agreement with the value 0.60 eV reported in Ref. (Spataru *et al.*, 2004). The calculated electronic band gap of SW defect SWCNT is 0.74 eV which is slightly larger than the electronic band gap of pristine SWCNT due mainly to the shift up of the lowest unoccupied level (v_i+0). The band gaps of both SV and DV are smaller than the pristine one with the values 0.43 eV and 0.08 eV, respectively. The lowering of the band gaps of these vacancy defects are due to the downward shift of the lowest unoccupied level (v_i+0).



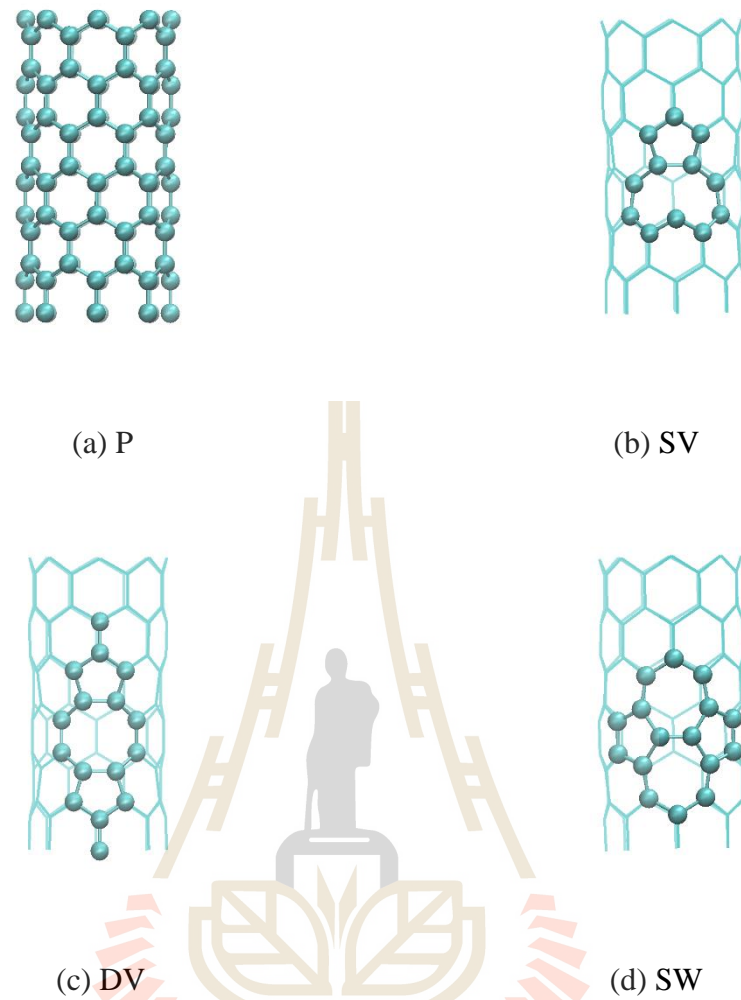


Figure 4.22 Schematic illustration of the structure of (a) pristine (8,0) SWCNT, (b) Single vacancy (SV) defect, (c) Diatom-vacancy (DV) defect and (d) Stone-Wales (SW) defect.

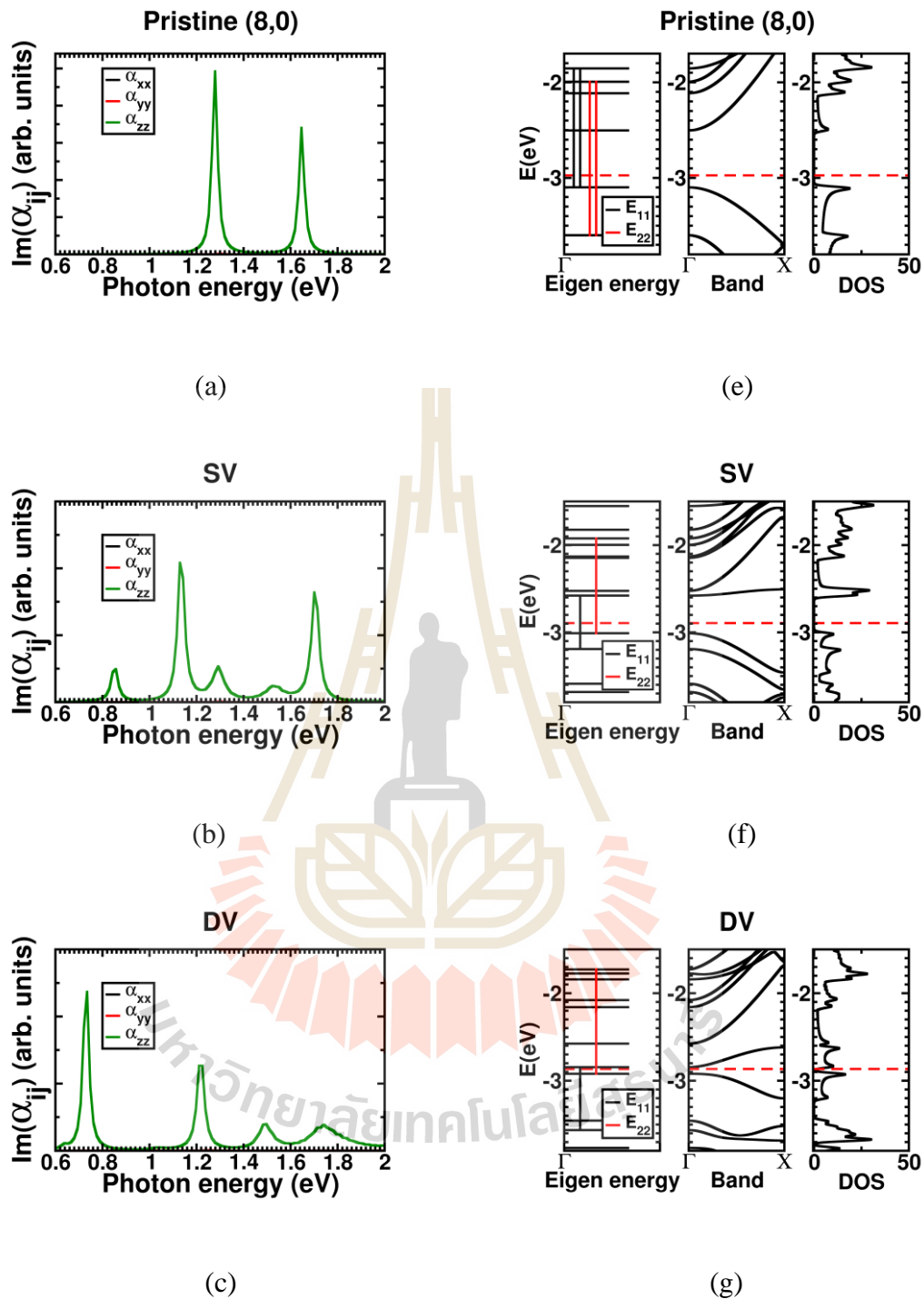


Figure 4.23 Calculated photon absorption energy of (a) pristine (8,0) SWCNT, (b)-(d) defected SWCNT. The corresponding optical transition states, band structures, and density of states are shown on the right (e)-(h). The z axis is defined along the tube direction.

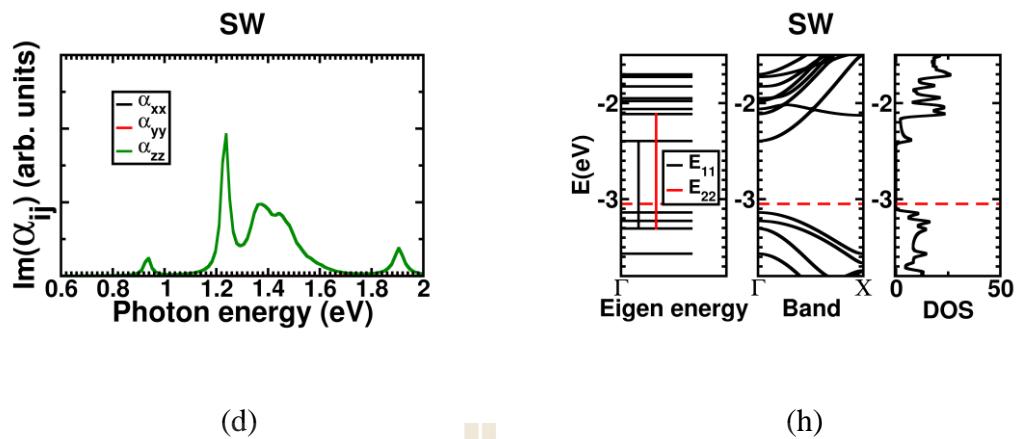


Figure 4.23 Calculated photon absorption energy of (a) pristine (8,0) SWCNT, (b)-(d) defected SWCNT. The corresponding optical transition states, band structures, and density of states are shown on the right (e)-(h). The z axis is defined along the tube direction (Continued).

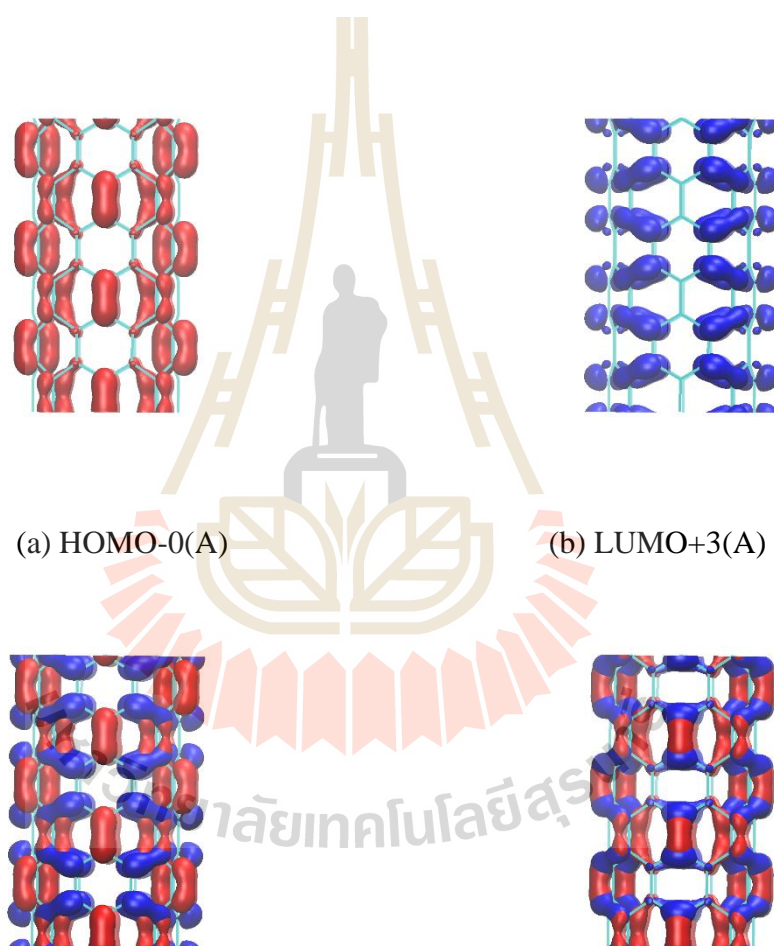
4.3.5 Optical transitions of native defect in SWCNTs

In order to obtain the photon absorption spectra from the calculated electronic levels, we have to determine the optical transition between electron Eigen states. The photon absorption energies are determined on the basis of band-to-band transitions (Bassani and Parravicini, 1989) and selection rules (Griffiths, 2005; Rohlfing and Louie, 2000; Hiroshi, 2012) of single-electron Eigen states. The calculated optical transition (Davidson-like algorithm (Ge *et al.*, 2014)) of pristine SWCNTs shows the E_{11} exciton composed of band-to-band transitions between the highest occupied molecular orbital H-0 band and unoccupied molecular orbital L+3 band. Because both bands are double degenerate, there are four singlet excitons formed between them, a dipole-allowed E_{11} state and three dark states: two degenerate states and one singlet

state. This is previously described by Mu *et al.* (Mu *et al.*, 2013) Our calculated PAE of E_{11} for pristine (8,0) SWCNT is 1.28 eV which is in a reasonable agreement with Ref. (Spataru *et al.*, 2004) (1.39 eV) and Ref. (Mu *et al.*, 2013) (1.53 eV). The orbital shapes of the initial and final states related to the transition are shown in Figure 4.24 and 4.25. Similarly analysis shows the E_{22} excitation in pristine (8,0) SWCNT composed of the band-to-band transitions between the lower occupied orbital H-1 to the unoccupied orbital L+2. Our calculated PAE of E_{22} for pristine (8,0) SWCNT is 1.65 eV which is in a reasonable agreement with Ref. (Spataru *et al.*, 2004) (1.51 eV) and Ref. (Mu *et al.*, 2013) (1.80 eV). Note that the values from Ref. (Mu *et al.*, 2013) are consistently higher than our values, due to the difference in computational approach used. The GW results are not suffered from the so-called DFT band gap underestimation. The optical transitions of pristine (8,0) SWCNT and defected (8,0) SWCNTs are shown in Table 4.11.

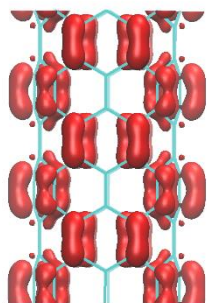
For the single vacancy defect, our calculated bright excitons of the optical transitions (principle components) for E_{11} process are from $oc-1 \rightarrow vi+0$ and for E_{22} from $oc-0 \rightarrow vi+5$. The orbital shapes of the initial and final states related to the transition as well as the combined plot of initial and final states are shown in Figure 4.26. For the diatomic vacancies defect, our calculated bright excitons of the optical transitions for E_{11} process are from $oc-2 \rightarrow vi+0$ and for E_{22} from $oc-0 \rightarrow vi+6$. The orbital shapes of the initial and final states related to the transition as well as the combined plot of initial and final states are shown in Figure 4.27. For the Stone-Wales defect, our calculated bright excitons of the optical transitions for E_{11} are from $oc-2 \rightarrow vi+0$ and for E_{22} from $oc-2 \rightarrow vi+1$. The orbital shapes of the initial and final states

related to the transition as well as the combined plot of initial and final states are shown in Figure 4.28. The components of the dipole polarizability (α_{ij}) are shown in Figure 4.23. The main component is from α_{zz} , because of SWCNT is a one-dimensional material with the tube axis align along the z-axis.

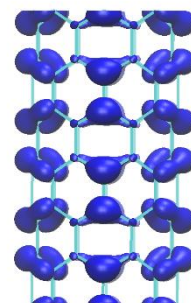


(c) H-0(A) \rightarrow L+3(A); dipole-allowed (d) H-0(A) \rightarrow L+3(B); dipole-forbidden

Figure 4.24 Relevant molecular orbitals for E_{11} (A_{11}) optical transition of the pristine (8,0) SWCNT; (c) the dipole-allowed transition and (d) the dipole forbidden.



(a) HOMO-0(B)



(b) LUMO+3(B)

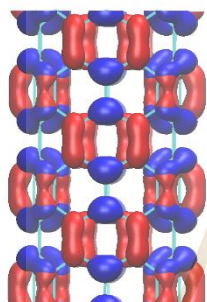
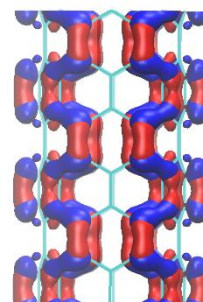
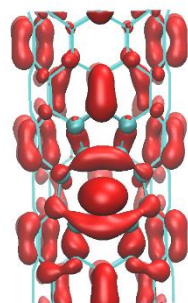
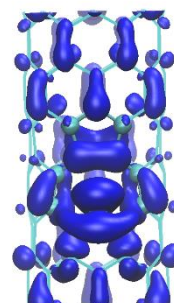
(c) H-0(B) \rightarrow L+3(B); dipole-allowed(d) H-0(B) \rightarrow L+3(A); dipole-forbidden

Figure 4.25 Relevant molecular orbitals for E_{11} (B_{11}) optical transition of the pristine (8,0) SWCNT; (c) the dipole-allowed transition and (d) the dipole forbidden.



(a) occ-1



(b) virt+0

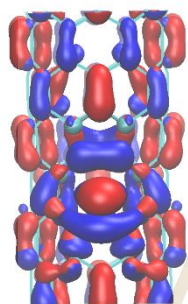
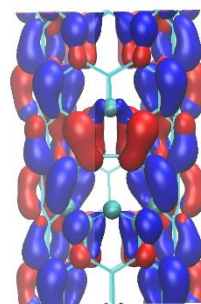
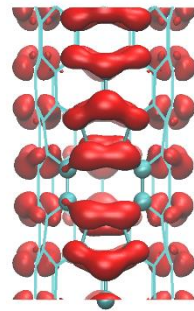
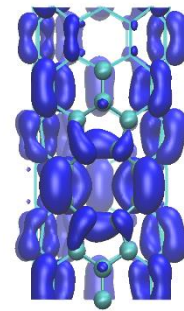
(c) occ-1 \rightarrow virt+0; dipole-allowed; E_{11} (d) occ-0 \rightarrow virt+5; dipole-allowed; E_{22}

Figure 4.26 Relevant molecular orbitals for E_{11} and E_{22} optical transitions of the single vacancy defect, SV, in (8,0) SWCNT; (c) the dipole-allowed E_{11} transition and (d) the dipole-allowed E_{22} transition.



(a) occ-2



(b) virt+0

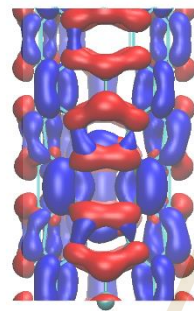
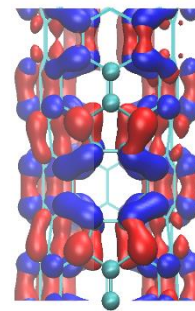
(c) occ-2 \rightarrow virt+0; dipole-allowed; E_{11} (d) occ-0 \rightarrow virt+6; dipole-allowed; E_{22}

Figure 4.27 Relevant molecular orbitals for E_{11} and E_{22} optical transitions of the diatom vacancy defect, DV, in (8,0) SWCNT; (c) the dipole-allowed E_{11} transition and (d) the dipole-allowed E_{22} transition.

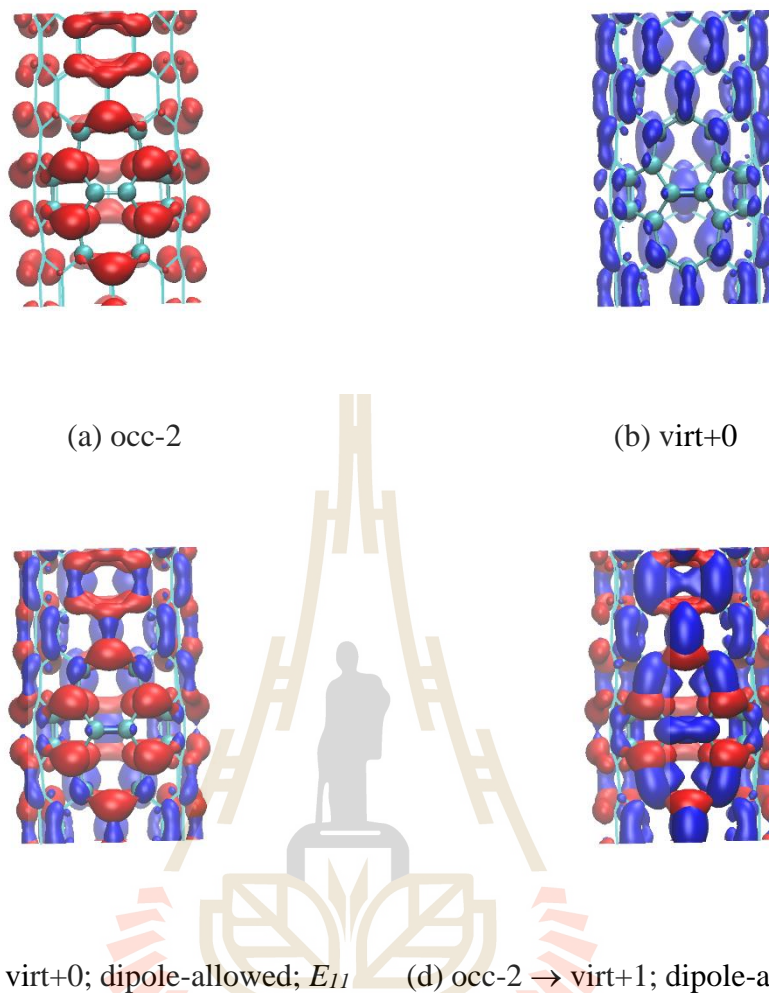


Figure 4.28 Relevant molecular orbitals for E_{11} and E_{22} optical transitions of the Stone-Wales defect, SW, in (8,0) SWCNT; (c) the dipole-allowed E_{11} transition and (d) the dipole-allowed E_{22} transition.

Table 4.9 Calculated Eigen energies in eV at the Γ -point of the pristine (8,0) SWCNT and defected (8,0) SWCNTs, namely, single vacancy (SV), diatom vacancy (DV), and Stone-Wales (SW). To aid identification of the energy levels, the labels are shown in column 2 and 6 for pristine SWCNT and defected SWCNTs, respectively. The Fermi energy (E_f) of each system is also shown. Label abbreviations: L = lowest unoccupied molecular orbital, H = highest occupied molecular orbital, vi = virtual state, oc = occupied state.

Pristine	Label	Energy (eV)			Label
		SV	DV	SW	
-1.8549	L+3(A)	-1.8237	-1.7286	-1.7278	vi+6
-1.8549	L+3(B)	-1.9233	-1.7743	-1.8264	vi+5
-1.9938	L+2(A)	-1.9974	-1.8421	-1.9499	vi+4
-1.9941	L+2(B)	-2.1308	-2.0785	-1.9791	vi+3
-2.1142	L+1(A)	-2.1456	-2.1597	-2.0618	vi+2
-2.1142	L+1(B)	-2.5243	-2.5758	-2.1141	vi+1
-2.5034	L+0	-2.5787	-2.8449	-2.3953	vi+0
-2.9736	E_f	-2.8933	-2.8655	-3.0492	E_f
-3.0989	H-0(A)	-3.0096	-2.9202	-3.1382	oc-0
-3.0989	H-0(B)	-3.1901	-3.4555	-3.2263	oc-1
-3.5996	H-1(A)	-3.5878	-3.5635	-3.3053	oc-2
-3.6005	H-1(B)	-3.6829	-3.7678	-3.5676	oc-3
-4.7058	H-2(A)	-4.2628	-4.0381	-4.3094	oc-4
-4.7058	H-2(B)	-4.3894	-4.5168	-4.6384	oc-5
-4.7142	-	-4.7028	-4.6575	-4.6545	oc-6
-4.7142	-	-4.7187	-4.6913	-4.6807	oc-7

4.3.6 Photon absorption spectra of native defect in SWCNTs

The photon absorption spectra can be used to identify the pristine SWCNTs as well as native defects in them. This is because the photon absorption spectra are related to the electronic band structure states of pristine and defects in semiconducting SWCNT. As previously mentioned, in this study we focused our attentions on the pristine (8,0) SWCNT and three types of defects in the pristine (8,0) SWCNTs, i.e., SV, DV and SW defects using a supercell approach (Saidi and Norman, 2014).

Based on the allowed optical transitions (Table 4.11) and the calculated Eigen energy of each state (Table 4.9), the photon absorption energies are shown in Table 4.12. For the E_{11} optical transition, we obtained the photon absorption energies (PAE) associated with SV, DV, and SW of 0.85, 0.73, and 0.94 eV, respectively. These PAEs are all smaller than the calculated PAE of pristine (8,0) SWCNT of 1.28 eV. Because the relative energies are expected to be more accurate than the absolute PAE due to the well-known DFT band gap underestimation, we calculate the relative PAE (label as 'Shift' in Table 4.12) associated these defects relative to that of pristine PAE value. The characteristic PAE for the E_{11} optical transition of SV, DV, and SW defects are expected at 0.43, 0.55, and 0.34 eV below the PAE of pristine SWCNT. These relative PAEs are compared favorably with the calculated values in Ref. (Mu *et al.*, 2013) which expects the E_{11} PAEs of SV and SW at 0.56 and 0.18 eV below the PAE of pristine SWCNT.

For the E_{22} optical transition (Table 4.13), to our knowledge, there is no computational values reported for SV, DV, and SW defects in (8,0) SWCNT. Therefore, our values could serve as the first prediction for further experimental

identification of these defects. We obtained the PAE associated with SV, DV, and SW of 1.14, 1.22, and 1.24 eV, respectively. These are all smaller than the calculated PAE of pristine (8,0) SWCNT of 1.65 eV. Therefore, the characteristic PAE for the E_{22} optical transition of SV, DV, and SW defects are expected to see at 0.51, 0.43, and 0.41 eV below the PAE of pristine SWCNT.

Table 4.10 Calculated formation energies and band gaps of the pristine (8,0) SWCNT and defected (8,0) SWCNTs, namely, single vacancy (SV), diatom vacancy (DV), and Stone-Wales (SW). The band gaps are calculated from the lowest unoccupied state minus the highest occupied state in Table 4.9.

System	Band gap (Γ ; eV)	E_{for} (eV)
Pristine (8,0)	0.60	0.00
SV	0.43	5.10
DV	0.08	3.19
SW	0.74	2.38

Table 4.11 Electric dipole allowed (di-al) and forbidden (di-fo) optical transitions of pristine and defected (8,0) SWCNTs. Abbreviations: P = pristine, SW = Stone-Wales, DV = diatom vacancies, SV = single vacancy.

System	E_{11} , di-al	E_{11} , di-fo
P	H-0(A) \rightarrow L+3(A)	H-0(A) \rightarrow L+3(B)
P	H-0(B) \rightarrow L+3(B)	H-0(B) \rightarrow L+3(A)
SV	oc-1 \rightarrow vi+0	-
DV	oc-2 \rightarrow vi+0	-
SW	oc-2 \rightarrow vi+0	-
	E_{22} , di-al	E_{22} , di-fo
P	H-1(A) \rightarrow L+2(B)	H-1(A) \rightarrow L+2(A)
P	H-1(B) \rightarrow L+2(A)	H-1(B) \rightarrow L+2(B)
SV	oc-0 \rightarrow vi+5	-
DV	oc-0 \rightarrow vi+6	-
SW	oc-2 \rightarrow vi+1	-

Table 4.12 E_{11} Photon absorption energy (PAE) in eV of pristine and defected SWCNTs. Abbreviations: P = pristine, SW = Stone-Wales, DV = diatom vacancies, SV = single vacancy, IS = impurity state, Shift = (PAE-defect) - (PAE-pristine).

		Model (E_{11})				
Source	System	PAE pristine	PAE defect	Shift	Initial state	Final state
Exp ^a	P (8,0)	1.598	-	-	-	-
LDA ^b	P (8,0)	1.39	-	-	-	-
PBE ^c	SW (7,0)	0.89	0.88	-0.01	-	-
	DV (7,0)	0.89	0.81	-0.08	-	-
TB-BSE ^d	IS (20,0)	0.64	0.62	-0.02	-	-
GW+BSE ^e	P (8,0)	1.53	-	-	H-0	L+3
	O (8,0)	1.53	1.45	-0.08	H-O(+)	L+3(-)
	O (8,0)	1.53	1.62	0.09	H-O(-)	L+3(+)
	2H (8,0)	1.53	1.27	-0.26	State ₁	State ₂
	SV (8,0)	1.53	0.97	-0.56	-	-
	SW(8,0)	1.53	1.35	-0.18	-	-
Present	P (8,0)	1.28	-	-	H-0(A)	L+3(A)
	P (8,0)	1.28	-	-	H-0(B)	L+3(B)
	SV (8,0)	1.28	0.85	-0.43	oc-1	vi+0
	DV (8,0)	1.28	0.73	-0.55	oc-2	vi+0
	SW (8,0)	1.28	0.94	-0.34	oc-2	vi+0

^a Ref. (Weisman and Bachilo, 2003); Experimental measurement of the pristine (8,0) SWCNT

^b Ref. (Spataru *et al.*, 2004); LDA calculations of the pristine (8,0) SWCNT

^c Ref. (Saidi and Norman, 2014); PBE calculations of 3 units supercell of (7,0) SWCNT

^d Ref. (Konabe and Watanabe, 2011); Tight-binding+BSE calculations of the (20,0) SWCNT

^e Ref. (Mu *et al.*, 2013); GW+BSE, PBE calculations of the pristine (8,0) SWCNT

Table 4.13 E_{22} Photon absorption energy (PAE) in eV of pristine and defected SWCNTs. Abbreviations: P = pristine, SW = Stone-Wales, DV = diatom vacancies, SV = single vacancy, IS = impurity state, Shift = (PAE-defect) - (PAE-pristine).

		Model (E_{22})				
Source	System	PAE pristine	PAE defect	Shift	Initial state	Final state
Exp ^a	P (8,0)	1.878	-	-	-	-
LDA ^b	P (8,0)	1.51	-	-	-	-
PBE ^c	SW (7,0)	2.19	2.40	0.21	-	-
	DV (7,0)	2.19	2.29	0.10	-	-
GW+BSE ^e	P (8,0)	1.79	-	-	H-1	L+2
Present	P (8,0)	1.65	-	-	H-1(A)	L+2(B)
	P (8,0)	1.65	-	-	H-1(B)	L+2(A)
	SV (8,0)	1.65	1.14	-0.51	oc-0	vi+5
	DV (8,0)	1.65	1.22	-0.43	oc-0	vi+6
	SW (8,0)	1.65	1.24	-0.41	oc-2	vi+1

^a Ref. (Weisman and Bachilo, 2003); Experimental measurement of the pristine (8,0)

SWCNT

^b Ref. (Spataru *et al.*, 2004); LDA calculations of the pristine (8,0) SWCNT

^c Ref. (Saidi and Norman, 2014); PBE calculations of 3 units supercell of (7,0)

SWCNT

^e Ref. (Mu *et al.*, 2013); GW+BSE, PBE calculations of the pristine (8,0) SWCNT

CHAPTER V

CONCLUSIONS

5.1 Configurations

This is a theoretical study report of pure hydrazine doped single-walled carbon nanotubes (SWCNTs) which obtained donor state (DS) in the electronic band structure. The density functional theory (DFT) corrected by van der Waals (vdW) interaction is important for calculation that form the hydrogen bond network (HBN), which cause for charge transfer from hydrazine molecules to SWCNT. The DS occurrence, it depends on both HBN and configurations of a hydrazine molecule; this molecule a H atom of both side of itself pointing to a N atom of another molecule (a N atom of itself could pointed by a H atom of another molecule). For the hydrazine gas phase doped SWCNT it cannot occur DS, it is a vdW interaction and the electronic band structure state is impurity state below the maximum valence state (ISBMVS). When HBN occurrence, the intermolecular interaction is a noncovalent interactions (NCI), it consists of vdW, N-H... π and N-H...N interactions, and the electronic band structure state are impurity state close to the maximum valence state (ISCMVS) and DS.

5.2 NMR chemical shifts (δ)

The DFT study on the nuclear magnetic resonance (NMR) chemical shift (δ) of hydrazine doped SWCNT and obtained the DS. To confirm the configuration which obtained DS we found ^{13}C NMR δ shifts to a lower frequency (4 ppm) for the case of N-H $\cdots\pi$ interaction when compare to pristine SWCNT, and shifts to a higher frequency for the case of vdW interaction. For ^1H NMR δ of hydrazine molecules, when HBN occur the ^1H NMR δ shifts to a higher frequency when compare to isolated hydrazine (Gauche), and more shifts to a higher frequency (10 ppm compare to TMS) for a molecule that satisfied the condition to occur DS. The signatures of ^1H NMR δ could use to identify the DS in electronic band structure state.

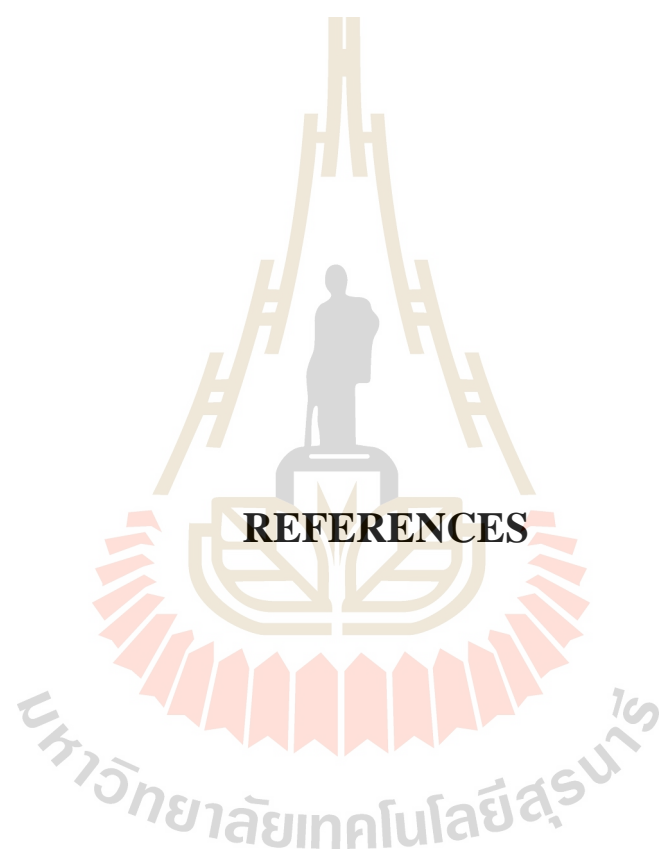
5.3 Ultraviolet-visibility (UV-Vis) spectroscopic

The TDDFT study on the photon absorption energy (PAE) of pristine and doped SWCNTs. The PAE for E_{11} of pristine SWCNT is 1.278 eV. For doped SWCNTs, in the case of impurity state (IS) occurrence both of ISBMVS and ISCMVS the PAE are 1.279 and 1.273 eV, have a slight change with values 1 and -5 meV compare to pristine SWCNT, respectively. In the case of DS occurrence the PAE is 1.291 eV has a slight change with value 13 meV compare to pristine SWCNT, this signature use to identify DS (n-type) in doped SWCNTs. For E_{22} in the case of DS occurrence the PAE change to lower energy with value 21 meV compare to pristine SWCNT.

The physisorption of hydrazine doped SWCNT is a cause for change the optical transition of E_{11} peak of PAE. When hydrazine caused the degenerate band of SWCNTs

to split into nondegenerate bands ((-),(+)), the optical transitions also changed. In the case DS occurrence the dark excitons changed to bright excitons are the optical transitions from HOMO-0(+) \rightarrow LUMO+3(+) and HOMO-0(-) \rightarrow LUMO+3(-), the bright exciton has slight change in photon absorption energy that change to higher energy with value 13 meV compare to pristine SWCNTs.

We have calculated the photon absorption energies of pristine and defected (8,0) single-walled carbon nanotubes (SWCNT) using time dependent density functional theory based on the electronic structures obtained from the density functional theory corrected by the van der Waals (vdW) interactions. Our calculated E_{11} and E_{22} PAE of pristine SWCNT are 1.28 eV and 1.65 eV, respectively. These values are in a reasonable agreement, albeit lower due to the well-known DFT band gap underestimation, with the GW calculations (1.53 eV and 1.79 eV) and experimental values (1.598 eV and 1.878 eV). Because the band gap underestimation is expected to be systematic, we calculated the relative PAE of the three defects, namely single vacancy (SV), diatom vacancy (DV), and Stone-Wales (SW) with respect to the PAE of pristine SWCNT. For E_{11} optical transition, our calculated characteristic PAE of SV, DV, and SW defects are 0.43, 0.55, and 0.34 eV below the PAE of pristine (8,0) SWCNT. For E_{22} optical transition, our calculated characteristic PAE of SV, DV, and SW defects are 0.51, 0.43, and 0.41 eV below the PAE of pristine (8,0) SWCNT. These PAE predictions can be used to identify defects in (8,0) SWCNT. The detail of the defect formation energies, Eigen states, density of states and photon transition characteristics are also provided.



REFERENCES

REFERENCES

- Agusta, M. K., David, M., Nakanishi, H., and Kasai, H. (2010). Hydrazine (N_2H_4) adsorption on Ni(100) – Density functional theory investigation. **Surface Science** 604: 245.
- Avouris, P., Freitag, M., and Perebeinos, V. (2008). Carbon-nanotube photonics and optoelectronics. **Nature Photonics** 2: 341.
- Bader, R. F. W., Carroll, M. T., Cheeseman, J. R., and Chang, C. (1987). Properties of atoms in molecules: atomic volumes. **Journal of the American Chemical Society** 109: 7968.
- Bai, L., and Zhou, Z. (2007). Computational study of B- or N-doped single-walled carbon nanotubes as NH_3 and NO_2 sensors. **Carbon** 45: 2105.
- Barkelid, M., and Zwiller, V. (2013). Single carbon nanotube photovoltaic device. **Journal of Applied Physics** 114.
- Barone, V., Casarin, M., Forrer, D., Pavone, M., Sambri, M., and Vittadini, A. (2009). Role and effective treatment of dispersive forces in materials: Polyethylene and graphite crystals as test cases. **Journal of Computational Chemistry** 30: 934.
- Bassani, G. F., and Parravicini, G. P. (1989). **Electronic states and optical transitions in solids**. Pergamon Press.
- Bekyarova, E., Ni, Y., Malarkey, E. B., Montana, V., McWilliams, J. L., Haddon, R. C., and Parpura, V. (2005). Applications of carbon nanotubes in biotechnology and biomedicine. **Journal of biomedical nanotechnology** 1: 3.

- Bonhomme, C., Gervais, C., Babonneau, F., Coelho, C., Pourpoint, F., Azais, T., Ashbrook, S. E., Griffin, J. M., Yates, J. R., Mauri, F., and Pickard, C. J. (2012). First-principles calculation of NMR parameters using the gauge including projector augmented wave method: a chemist's point of view. **Chemical reviews** 112: 5733.
- Callaway, J. (1955). Orthogonalized Plane Wave Method. **Physical Review** 97: 933.
- Chakrapani, V., Angus, J. C., Anderson, A. B., Wolter, S. D., Stoner, B. R., and Sumanasekera, G. U. (2007). Charge Transfer Equilibria Between Diamond and an Aqueous Oxygen Electrochemical Redox Couple. **Science** 318: 1424.
- Champlain, J. G. (2011). A first principles theoretical examination of graphene-based field effect transistors. **Journal of Applied Physics** 109.
- Charlier, J. C. (2002). Defects in Carbon Nanotubes. **Accounts of chemical research** 35: 1063.
- Cheng, J., Kang, C., Zhu, W., Luo, X., Pua, C. M., Chen, K., Shen, J., and Jiang, H. (2003). N-Methylformamide–Benzene Complex as a Prototypical Peptide N–H··· π Hydrogen-Bonded System: Density Functional Theory and MP2 Studies. **The Journal of Organic Chemistry** 68: 7490.
- Contreras-García, J., Johnson, E. R., Keinan, S., Chaudret, R., Piquemal, J.-P., Beratan, D. N., and Yang, W. (2011). NCIPLLOT: A Program for Plotting Noncovalent Interaction Regions. **Journal of Chemical Theory and Computation** 7: 625.
- Cui, J. B., Sordan, R., Burghard, M., and Kern, K. (2002). Carbon nanotube memory devices of high charge storage stability. **Applied Physics Letters** 81: 3260.
- Daff, T. D., and de Leeuw, N. H. (2011). Ab Initio Molecular Dynamics Simulations of the Cooperative Adsorption of Hydrazine and Water on Copper Surfaces:

- Implications for Shape Control of Nanoparticles. **Chemistry of Materials** 23: 2718.
- De Volder, M. F. L., Tawfick, S. H., Baughman, R. H., and Hart, A. J. (2013). Carbon Nanotubes: Present and Future Commercial Applications. **Science** 339: 535.
- Desai, S. C., Willitsford, A. H., Sumanasekera, G. U., Yu, M., Tian, W. Q., Jayanthi, C. S., and Wu, S. Y. (2010). Hypergolic fuel detection using individual single walled carbon nanotube networks. **Journal of Applied Physics** 107.
- Dresselhaus, M. S., Dresselhaus, G., and Saito, R. (1995). Physics of carbon nanotubes. **Carbon** 33: 883.
- Du, Q.-S., Wang, Q.-Y., Du, L.-Q., Chen, D., and Huang, R.-B. (2013). Theoretical study on the polar hydrogen- π (Hp- π) interactions between protein side chains. **Chemistry Central Journal** 7: 92.
- Duer, M. J. (2005). **Introduction to Solid-State NMR Spectroscopy**. Wiley.
- Engtrakul, C., Irurzun, V. M., Gjersing, E. L., Holt, J. M., Larsen, B. A., Resasco, D. E., and Blackburn, J. L. (2012). Unraveling the ^{13}C NMR chemical shifts in single-walled carbon nanotubes: dependence on diameter and electronic structure. **Journal of the American Chemical Society** 134: 4850.
- Freeman, D. D., Choi, K., and Yu, C. (2012). N-Type Thermoelectric Performance of Functionalized Carbon Nanotube-Filled Polymer Composites. **PLoS ONE** 7: e47822.
- Gabor, N. M., Zhong, Z., Bosnick, K., Park, J., and McEuen, P. L. (2009). Extremely efficient multiple electron-hole pair generation in carbon nanotube photodiodes. **Science** 325: 1367.

- Ge, X., Binnie, S. J., Rocca, D., Gebauer, R., and Baroni, S. (2014). turboTDDFT 2.0—Hybrid functionals and new algorithms within time-dependent density-functional perturbation theory. **Computer Physics Communications** 185: 2080.
- Griffiths, D. J. (2005). **Introduction to Quantum Mechanics**. Pearson Prentice Hall.
- Han, W.-Q., and Zettl, A. (2003). Coating Single-Walled Carbon Nanotubes with Tin Oxide. **Nano letters** 3: 681.
- Henkelman, G., Arnaldsson, A., and Jónsson, H. (2006). A fast and robust algorithm for Bader decomposition of charge density. **Computational Materials Science** 36: 354.
- Hiroshi, A. (2012). Exciton states and optical properties of carbon nanotubes. **Journal of Physics: Condensed Matter** 24: 483001.
- Hohenberg, P., and Kohn, W. (1964). Inhomogeneous Electron Gas. **Physical Review** 136: B864.
- Jena, D., Fang, T., Zhang, Q., and Xing, H. (2008). Zener tunneling in semiconducting nanotube and graphene nanoribbon p–n junctions. **Applied Physics Letters** 93.
- Johnson, E. R., Keinan, S., Mori-Sánchez, P., Contreras-García, J., Cohen, A. J., and Yang, W. (2010). Revealing Noncovalent Interactions. **Journal of the American Chemical Society** 132: 6498.
- Ju, X.-H., and Xiao, H.-M. (2002). Intermolecular interaction of hydrazine dimers: a comparative theoretical study. **Journal of Molecular Structure: THEOCHEM** 588: 79.

- Kabir, M., and Van Vliet, K. J. (2016). Kinetics of Topological Stone–Wales Defect Formation in Single-Walled Carbon Nanotubes. **The Journal of Physical Chemistry C** 120: 1989.
- Kaempgen, M., Duesberg, G. S., and Roth, S. (2005). Transparent carbon nanotube coatings. **Applied Surface Science** 252: 425.
- Kawazoe, H., Yasukawa, M., Hyodo, H., Kurita, M., Yanagi, H., and Hosono, H. (1997). P-type electrical conduction in transparent thin films of CuAlO₂. **Nature** 389: 939.
- Kodama, R. H., Makhlof, S. A., and Berkowitz, A. E. (1997). Finite Size Effects in Antiferromagnetic NiO Nanoparticles. **Physical Review Letters** 79: 1393.
- Kohn, W. (1999). Nobel Lecture: Electronic structure of matter—wave functions and density functionals. **Reviews of Modern Physics** 71: 1253.
- Kohn, W., and Sham, L. J. (1965). Self-Consistent Equations Including Exchange and Correlation Effects. **Physical Review** 140: A1133.
- Komarov, F., and Mironov, A. (2004). Carbon nanotubes: present and future. **Physics and Chemistry of Solid State** 5: 411.
- Konabe, S., and Watanabe, K. (2011). Mechanism for optical activation of dark spin-triplet excitons in hydrogenated single-walled carbon nanotubes. **Physical Review B** 83.
- Kong, J., and Dai, H. (2001). Full and Modulated Chemical Gating of Individual Carbon Nanotubes by Organic Amine Compounds. **The Journal of Physical Chemistry B** 105: 2890.
- Kong, J., Franklin, N. R., Zhou, C., Chapline, M. G., Peng, S., Cho, K., and Dai, H. (2000). Nanotube Molecular Wires as Chemical Sensors. **Science** 287: 622.

- Leenaerts, O., Partoens, B., and Peeters, F. M. (2008). Adsorption of H₂O, NH₃, CO, NO₂, and NO on graphene: A first-principles study. **Physical Review B** 77.
- Liu, K., Deslippe, J., Xiao, F., Capaz, R. B., Hong, X., Aloni, S., Zettl, A., Wang, W., Bai, X., Louie, S. G., Wang, E., and Wang, F. (2012). An atlas of carbon nanotube optical transitions. **Nature Nanotechnology** 7: 325.
- Malcioğlu, O. B., Gebauer, R., Rocca, D., and Baroni, S. (2011). turboTDDFT – A code for the simulation of molecular spectra using the Liouville–Lanczos approach to time-dependent density-functional perturbation theory. **Computer Physics Communications** 182: 1744.
- Marques, M., d’Avezac, M., and Mauri, F. (2006). Magnetic response and NMR spectra of carbon nanotubes from ab initio calculations. **Physical Review B** 73.
- Marques, M. A. L., Maitra, N. T., Nogueira, F. M. S., Gross, E. K. U., and Rubio, A. (2012). **Fundamentals of Time-Dependent Density Functional Theory**. Springer Berlin Heidelberg.
- Mauri, F., Pfrommer, B. G., and Louie, S. G. (1996). *Ab Initio* Theory of NMR Chemical Shifts in Solids and Liquids. **Physical Review Letters** 77: 5300.
- McEuen, P. L., Fuhrer, M. S., and Park, H. (2002). Single-walled carbon nanotube electronics. **Nanotechnology, IEEE Transactions on** 1: 78.
- Mirri, F., Ma, A. W. K., Hsu, T. T., Behabtu, N., Eichmann, S. L., Young, C. C., Tsentalovich, D. E., and Pasquali, M. (2012). High-Performance Carbon Nanotube Transparent Conductive Films by Scalable Dip Coating. **American Chemical Society Nano** 6: 9737.
- Mistry, K. S., Larsen, B. A., Bergeson, J. D., Barnes, T. M., Teeter, G., Engtrakul, C., and Blackburn, J. L. (2011). n-Type Transparent Conducting Films of Small

- Molecule and Polymer Amine Doped Single-Walled Carbon Nanotubes. **American Chemical Society Nano** 5: 3714.
- Movlaroooy, T., Kompany, A., Hosseini, S. M., and Shahtahmasebi, N. (2010). Optical absorption and electron energy loss spectra of single-walled carbon nanotubes. **Computational Materials Science** 49: 450.
- Mu, J., Ma, Y., Yin, H., Liu, C., and Rohlfing, M. (2013). Photoluminescence of Single-Walled Carbon Nanotubes: The Role of Stokes Shift and Impurity Levels. **Physical Review Letters** 111: 137401.
- Mueller, T., Kinoshita, M., Steiner, M., Perebeinos, V., Bol, A. A., Farmer, D. B., and Avouris, P. (2010). Efficient narrow-band light emission from a single carbon nanotube p-n diode. **Nature Nanotechnology** 5: 27.
- Nongnual, T., and Limtrakul, J. (2011). Healing of a Vacancy Defect in a Single-Walled Carbon Nanotube by Carbon Monoxide Disproportionation. **The Journal of Physical Chemistry C** 115: 4649.
- Nonoguchi, Y., Ohashi, K., Kanazawa, R., Ashiba, K., Hata, K., Nakagawa, T., Adachi, C., Tanase, T., and Kawai, T. (2013). Systematic conversion of single walled carbon nanotubes into n-type thermoelectric materials by molecular dopants. **Scientific reports** 3: 3344.
- Oh, H. S., Shin, K., Lee, S. J., Shim, D., Han, J. H., and Myoung, J.-M. (2012). The p-type doping in SWCNT transparent conductive films by spontaneous reduction potential using Ag and Ni. **Chemical Physics Letters** 548: 29.
- Ohta, H., and Hosono, H. (2004). Transparent oxide optoelectronics. **Materials Today** 7: 42.

- Ottiger, P., Pfaffen, C., Leist, R., Leutwyler, S., Bachorz, R. A., and Klopper, W. (2009). Strong N–H $\cdots\pi$ Hydrogen Bonding in Amide–Benzene Interactions. **The Journal of Physical Chemistry B** 113: 2937.
- Padilha, J. E., Amorim, R. G., Rocha, A. R., da Silva, A. J. R., and Fazzio, A. (2011). Energetics and stability of vacancies in carbon nanotubes. **Solid State Communications** 151: 482.
- Paolo, G., Stefano, B., Nicola, B., Matteo, C., Roberto, C., Carlo, C., Davide, C., Guido, L. C., Matteo, C., Ismaila, D., Andrea Dal, C., Stefano de, G., Stefano, F., Guido, F., Ralph, G., Uwe, G., Christos, G., Anton, K., Michele, L., Layla, M.-S., Nicola, M., Francesco, M., Riccardo, M., Stefano, P., Alfredo, P., Lorenzo, P., Carlo, S., Sandro, S., Gabriele, S., Ari, P. S., Alexander, S., Paolo, U., and Renata, M. W. (2009). QUANTUM ESPRESSO: a modular and open-source software project for quantum simulations of materials. **Journal of Physics: Condensed Matter** 21: 395502.
- Perdew, J. P., Burke, K., and Ernzerhof, M. (1996). Generalized Gradient Approximation Made Simple. **Physical Review Letters** 77: 3865.
- Pickard, C. J., and Mauri, F. (2001). All-electron magnetic response with pseudopotentials: NMR chemical shifts. **Physical Review B** 63: 245101.
- Rana, K., Singh, J., and Ahn, J.-H. (2014). A graphene-based transparent electrode for use in flexible optoelectronic devices. **Journal of Materials Chemistry C** 2: 2646.
- Rashidi, A. M., Nouralishahi, A., Khodadadi, A. A., Mortazavi, Y., Karimi, A., and Kashefi, K. (2010). Modification of single wall carbon nanotubes (SWNT) for hydrogen storage. **International Journal of Hydrogen Energy** 35: 9489.

- Ren, F. D., Cao, D. L., Wang, W. L., Ren, J., Hou, S. Q., and Chen, S. S. (2009). A theoretical study on unusual intermolecular T-shaped X-H... π interactions between the singlet state HB=BH and HF, HCl, HCN or H₂C₂. **Journal of Molecular Modeling** 15: 515.
- Ren, P., Zheng, A., Pan, X., Han, X., and Bao, X. (2013). DFT Study on the NMR Chemical Shifts of Molecules Confined in Carbon Nanotubes. **The Journal of Physical Chemistry C** 117: 23418.
- Robinson, J. A., Snow, E. S., Badescu, S. C., Reinecke, T. L., and Perkins, F. K. (2006). Role of defects in single-walled carbon nanotube chemical sensors. **Nano letters** 6: 1747.
- Rohlfing, M., and Louie, S. G. (2000). Electron-hole excitations and optical spectra from first principles. **Physical Review B** 62: 4927.
- Rydberg, H., Lundqvist, B. I., Langreth, D. C., and Dion, M. (2000). Tractable nonlocal correlation density functionals for flat surfaces and slabs. **Physical Review B** 62: 6997.
- Saidi, W. A., and Norman, P. (2014). Spectroscopic signatures of topological and diatom-vacancy defects in single-walled carbon nanotubes. **Physical Chemistry Chemical Physics** 16: 1479.
- Shim, M., Javey, A., Shi Kam, N. W., and Dai, H. (2001). Polymer Functionalization for Air-Stable n-Type Carbon Nanotube Field-Effect Transistors. **Journal of the American Chemical Society** 123: 11512.
- Shin, D. W., Lee, J. H., Kim, Y. H., Yu, S. M., Park, S. Y., and Yoo, J. B. (2009). A role of HNO₃ on transparent conducting film with single-walled carbon nanotubes. **Nanotechnology** 20: 475703.

- Sohn, S., and Han, Y. S. (2011). **Organic Light Emitting Diode - Material, Process and Devices**. InTech.
- Sony, P., Puschnig, P., Nabok, D., and Ambrosch-Draxl, C. (2007). Importance of Van Der Waals Interaction for Organic Molecule-Metal Junctions: Adsorption of Thiophene on Cu(110) as a Prototype. **Physical Review Letters** 99.
- Spataru, C. D., Ismail-Beigi, S., Benedict, L. X., and Louie, S. G. (2004). Excitonic effects and optical spectra of single-walled carbon nanotubes. **Physical Review Letters** 92: 077402.
- Tafreshi, S. S., Roldan, A., and de Leeuw, N. H. (2014). Density Functional Theory Study of the Adsorption of Hydrazine on the Perfect and Defective Copper (100), (110), and (111) Surfaces. **The Journal of Physical Chemistry C** 118: 26103.
- Tang, W., Sanville, E., and Henkelman, G. (2009). A grid-based Bader analysis algorithm without lattice bias. **Journal of Physics: Condensed Matter** 21: 084204.
- Tomohiro, Y., Shigeru, K., and Yutaka, O. (2014). Effect of ambient air on n-type carbon nanotube thin-film transistors chemically doped with poly(ethylene imine). **Japanese Journal of Applied Physics** 53: 05FD01.
- Unalan, H. E., Hiralal, P., Kuo, D., Parekh, B., Amaratunga, G., and Chhowalla, M. (2008). Flexible organic photovoltaics from zinc oxide nanowires grown on transparent and conducting single walled carbon nanotube thin films. **Journal of Materials Chemistry** 18: 5909.

- Wang, P.-C., Liao, Y.-C., Liu, L.-H., Lai, Y.-L., Lin, Y.-C., Su, C.-Y., and Hsu, Y.-J. (2013) Probing the transient fate of C-N bonding in hydrazine-treated carbon nanotubes by synchrotron photoelectron spectroscopy. Vol. 8811, pp. 88110J.
- Weisman, R. B., and Bachilo, S. M. (2003). Dependence of Optical Transition Energies on Structure for Single-Walled Carbon Nanotubes in Aqueous Suspension: An Empirical Kataura Plot. **Nano letters** 3: 1235.
- Williams, Q. L., Liu, X., Walters, W., Zhou, J.-G., Edwards, T. Y., Smith, F. L., Williams, G. E., and Mosley, B. L. (2007). Boron-doped carbon nanotube coating for transparent, conducting, flexible photonic devices. **Applied Physics Letters** 91.
- Wu, Z., Chen, Z., Du, X., Logan, J. M., Sippel, J., Nikolou, M., Kamaras, K., Reynolds, J. R., Tanner, D. B., Hebard, A. F., and Rinzler, A. G. (2004). Transparent, conductive carbon nanotube films. **Science** 305: 1273.
- Xia, F., Farmer, D. B., Lin, Y. M., and Avouris, P. (2010). Graphene field-effect transistors with high on/off current ratio and large transport band gap at room temperature. **Nano letters** 10: 715.
- Xu, X., and Goddard, W. A. (2004). Bonding Properties of the Water Dimer: A Comparative Study of Density Functional Theories. **The Journal of Physical Chemistry A** 108: 2305.
- Yu, M., Tian, W. Q., Jayanthi, C. S., and Wu, S. Y. (2011). The effect of humidity on the adsorption of the hydrazine on single-wall carbon nanotubes: First-principles electronic structure calculations. **Chemical Physics Letters** 518: 93.

- Zhang, D., Ryu, K., Liu, X., Polikarpov, E., Ly, J., Tompson, M. E., and Zhou, C. (2006). Transparent, Conductive, and Flexible Carbon Nanotube Films and Their Application in Organic Light-Emitting Diodes. **Nano letters** 6: 1880.
- Zhang, X.-F., and Shao, X. (2014). π - π binding ability of different carbon nano-materials with aromatic phthalocyanine molecules: Comparison between graphene, graphene oxide and carbon nanotubes. **Journal of Photochemistry and Photobiology A: Chemistry** 278: 69.
- Zhou, Q.-X., Wang, C.-Y., Fu, Z.-B., Tang, Y.-J., and Zhang, H. (2014). Effects of various defects on the electronic properties of single-walled carbon nanotubes: A first principle study. **Frontiers of Physics** 9: 200.
- Zurek, E., Pickard, C. J., and Autschbach, J. (2007). A Density Functional Study of the ^{13}C NMR Chemical Shifts in Functionalized Single-Walled Carbon Nanotubes. **Journal of the American Chemical Society** 129: 4430.

CURRICULUM VITAE

Name: Mr. Wutthisak Prachamon

Date of Birth: 22nd November 1975

Place of Birth: Phukhieo, Chaiyaphum, Thailand.

Education:

2011–2017

Ph.D. candidate in Physics

School of Physics, Institute of Science, Suranaree University of Technology, Nakhon Ratchasima, Thailand.

2006-2009

M.Sc. (Physics)

Department of Physics, Faculty of Science, Ubon Ratchathani University, Ubon Ratchathani, Thailand.

1994-1998

B.Sc. (Physics)

Department of Physics, Faculty of Science, Khon Kaen University, Khon Kaen, Thailand.

Position and Place of Work:

Scientist, Ubon Ratchathani University, Thailand.